Fiber Optic Sensors for the Detection of Water Contaminants

José Miguel da Silva Amaral Pereira
Mestrado em Engenharia Física
Departamento de Física e Astronomia
2023

Supervisor
José Manuel Marques Martins de Almeida, Associate Professor,
University of Trás-os-Montes e Alto Douro

Co-supervisor
Luís Carlos Costa Coelho, Assistant Researcher, INESC TEC

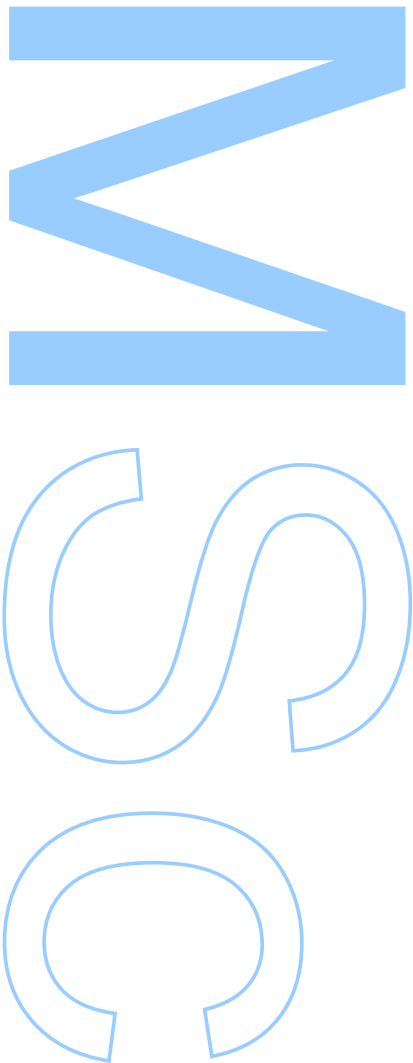


U.PORTO
FEUP FACULDADE DE ENGENHARIA
UNIVERSIDADE DO PORTO


U.PORTO
FACULDADE DE CIÊNCIAS
UNIVERSIDADE DO PORTO

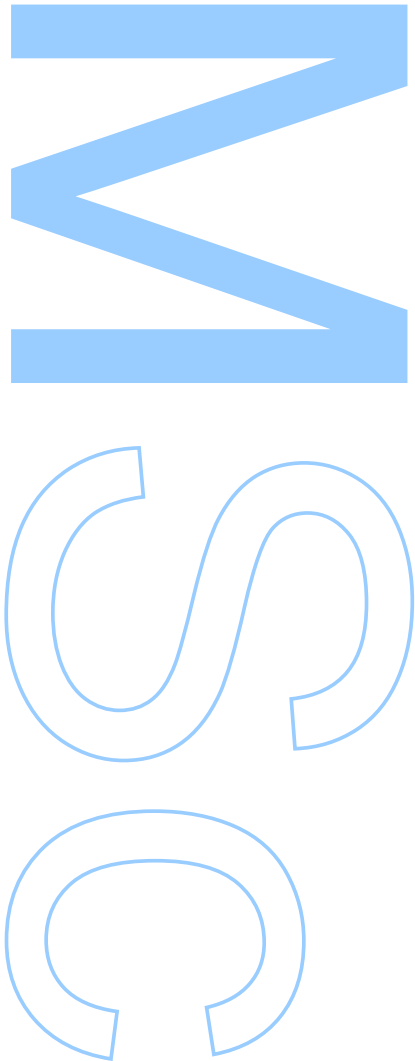

Acknowledgements

As most academic achievements, this dissertation is the result not just from my individual effort, but also from the contribution of multiple people whom I wish to acknowledge.

Firstly, I would like to express my gratitude to my supervisors, Professor José Manuel Marques Martins de Almeida and Dr. Luís Carlos Costa Coelho, for providing this opportunity and for their invaluable contribution in guiding this work. Without their advice and criticism this work would not exist.

I would also like to thank all my colleagues at INESC TEC for their contributions in the development and discussion of this work. Namely, Bernardo Dias for introducing me to the laboratory, João Carvalho for all the help with the sputtering system, Paulo Santos for the support and inspiration and João Mendes for the amount of hours he had to use helping and guiding me while I was lost in the laboratory.

A special thanks to my entire family. I am forever grateful to my parents, Emília and José Carlos, for the constant support, and to my brother Nicolau, for all the hours he spent hearing my ramblings.

UNIVERSIDADE DO PORTO

Abstract

Faculdade de Ciências

Departamento de Física e Astronomia

Master of Science

Fiber Optic Sensors for the Detection of Water Contaminants

by José PEREIRA

In this work, long-period fiber gratings (LPFG) and thin films that support surface plasmon polaritons (SPP) were studied as sensing platforms. A numerical implementation of the transfer matrix method and coupled-mode theory was done, to simulate the LPFG response and support the experimental results. The transfer matrix formalism was also extended to simulate the optical response of a stack of metals and dielectric, to include surface plasmon resonance support. A graphical user interface (GUI) of the latter was developed, to aid the optimization of SPR based sensing structures.

An optical fiber pH sensor based on a LPFG was developed. Two oppositely charged polymers, polyethylenimine (PEI) and polyacrylic acid (PAA), were alternately deposited on the sensing structure through a layer-by-layer (LbL) electrostatic self-assembly technique. Since the polymers are pH sensitive, their refractive index (RI) varies when the pH of the solution changes, due to swelling/deswelling phenomena. The fabricated coating retained a similar property, enabling sensing applications. A two bilayers overlay was deposited on a LPFG, achieving a high sensitivity of (6.3 $\pm$ 0.2)nm/pH in the 5.92-9.23 pH range, with a 20% hysteresis. The sensor reversibility and repeatability were also demonstrated by tracking its response throughout multiple cycles between different pH solutions. With simulation work and results of a low-finesse Fabry-Perot (FP) cavity on a fiber tip, it was estimated that the coating has a thickness of 200nm and 1.53 $\pm$ 0.01 RI when saturated at low pH, expanding up to 310nm with a 1.35 $\pm$ 0.01 RI at higher values, mostly due to the structural changes of PAA. The same coating was also deposited on a LPFG previously coated with 40nm of TiO_2, which had a higher sensitivity to the external RI. The superior

outcome was attained within a narrower pH range, ranging from 6.78 to 8.09, exhibiting a sensitivity of (16.0 $\pm$ 0.2) nm/pH.

By increasing the pH of the PAA dipping solution used in the LbL deposition, a thinner coating can be fabricated. This property was exploited to develop a pH sensor using a surface plasmon resonance (SPR) structure based on a thin gold film on a planar substrate. With 2 bilayers as an overlay, a linear relation between the reflected power and the solution pH was observed in the 5.65-7.52 pH range.

A SPR sensor for the detection of glyphosate, using an aptamer-based sensing probe deposited onto a planar substrate with a gold film, was fabricated and tested. Sensitivity to this contaminant was verified, and a limit of detection of (1.13 $\pm$ 0.03)$\times 10^{-3}$µg/L was obtained, which is lower than the safety limit, making this technology promising for glyphosate sensing.

Keywords: optical sensors, fiber optic sensors, long-period fiber gratings, pH sensor, polymeric nanocoating, plasmonics, surface plasmon resonance, biosensor, glyphosate.

UNIVERSIDADE DO PORTO

Resumo

Faculdade de Ciências
Departamento de Física e Astronomia

Mestrado em Engenharia Física

Sensores em Fibra Ótica para a Deteção de Contaminantes na Água

por José Pereira

Neste trabalho foram estudados como sensores redes de período longo e filmes finos que suportam polaritões plasmónicos de superfície. Foi feita uma implementação numérica do método da matriz de transferência e da teoria dos modos acoplados para simular a resposta de redes de período longo, suportando resultados experimentais. O formalismo das matrizes de transferência foi prolongado para simular a resposta ótica de filmes finos de metais e dielétricos, o que inclui suporte para plasmões de superfície. Uma interface gráfica desta implementação foi desenvolvida, para facilitar a otimização de sensores plasmónicos.

Foi desenvolvido e estudado um sensor em fibra ótica para medição de pH baseado em redes de período longo. Dois polímeros com cargas opostas, polietilenimina e ácido poli-acrílico, foram depositados alternadamente na estrutura através da técnica de deposição camada por camada. Como os polímeros são sensíveis ao pH, o seu índice de refração é alterado quando há variações do pH de uma solução, devido a fenómenos de compressão/expansão. O revestimento fabricado retém a sensibilidade ao pH, podendo ser implementado em sensorização. Para um revestimento da rede de período longo com duas bicamadas, foi obtida uma sensibilidade de (6.3 ± 0.2)nm/pH na gama de pH 5.92-9.23 com 20% de histerese. A reversibilidade e repetibilidade do sensor foram também estudadas através da monitorização da resposta durante múltiplos ciclos entre soluções com diferente pH. Utilizando resultados experimentais de uma cavidade Fabry-Perot na ponta de uma fibra e de simulações, foi estimada uma espessura de 200nm com um índice de refração 1.53 ± 0.01 quando saturada a baixo pH, que expande até 310nm e

um índice de refração de 1.35 $\pm$ 0.01, para os filmes produzidos nas redes de período longo e que variam devido principalmente a mudanças na estrutura do ácido poliacrílico. O mesmo revestimento foi depositado numa rede de período longo recoberta previamente com 40nm de dióxido de titânio, aumentando a sua sensibilidade ao índice de refração do meio externo. O resultado foi uma maior sensibilidade de (16.0 $\pm$ 0.2)nm/pH numa gama de pH menor, 6.78-8.09.

Aumentando o pH da solução de imersão do ácido poliacrílico usada na deposição camada por camada, foi fabricado um revestimento com menor espessura. Esta propriedade foi utilizada para desenvolver um sensor baseado na ressonância de plasmões de superfície obtida através de um filme de ouro depositado num substrato planar. Com um revestimento de duas camadas, observou-se uma relação linear entre a potência refletida e o pH das soluções na região de pH 5.65-7.52.

Um sensor plasmónico para a deteção de glifosato baseado numa estrutura com aptâmeros depositada num substrato planar com um filme de ouro foi fabricado e testado. A sensibilidade a este contaminante foi comprovada, obtendo-se um limite de deteção de (1.13 $\pm$ 0.03)$\times 10^{-3}$µg/L, inferior ao limite de segurança, o que torna esta tecnologia promissora para a deteção de glifosato.

Palavras-chave: sensores óticos, sensores de fibra ótica, redes de período longo, sensor de pH, revestimento polimérico, plasmónica, ressonância de plasmões de superfície, biossensor, glifosato.

Contents

List of Figures

List of Tables

List of Abbreviations

CMT	**C**oupled-**M**ode **T**heory
DI	**D**e**i**onized
EM	**E**lectro**m**agnetic
ESA	**E**lectrostatic **S**elf-**A**ssembly
FBG	**F**iber **B**ragg **G**rating
FDTD	**F**inite-**D**ifference **T**ime-**D**omain
FOM	**F**igure **o**f **M**erit
FP	**F**abry-**P**erot
FWHM	**F**ull **W**idth at **H**alf **M**aximum
GBA	**G**lyphosate **B**inding **A**ptamer
GUI	**G**raphical **U**ser **I**nterface
LbL	**L**ayer-**b**y-**L**ayer
LOD	**L**imit **o**f **D**etection
LPFG	**L**ong-**P**eriod **F**iber **G**rating
LSPR	**L**ocalized **S**urface **P**lasmon **R**esonance
MMF	**M**ulti**m**ode **F**iber
NIR	**N**ear **I**nfra**r**ed
OSA	**O**ptical **S**pectrum **A**nalyzer
PAA	**P**oly**a**crylic **A**cid
PEI	**P**oly**e**thylen**i**mine
PLL	**P**oly-**L**-**l**ysine
RI	**R**efractive **I**ndex
RF	**R**adio **F**requency
SEM	**S**canning **E**lectron **M**icroscope
SMF	**S**ingle-**M**ode Optical **F**iber
SPF	**S**ide-**P**olished **F**iber
SPP	**S**urface **P**lasmon **P**olariton
SPR	**S**urface **P**lasmon **R**esonance
TMM	**T**ransfer-**M**atrix **M**ethod
UV	**U**ltra**v**iolet

Chapter 1

Introduction

1.1 Motivation

Good water quality is essential in drinking water to prevent the start and evolution of contagious diseases, but also for food production, nutrient cycling, habitat provision, flood regulation, and soil formation [1]. Despite having this knowledge, waste production from agriculture, industrial sewage, animal and human activities are still contaminating fresh water supplies, reducing their availability. For this reason, fast and sensitive detection techniques are crucial to ensure a safe and clean water supply. Moreover, industries such as the aquaculture rely on water sensing technology and currently require a development of this technology to keep up with the increasing demand of aquatic products [2].

There are four major water quality parameters that must be controlled, physical parameters, such as pH, temperature, dissolved oxygen, and salinity, organic chemical contaminants, biochemical hazards, cyanotoxins, and biological contaminants. Recently, better sensing structures for in-situ measurements and multiple detection analyses have been introduced in the market, but not with enough resolution to detect biological and chemical contaminants. For this, methods such as spectrophotometry and electrochemical detection, that require water extraction and can take up to few days to obtain the results, are still needed [3].

Optical fiber sensors and plasmonics are two emerging areas that can be used to fabricate sensors capable of fast detection of water contaminants, as they result in small sized structures with high sensitivity to the external environment. Highly specific molecules such

as aptamers, antibodies and some proteins can be introduced to those structures to detect a certain contaminant. Optical fibers can also be implemented in complex multiplexing systems, ideal for monitoring multiple parameters simultaneously.

1.2 Fiber Optic Sensors

Optical fibers have multiple desirable features as a sensing platform, they are flexible, durable, and small, while simultaneously being immune to electromagnetic (EM) and radio frequency (RF) interference, an essential feature for sensors in industrial and environmental scenarios, especially in harsh conditions where monitoring can be critical [4].

Optical fiber gratings are a type of diffraction structure that can be used to enable sensing applications on single-mode optical fibers (SMF). They correspond to a periodic modulation of the refractive index (RI) in the fiber core that satisfies a phase matching condition between the fundamental guided mode and the remaining fiber modes, which can be the counter-propagating core mode, cladding modes, or radiation (or leaky) modes [5]. This allows a controlled power transfer in between them, a phenomenon which depends not only on the grating fabrication parameters but also the environment where it is placed, making them sensitive to strain, temperature, and refractive index.

Gratings in an optical fiber are usually classified into two types, Fiber Bragg Gratings (FBG) (also known as Reflection or Short-Period Fiber Gratings) and Long-Period Fiber Gratings (LPFG) (also called Transmission Gratings) [6]. The FBG was first demonstrated by Hill et al. in 1978 [7], fabricated at the Canadian Communications Research Center using an argon laser. In this structure, coupling occurs between the forward propagating core mode and the backwards propagating modes, whereas an LPFG couples light between modes traveling in the same direction [8]. The former has a sub-micron grating period, while the latter has a period in the range from 100µm to 1mm along a few centimeters of fiber [5]. The higher period allows for an easier and cheaper fabrication using a broader range of techniques.

The first LPFG was successfully obtained through ultraviolet (UV) irradiation in 1996 by Vengsarkar et al. [9] and was used as a sensor in the same year by Bhatia et al. [10]. Later in the year, Bhatia also presented the first theoretical model to calculate the fiber cladding modes [11], a simple approximation that neglected the fiber core and other effects. In 1997, Erdogan developed the theory behind the three-layer model [12], which used the

Transfer-Matrix Method (TMM) and coupled-mode theory (CMT) to estimate the response of an LPFG on a fiber of arbitrary RI. These theories assumed the structure was fabricated using UV laser radiation, therefore only changing the RI of the core and resulting in a coupling to the symmetric cladding modes, but some manufacturing techniques can also modify the cladding RI and/or originate non-uniform longitudinal and radial profiles, leading to a coupling to asymmetric cladding modes. A theoretical and numerical model that can simulate an LPFG with arbitrary azimuthal/radial refractive index variations, solving the problem of the previous models, was presented in 2003 by Anemogiannis et al. [13]. This theory was also used to simulate the LPFG response when an overlay of higher refractive index than the cladding was deposited in an LPFG [14].

Over the years, various applications of LPFGs have been demonstrated, predominantly for its use in optical communications and in sensor systems. They have been implemented in optical communication systems as wavelength selective elements, namely a band-rejection filter [9], a band-pass filter [15] and a gain-flattening filter [16], as well as a wavelength-selective coupler and add-drop multiplexer [17]. As a sensor, its capability to measure temperature [18–20], axial strain [18], curvature [21], and refractive index [22–24] with high resolution has been demonstrated. Since it is sensible to RI variations, with a specific overlay it can also be implemented biological and chemical sensors, and was used to detect biological molecules [25–27], microorganisms [28, 29], pH [30], corrosion [31] and gases [32–34].

The development of a diverse portfolio of techniques for the LPFG fabrication, allows the inscription of these gratings in a huge variety of fibers, and not only the standard single-mode fiber used in telecommunications. Mode coupling was achieved in two-mode fibers [35], multimode fibers [36], dual-core fibers [37], three-layered fibers [38], polarization maintaining fibers [39], pure-silica-core fiber [22], dispersion compensating fiber [40], depressed cladding fibers [41], photonic crystal fibers [42], plastic fibers [43], microstructured fibers [44], and others. Recently, the sensitivity optimization revolved around adding overlays to the sensing region, from high RI materials, such as titanium dioxide [23] and carbon-nanotubes [45], to plasmonic materials [46, 47].

1.3 Surface Plasmon Resonance

When light is coupled at a metal interface, the coherent interaction of photons and conduction band electrons can result in a hybrid structure called plasmon. It is a collective oscillation of the free-electron plasma, which produces travelling EM waves called plasmon polaritons, which when excited in metals are also expressed as charge density waves at their surface and are then considered a surface plasmon polariton (SPP) [48].

The primary focus within the field of plasmonics often centers not on the plasmons themselves, but rather on the SPPs. Their creation is the result of energy transfer from the incident light to the metal, therefore when the standing waves in the plasmonic material combine constructively, a strong optical response such as peaks in absorption or dips in reflectivity can be observed. Since this surface plasmon resonance (SPR) happens at a boundary, its resonance conditions are highly sensitive to the surrounding medium, enabling multiple applications.

The first experimental observation of SPPs was presented by Wood in 1902 [49], who noticed dark stripes in the spectrum of the diffracted light when a metallic diffraction grating was illuminated by a polychromatic light. This phenomenon is known as Wood-Raleigh anomaly as Lord Rayleigh published the first theoretical explanation for this phenomenon in 1907 [50], which was only based on the expansion of the scattered electromagnetic field using waves. Despite multiple developments in the study of these anomalies [51, 52], it was not until 1957, a few years after Pines and Bohm proposed the existence of plasmons [53], that Ritchie predicted that the previously observed energy losses could be described through the collective oscillation of electrons on metallic thin films [54]. In 1959, Powel and Swan confirmed this concept experimentally [55] and in the late 1960's the excitation of surface plasmons using evanescent waves generated from total attenuated reflection was demonstrated by Kretschmann and Raether [56], and Otto [57], using two different configurations. These works were the foundation for the significant development that occurred in the following decades, which ultimately resulted in the commercialization of SPP based optical sensors by several companies.

After the use of SPR for gas detection and biosensing was demonstrated by Nylander and Liedberg in 1982 [58], this technology was exploited in a variety of sensing applications, and due to its high sensitivity and platform flexibility it became a standard for the detection of biomolecular interactions [59] and was implemented in medical and environmental applications such as food quality and the detection of diseases, most notably

cancer. Furthermore, it was used to detect gases, carbon monoxide [60], ammonia [61], hydrogen [62], as well as aqueous pollutants, pesticides [63], methane [64], heavy metals [65], bacteria and toxins [66], and many more substances.

Plasmonic sensors keep getting more attention from the scientific community, as most aspects of this technology are still being researched and improved to meet the current needs of biotechnology. Many options are being explored in order to decrease the band width and increase the sensitivity for a better resolution [67], such as the improvement of the experimental setups and materials and the development of new plasmonic materials, alloys [68], oxides [69], metamaterials [70], and rare-earth metals [71], which is particularly relevant to reduce the sensor's cost, since gold is currently the most reliable option. Other phenomena are also being introduced or combined in the sensing structures, such as localized surface plasmon resonance (LSPR) from using conductive nanoparticles [72], EM field enhancement using other nanomaterials like graphene and graphene oxide [73] and the introduction of interferometry and cavities [74].

1.4 Optical pH Sensors

A logarithmic scale used to indicate acidity or basicity of an aqueous solution is pH. Acidic solutions, with higher concentrations of hydrogen ions, have lower pH values than basic or alkaline solutions, and if $[H^+]$ is the equilibrium molar concentration of the hydrogen ions in a solution, its pH is given by [75]:

$$\text{pH} = -\log([H^+]) \tag{1.1}$$

This parameter is crucial in most chemical reactions, so its control is of high importance to multiple applications such as industrial, biomedical, and environmental [76]. The glass pH electrode is the most conventional instrument to do so as it covers a broad range of pH with high precision and a fast response time [75]. Nevertheless, there remains a demand for alternative sensing structures not only to improve the measurement accuracy but also for measurements in specific scenarios where the electrode cannot be used. For example, in batteries, electrical currents flow through the fluids altering the electrode measurements and in biological cells, nanoscale sensitive structures are needed to monitor the pH.

Optical pH sensing offers a viable alternative to the glass electrodes, which is already popular due to pH indicator strip tests. These optical sensors utilize dyes whose

absorbance in the visible spectrum changes as a response to certain pH levels. This approach allows for a fast assessment of pH without the requirement of any devices or complex setups.

Recently, following the trend in sensing technology, there has been a growing interest in optical fiber-based pH sensors, driven by the demand for compact sensors capable of real-time local and in vivo pH measurements for long periods of time. The first fiber optic pH probe was reported in 1980 [77], and since then various coatings and sensing structures have been proposed and implemented experimentally [75]. Some of these sensors rely on the absorbance or luminescence properties of pH indicators [77], which are affected by alterations in intensity of the incident light and are extremely limited by the dye durability, but the most interesting approaches rely on coatings fabricated with pH-sensitive films [78], which modify their refractive index (RI) in response to pH changes, often as a result of associated swelling and deswelling phenomena.

Most fiber-optic sensing structures have been explored for pH sensing, including LPFGs [79], FBGs [80], fiber SPR [78], and fiber interferometers [81]. The majority of the structures are based on pH sensitive polymers, such as polyacrylamide (PAAm) [78], polyaniline [82], poly(methacrylic acid) (PMA) [83], and polyacrylic acid (PAA) [79]. These polymers can be coated on the fiber through dip coating, but since some of them are polyelectrolytes, the layer-by-layer (LbL) technique can also be used.

1.5 Optical Sensors for Glyphosate Detection

Glyphosate is a widely used herbicide worldwide since the introduction of genetically modified glyphosate-resistance crops. It is considered toxicologically harmful, as it can be associated to human cancers and other chronic diseases, including mental and reproductive behaviors, as well as other animal diseases, due to its ability to form a metal complex [84]. For this reason, it is important to monitor the concentration of glyphosate in real time.

Current detection methods of glyphosate are expensive and slow, so despite most governmental environmental control agencies defining a maximum residue limit for this contaminant, this restriction is ineffective without the development of better sensing structures, with enough resolution to detect that concentration. For the European Union, a limit of 0.1µg/mL was introduced, a lower value than the limit of detection of most sensing methods [85].

Multiple optical sensing techniques have been employed for the detection of glyphosate [85]. SPR based sensors for glyphosate are currently a popular option for biosensors due to its ability to detect biological analytes in a label-free and real-time operation [86], making use of biomolecular interactions at the structure surface. As such, this technology has been successfully used for glyphosate detection [87–89].

1.6 Associated Research Outputs

Part of the work developed in this thesis was submitted and presented at the 28th International Conference on Optical Fiber Sensors, and a poster was also presented at Encontro de Investigação Jovem da Universidade do Porto (IJUP) 2023.

A scientific paper based on the research developed in this thesis, ”Optical pH sensor based on a Long-Period Fiber Grating coated with a Polymeric Layer-by-Layer Electrostatic Self-Assembled Nanofilm”, is currently under review for publication in an international journal.

Chapter 2

Theoretical Background

This chapter presents the physical concepts that define the sensing structures exploited in this work. In section 2.1 the theoretical principle behind long-period fiber gratings is described, and in section 2.2 the theory that defines the surface plasmon polaritons phenomenon as well as the conditions for their existence and excitation on a metal-dielectric interface are presented.

2.1 Long-Period Fiber Gratings

A simple description of LPFGs can be made by considering the three-layer model represented in figure 2.1 [90]. While it is not the correct approach for structures other than a standard SMF with a symmetrical and uniform RI variations, it is a good approximation that allows an understanding of the mode coupling conditions.

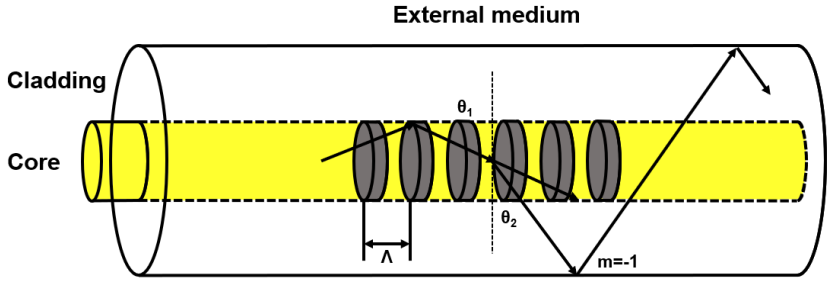

FIGURE 2.1: Ray-optics illustration of cladding-mode coupling by a long-period grating. Adapted from [90].

An LPFG can be simplified to an optical fiber grating imprinted in a fiber core, so its effect on a light wave can be expressed through the diffraction grating equation:

$$n_1 \sin\theta_2 = n_1 \sin\theta_1 + m\frac{\lambda}{\Lambda} \tag{2.1}$$

where n_1 is the RI of the fiber core, θ_1 is the angle of the incident plane wave, θ_2 the angle of the diffracted wave, λ the light wavelength, Λ the spatial period of the modulation and m the diffraction order.

An LPFG couples light to forward-propagating cladding modes, so the transmitted wave has propagation constant $\beta_2 > 0$, and since $\beta = (2\pi/\lambda)n_{eff}$ and $n_{eff} = n_1 \sin\theta$, equation 2.1 can be rewritten as:

$$\beta_2 = \beta_1 + m\frac{2\pi}{\Lambda} \tag{2.2}$$

In a fiber grating, first-order diffraction dominates over the remaining, so we can assume $m = -1$, and therefore the LPFG effect can be described by:

$$\beta_1 - \beta_2 = \frac{2\pi}{\Lambda} \tag{2.3}$$

, which predicts the following resonance wavelength:

$$\lambda = (n_{eff,1} - n_{eff,2})\Lambda \tag{2.4}$$

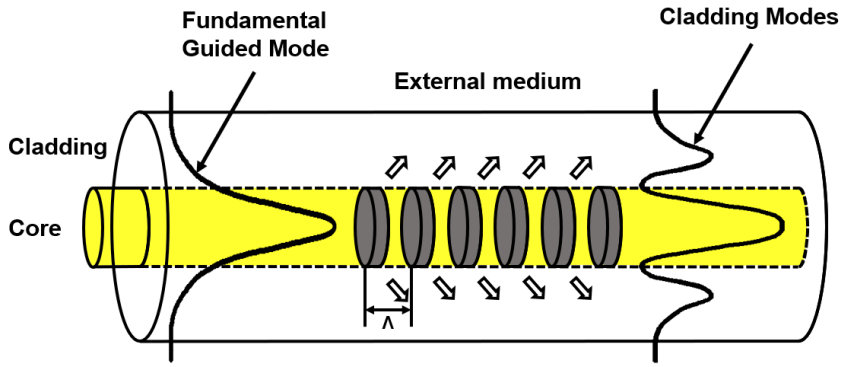

FIGURE 2.2: Coupling of the fundamental guided mode to cladding modes in a long-period grating.

Figure 2.2 represents the principle of operation of an LPFG, light from the fundamental guided mode (or core mode) is perturbed by the RI modulation and coupled to certain cladding modes. From equations 2.3 and 2.4 results that this coupling occurs only at a specific wavelength for a cladding mode of order n, whose propagation constant at that

wavelength satisfies the phase-matching condition. Although this condition is necessary, it is not enough for a significant coupling. An overlap between the modes profile is also necessary for power transfer, and for this reason from the hundreds of cladding modes supported in the considered three-layer cylindrical waveguide, coupling is only observed for a limited number. Consequently, equations 2.3 and 2.4 can be adjusted to:

$$\beta_{co} - \beta_{cl}^{n} = \frac{2\pi}{\Lambda} \tag{2.5}$$

$$\lambda_{res}^{n} = [n_{eff,co}(\lambda) - n_{eff,cl}^{n}(\lambda)]\Lambda \tag{2.6}$$

where β_{co} and $n_{eff,co}(\lambda)$ are the propagation constant and effective refractive index of the core and β_{cl}^{n}, $n_{eff,cl}^{n}(\lambda)$ and λ_{res}^{n} are the propagation constant, effective refractive index and resonance wavelength of the n^{th} cladding mode.

The light coupled to the cladding modes can either be recoupled to the core mode using, for example, another LPFG, or stay in the cladding where it will be lost due to absorption and scattering. These losses originate resonance bands for the different modes, as shown in figure 2.3, so this structure can act as a wavelength selective filter. The difference in the power losses for each mode is associated with cladding modes radial profile, as its overlap with the fundamental guided mode profile and to a lesser extent the remaining cladding modes profiles dictates the power transfer between them.

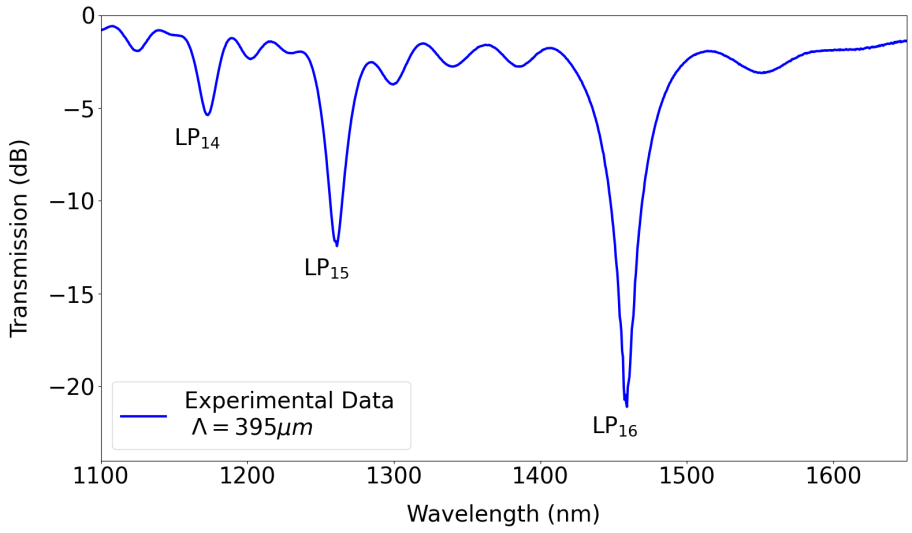

FIGURE 2.3: Transmission spectrum of a typical LPFG (written with the electric arc discharge technique, $\Lambda = 395\mu m$, 40 discharges).

As predicted by equation 2.6, the wavelength position of each LPFG resonance band is affected by the grating period, by applying strain or curvature, and by changing properties of the external medium. The latter allows for sensing applications, being the most relevant property its wavelength dependence on the effective RI which strongly depends on the external refractive index. The fundamental guided mode is constricted to the fiber core and a very small portion of the cladding, so its effective RI only depends on the fiber composition RI, but the higher order cladding modes can interact with the external medium through the electromagnetic evanescent field. Due to this interaction, the cladding modes propagation constant is affected by changes in the RI of the environment the LPFG is placed in, causing a wavelength shift of the loss bands.

2.2 Surface Plasmon Resonance

2.2.1 Surface Plasmon Polaritons on a Metal-Dielectric Interface

An accurate description of SPPs can only be made using quantum mechanics [91], but due to the high carrier density in metals, the Drude classical model can accurately describe the properties of plasma waves in most scenarios, by assuming that the electrons within the last electronic layer are free to propagate in the metal [92].

The EM field generated by light at the metallic interface, as seen in figure 2.4, is characterized by an exponential decay away from the boundary and a propagation along the interface, similarly to an evanescent wave, and can then be written in each material as [92]:

$$E_m(x,z) = E_0 e^{i(-k_{mz}z + k_x x - \omega t)} \tag{2.7}$$

$$E_d(x,z) = E_0 e^{i(k_{dz}z + k_x x - \omega t)} \tag{2.8}$$

where ω is the frequency, E_m and E_d correspond to the field in the metal and dielectric, respectively, k_{mz} and k_{dz} are the components of the wavevectors perpendicular to the interface and k_x is the parallel component.

The out-of-plane momentum $k_z = ik_z''$ is imaginary, since the wave does not propagate in that direction, but the associated charge fluctuations that generate the field occur in that path. These oscillations are within a very small range of one angstrom [94], so surface

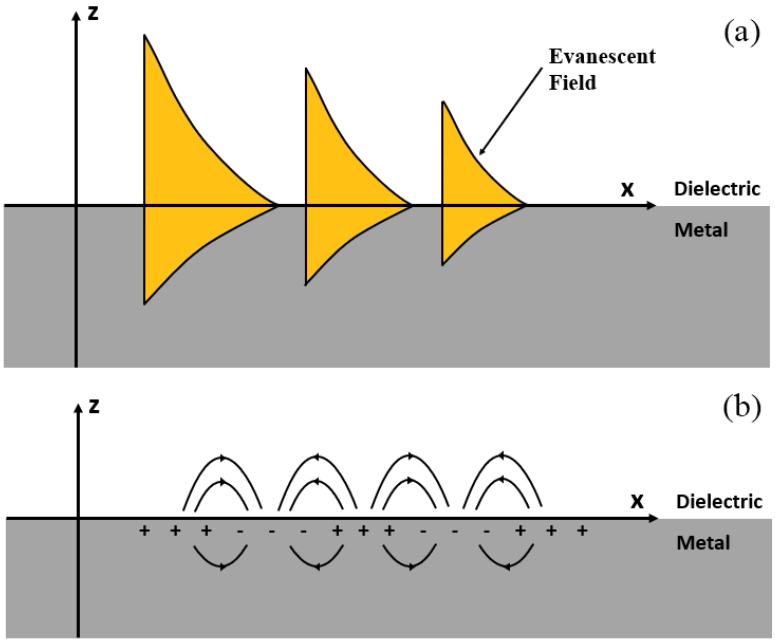

FIGURE 2.4: Schematic representation of the distribution of the electromagnetic field of SPP at a metal-dielectric interface. (a) SPP decay along the interface and time propagation; (b) electric field orientation and interaction with the charges at the metal surface. Adapted from [93].

properties have a high impact in the generated field, which has its advantages and disadvantages as it can allow interesting implementations but implies a careful handling of the structures.

Since the perpendicular component of the wavevector describes the field decay, it also dictates the penetration depth, which is different for each medium. This parameter is of high importance for biosensors, and is defined as [95]:

$$\delta = \frac{1}{2|k_z|} \tag{2.9}$$

which is typically in the order of tens of nanometers into the metal and hundreds of nanometers into the dielectric.

From the Maxwell equations and the boundary conditions for two interfaces, the following dispersion relations for the SPP can be obtained [48]:

$$\frac{k_{zm}''}{\varepsilon_m} = -\frac{k_{zd}''}{\varepsilon_d}, \quad \text{p polarization} \tag{2.10}$$

$$k_{zm}'' = -k_{zd}'', \quad \text{s polarization} \tag{2.11}$$

From these conditions, we conclude that p polarized light can excite the surface waves when the materials have permittivity with opposite signs which, ignoring magnetic properties, is only possible on the interface of a metal with a negative permittivity and a dielectric, whereas the s polarized light dispersion relation has no solution. The condition for the TE polarized modes can be rewritten to obtain the propagation constant of the surface wave [48]:

$$\beta = k_x = \frac{\omega}{c}\sqrt{\frac{\varepsilon_m \varepsilon_d}{\varepsilon_m + \varepsilon_d}} \tag{2.12}$$

where $\varepsilon_m = \varepsilon_m^{'} + i\varepsilon_m^{''}$ and $\varepsilon_d = \varepsilon_d^{'} + i\varepsilon_d^{''}$ are the permittivity of the metal and dielectric. Since k_x needs a real component to result in wave propagation, the interface media need the following properties:

$$\varepsilon_m \varepsilon_d < 0 \quad \text{and} \quad \varepsilon_m + \varepsilon_d < 0 \tag{2.13}$$

While not as relevant as the penetration depth, since k_x is a complex quantity a propagation length of the surface plasmon polariton can also be defined:

$$\delta = \frac{1}{2k_x^{''}} \tag{2.14}$$

If we assume a metal without field attenuation, its dielectric constant can be calculated using the free electron model:

$$\varepsilon_m(\omega) = 1 - \left(\frac{\omega_p}{\omega}\right)^2 \tag{2.15}$$

where ω_p is the plasma frequency as given by the Drude model, the frequency value in which the metal stops being highly reflective and becomes transparent:

$$\omega_p = \sqrt{\frac{Ne^2}{\varepsilon_0 m_e}} \tag{2.16}$$

with N, e and m_e being the density, electric charge and effective mass of the electrons, respectively, and ε_0 the vacuum permittivity. This result can be used to obtain the dispersion curve of a SPP, as represented in figure 2.5.

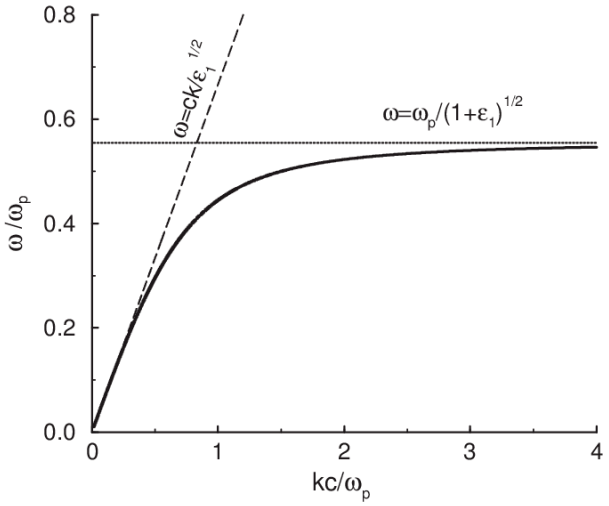

FIGURE 2.5: Dispersion of SPP at a dielectric-metal interface. The dashed line shows the dispersion of light in the dielectric and the dotted line the corresponding surface plasmon frequency [96].

For low ω and k values the SPP branch is light like, due to the proximity to the light line, and the SPP dispersion relation can be approximated to one of the light in a medium of permittivity ε_1:

$$\omega = \frac{ck_x}{\sqrt{\varepsilon_1}} \tag{2.17}$$

The curve has an asymptotic behavior, at high k values a cutoff frequency can be observed, meaning that only light with wavelength above a certain value can excite the surface wave. This value corresponds to a pole of equation 2.12:

$$\omega = \frac{\omega_p}{\sqrt{1+\varepsilon_1}} \tag{2.18}$$

As the dispersion curve of SPPs is always below the light line, this wave cannot be generated through direct excitation since the parallel component of the wavevectors will never be equal. Light coupling techniques are then needed to produce light with the required characteristics.

2.2.2 Excitation of Surface Plasmon Polaritons

Multiple configurations exist for inducing SPPs, with the Kretschmann [56] and Otto [57] configurations, based on the prism coupling technique, still being the primary choices in bulk optics-based SPR. Nonetheless, there are other interesting approaches like the grating coupling configurations [97], including fiber gratings like LPFGs, and the waveguide

coupling configurations [98]. In this work, the excitation of SPPs using the Kretschmann configuration and using a side-polished single-mode optical fiber are considered.

In recent years, significant interest has turned towards incorporating the SPR sensing into optical waveguide structures. This can offer a host of advantageous traits for sensing applications, notably compact dimensions, robustness, the potential for crafting multiple or multichannel sensors on a single unit, and when combined with optical fibers, the capability for remote sensing.

In SPP sensors, the coupling conditions of the plasmonic mode vary with a change of the external RI, so a shift can be detected by an experimental setup. This shift allows four different methods of interrogating plasmonic structures, the spectral, angular, intensity and phase interrogation, which require different setups. Only the spectral interrogation mode was employed in this work, which detects a wavelength shift of the SPP and therefore requires a light source for the intended range and a spectrometer.

The Kretschmann (or Kretschmann-Raether) configuration conjugates the prism coupling technique (PCT) and the attenuated total reflection (ATR) to generate an evanescent wave with a wavevector that matches the values of a SPP dispersion curve. The PCT consists in using an optical prism with a high RI to couple light into a thin film at its base [99], where ATR occurs when light is refracted at an interface between a medium with high RI and another with smaller RI, with an incident angle larger than the critical angle, which will reflect most light but also form the evanescent wave with a frequency region corresponding to the values where the second medium is non-absorbing [100].

As shown in figure 2.6, in this configuration a metallic layer with a thickness of several tens of nanometers is in contact with the prism. The electromagnetic field decays exponentially inside the film and excites the surface plasmon on the interface of the metal and the dielectric. For an easy experimental implementation, the thin metallic film can be deposited on a substrate of a material similar to the prism, and then this structure placed on the prism base using index matching fluid. In this case, the substrate will only act as an extension of the prism, requiring a change of the incident angle according to its thickness.

This configuration remains a highly popular option, despite all the alternatives developed over the years. Implementation of experimental setups for bulk SPR structures is simple, and the devices have great flexibility and high signal-to-noise ratio, allowing high resolution measurements.

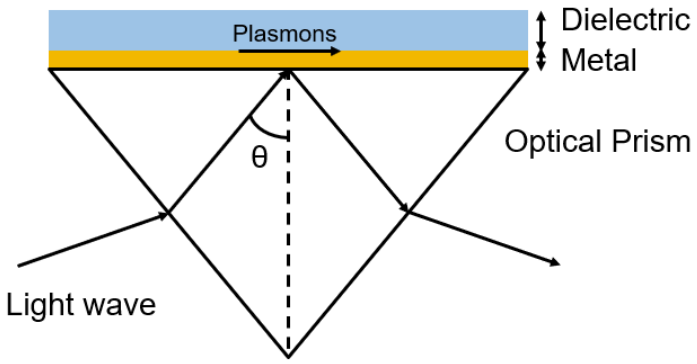

Figure 2.6: Schematic of the Kretschmann configuration for the excitation of plasmon waves.

The same Kretschmann configuration can be implemented in optical fibers. Multimode fibers (MMF) are very common structures for SPR generation in optical fibers, as their rigid structure not only results in robust structures but also enables an easy removal of their coating and cladding, without the need of a specific setup. Their large core even allows for further etching to change the evanescent field properties. The cladding removal allows access to the evanescent field of the multiple modes guided in the core, which similarly to what happens in the prism configurations, has enough power to excite the SPP in the metal-dielectric interface of a thin film deposited on the core. Since in this structure films are deposited in the entire region of the cylindrical waveguide, even with a small sensor size the active surface sensing area is more extensive than the planar configurations, which can be an advantage in biological sensing. Nevertheless, the high numerical aperture of the fiber results in wider bands than those obtained in the planar setup.

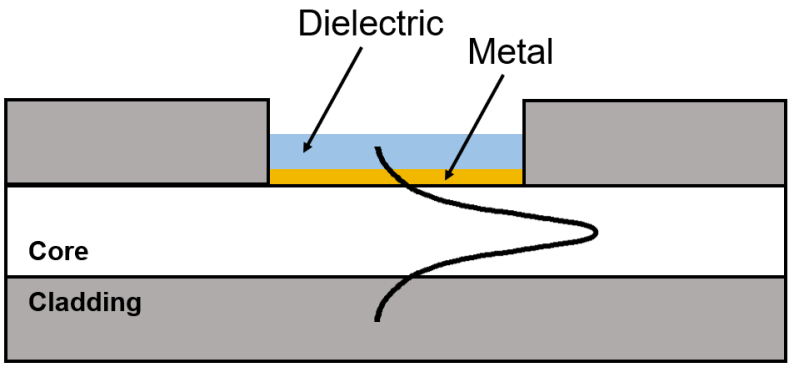

Figure 2.7: Configuration for SPR excitation in a side-polished optical fiber.

A side-polished fiber (SPF) is an alternative structure for SPP excitation in optical fibers. In this case, the cladding is only removed on one side of the fiber, but it still allows access to the evanescent field that typically propagates in the cladding, as seen in figure 2.7. This structure is particularly relevant for single-mode and plastic optical fibers, whose flexibility creates the need for specific fabrication setups to remove their cladding. Nevertheless, a simple and low-cost manufacturing process such as a wheel-type fiber polishing machine with sandpaper can be used [101], and the flat polished surface allows for an easy deposition of uniform metal films through multiple techniques. However, without the cladding, the fiber elasticity and mechanical strength are severely reduced, which might limit the life span of the sensor. Despite the fragility, this configuration remains relevant, especially for single-use implementations and multiplexing on a single fiber.

Chapter 3

Simulation of Sensing Structures

Simulation methodologies used in the design and fabrication of LPFGs and structures that support SPR are presented in this chapter. Section 3.1 describes the use of the transfer matrix method to calculate propagations constants of an optical fiber modes, and the coupled-mode theory to model the effects of the grating. In section 3.2 is the used transfer method formalism and its computation implementation, which can accurately model the optical response of 1D stacks of metals and dielectrics, including SPR.

3.1 Long-Period Fiber Gratings

An implementation of the numerical method presented by Anemogiannis et al. [13] was done using Python, in order to simulate the response of the fabricated LPFGs when an overlay is deposited. This model allows for the simulation of a grating with arbitrary azimuthal/radial refractive index variations, but since the fabrication through electric arc creates a very complex longitudinal and transversal RI profile it wasn't possible to take full advantage of this feature.

For the purpose of this work, the fabricated LPFGs RI index profile was approximated to a sinusoidal modulation of amplitude 3.6×10^{-4} in a sector profile of angles $0° < \phi < 270°$, in both the core and cladding, so similarly to the fabricated structures coupling to the LP_{1j} modes was observed.

The values for a standard SMF were used in the simulations, a core diameter of 8.2µm and cladding diameter of 125µm. The RI values for each wavelength were obtained using the "ofiber" python package.

3.1.1 Calculation of the Propagation Constants of LP Modes in a Multilayer Cylindrical Waveguide

Since it was already proved that the LP modes approximation is adequate for a description of a cylindrical waveguide, under the assumption of weak guidance [102], it was used in combination with the transfer matrix method (TMM) to describe the fields in the fiber. While the RI difference between the cladding and ambient medium is not negligible, specially when a high RI overlay is added to the structure, its effect is minimal for the low order modes that were analyzed.

For an $LP_{\nu j}$ mode of azimuthal number ν and order j within a cylindrical dielectric layer i with radius $r_{i-1} < r < r_i$ and refractive index n_i, they have a transverse electric field component propagating along the z-axis which is given by [13]:

$$\begin{aligned} U_{\nu j,i}(r,\phi,z) &= \exp(-j\beta_{\nu j}z)\Psi_{\nu j,i}(r,\phi) \\ &= \exp(-j\beta_{\nu j}z)\Phi_{\nu}(\phi)R_{\nu j,i}(r) \\ &= \exp(-j\beta_{\nu j}z)\begin{Bmatrix}\cos(\nu\phi)\\ \sin(\nu\phi)\end{Bmatrix} \\ &\times \begin{cases} A_{\nu j,i}J_{\nu}(r\gamma_{\nu j,i}) + B_{\nu j,i}Y_{\nu}(r\gamma_{\nu j,i}), & \text{when } \beta_{\nu j} < k_0 n_i \\ A_{\nu j,i}I_{\nu}(r\gamma_{\nu j,i}) + B_{\nu j,i}K_{\nu}(r\gamma_{\nu j,i}), & \text{when } \beta_{\nu j} > k_0 n_i \end{cases} \end{aligned} \tag{3.1}$$

where λ is the operating free space wavelength, $k_0 = 2\pi/\lambda$, $\beta_{\nu j}$ is the longitudinal propagation constant of the $LP_{\nu j}$ mode, $\gamma_{\nu j,i} = \sqrt{|k_0^2 n_i^2 - \beta_{\nu j}^2|}$ is the magnitude of the transverse wavenumber, ϕ is the azimuthal angle, and $A_{\nu j,i}$ and $B_{\nu j,i}$ are arbitrary field expansion coefficients determined by the boundary conditions within the cylindrical layer i. $J_{\nu}(r\gamma_{\nu j,i})$ and $Y_{\nu}(r\gamma_{\nu j,i})$ are the ordinary Bessel functions of the first and second kind of order ν, while $I_{\nu}(r\gamma_{\nu j,i})$ and $K_{\nu}(r\gamma_{\nu j,i})$ are the modified Bessel functions of the first and second kind of order ν, with ν being a nonnegative integer number. For $v > 0$ there is a two-folded degeneracy due to the sine and cosine dependence of the fields. Two different LP modes must be considered, $LP_{\nu j}^{S}$ and $LP_{\nu j}^{C}$, with $\sin(\nu\phi)$ and $\cos(\nu\phi)$ azimuthal dependence, respectively. The chosen sector profile with RI variation for $0° < \phi < 270°$ will simplify the analysis.

The radial field in a layer i of a multilayer cylindrical waveguide is then given by:

$$
\begin{aligned}
R_{\nu j,i}(r,\phi,z) &= A_{\nu j,i}C_\nu(r\gamma_{\nu j,i}) + B_{\nu j,i}D_\nu(r\gamma_{\nu j,i}) \\
&= \begin{cases} A_{\nu j,i}J_\nu(r\gamma_{\nu j,i}) + B_{\nu j,i}Y_\nu(r\gamma_{\nu j,i}), & \text{when } \beta_{\nu j} < k_0 n_i \\ A_{\nu j,i}I_\nu(r\gamma_{\nu j,i}) + B_{\nu j,i}K_\nu(r\gamma_{\nu j,i}), & \text{when } \beta_{\nu j} > k_0 n_i \end{cases}
\end{aligned} \tag{3.2}
$$

Since the electric field and its tangential component must be continuous at the interface of two consecutive layers:

$$
\begin{aligned}
& R_{\nu j,i}(r_i) = R_{\nu j,i+1}(r_i) \\
& \Leftrightarrow A_{\nu j,i}\mathbf{C}_\nu(r_i\gamma_{\nu j,i}) + B_{\nu j,i}\mathbf{D}_\nu(r_i\gamma_{\nu j,i}) \\
& = A_{\nu j,i+1}\mathbf{C}_\nu(r_i\gamma_{\nu j,i+1}) + B_{\nu j,i+1}\mathbf{D}_\nu(r_i\gamma_{\nu j,i+1})
\end{aligned} \tag{3.3}
$$

$$
\begin{aligned}
& \frac{dR_{\nu j,i}(r_i)}{dr} = \frac{dR_{\nu j,i+1}(r_i)}{dr} \\
& \Leftrightarrow \gamma_{\nu j,i}\left[A_{\nu j,i}\mathbf{C}'_\nu(r_i\gamma_{\nu j,i}) + B_{\nu j,i}\mathbf{D}'_\nu(r_i\gamma_{\nu j,i})\right] \\
& = \gamma_{\nu j,i+1}\left[A_{\nu j,i+1}\mathbf{C}'_\nu(r_i\gamma_{\nu j,i+1}) + B_{\nu j,i+1}\mathbf{D}'_\nu(r_i\gamma_{\nu j,i+1})\right]
\end{aligned} \tag{3.4}
$$

Solving the system of equations 3.3 and 3.4 for $A_{\nu j,i}$ and $B_{\nu j,i}$, the transfer matrix for a single homogeneous cylindrical layer is obtained:

$$
\begin{pmatrix} A_{\nu j,i} \\ B_{\nu j,i} \end{pmatrix} = \begin{pmatrix} \frac{m_{11}^{i,i+1}(\beta_{\nu j})}{Q_i} & \frac{m_{12}^{i,i+1}(\beta_{\nu j})}{Q_i} \\ \frac{m_{21}^{i,i+1}(\beta_{\nu j})}{Q_i} & \frac{m_{22}^{i,i+1}(\beta_{\nu j})}{Q_i} \end{pmatrix} \begin{pmatrix} A_{\nu j,i+1} \\ B_{\nu j,i+1} \end{pmatrix} = \mathcal{M}_{i,i+1} \begin{pmatrix} A_{\nu j,i+1} \\ B_{\nu j,i+1} \end{pmatrix} \tag{3.5}
$$

where

$$
\begin{aligned}
m_{11}^{i,i+1}(\beta_{\nu j}) &= \gamma_{\nu j,i}\mathbf{D}'_\nu(r_i\gamma_{\nu j,i})\mathbf{C}_\nu(r_i\gamma_{\nu j,i+1}) - \gamma_{\nu j,i+1}\mathbf{D}_\nu(r_i\gamma_{\nu j,i})\mathbf{C}'_\nu(r_i\gamma_{\nu j,i+1}), \\
m_{12}^{i,i+1}(\beta_{\nu j}) &= \gamma_{\nu j,i}\mathbf{D}'_\nu(r_i\gamma_{\nu j,i})\mathbf{D}_\nu(r_i\gamma_{\nu j,i+1}) - \gamma_{\nu j,i+1}\mathbf{D}_\nu(r_i\gamma_{\nu j,i})\mathbf{D}'_\nu(r_i\gamma_{\nu j,i+1}), \\
m_{21}^{i,i+1}(\beta_{\nu j}) &= -\gamma_{\nu j,i}\mathbf{C}'_\nu(r_i\gamma_{\nu j,i})\mathbf{C}_\nu(r_i\gamma_{\nu j,i+1}) + \gamma_{\nu j,i+1}\mathbf{C}_\nu(r_i\gamma_{\nu j,i})\mathbf{C}'_\nu(r_i\gamma_{\nu j,i+1}), \\
m_{22}^{i,i+1}(\beta_{\nu j}) &= -\gamma_{\nu j,i}\mathbf{C}'_\nu(r_i\gamma_{\nu j,i})\mathbf{D}_\nu(r_i\gamma_{\nu j,i+1}) + \gamma_{\nu j,i+1}\mathbf{C}_\nu(r_i\gamma_{\nu j,i})\mathbf{D}'_\nu(r_i\gamma_{\nu j,i+1}), \\
Q_i &= \gamma_{\nu j,i}\left(\mathbf{C}_\nu(r_i\gamma_{\nu j,i})\mathbf{D}'_\nu(r_i\gamma_{\nu j,i}) - \mathbf{C}'_\nu(r_i\gamma_{\nu j,i})\mathbf{D}_\nu(r_i\gamma_{\nu j,i})\right).
\end{aligned} \tag{3.6}
$$

The relation in equation 3.5 can be applied along $N+1$ layers, resulting in a global matrix that relates the field in the fiber core, $i=1$, to the external layer, $i=N+1$:

$$\begin{aligned}\begin{pmatrix} A_{\nu j,1} \\ B_{\nu j,1} \end{pmatrix} &= \mathcal{M}_{1,2}\mathcal{M}_{2,3}...\mathcal{M}_{N,N+1} \begin{pmatrix} A_{\nu j,N+1} \\ B_{\nu j,N+1} \end{pmatrix} \\ &= \begin{pmatrix} m_{11}^{1,N+1}(\beta_{\nu j}) & m_{12}^{1,N+1}(\beta_{\nu j}) \\ m_{21}^{1,N+1}(\beta_{\nu j}) & m_{22}^{1,N+1}(\beta_{\nu j}) \end{pmatrix} \begin{pmatrix} A_{\nu j,N+1} \\ B_{\nu j,N+1} \end{pmatrix}\end{aligned} \tag{3.7}$$

Since the fields in the fiber core and external medium must be finite, $A_{\nu j,N+1} = B_{\nu j,1} = 0$, and from equation 3.7 the following condition is obtained:

$$m_{22}^{1,N+1}(\beta_{\nu j}) = 0 \tag{3.8}$$

The propagation constants of the defined structure can be obtained by finding the roots of a transfer matrix element, which was done using the bisection method. After the calculation, the coefficients $A_{\nu j,i}$ and $B_{\nu j,i}$ can also be obtained using equation 3.7 and by assuming a value for $A_{\nu j,1}$ or $B_{\nu j,N+1}$, which can be arbitrary since it will be normalized before further use. Each LP mode carries power given by equation 3.9, that can be solved for a normalization constant if a constant power for each mode is defined (1W was used in the simulations). Figure 3.1 represents the radial field profiles of the simulated structure, obtained using the described technique.

$$\mathcal{P}_{\nu j} = \frac{\beta_{\nu j}}{2\omega\ \mu_0} \int_0^{2\pi} \Phi_\nu^2(\phi) d\phi \int_0^{\infty} R_{\nu j}^2(r) r dr = \mathcal{P}_0 \tag{3.9}$$

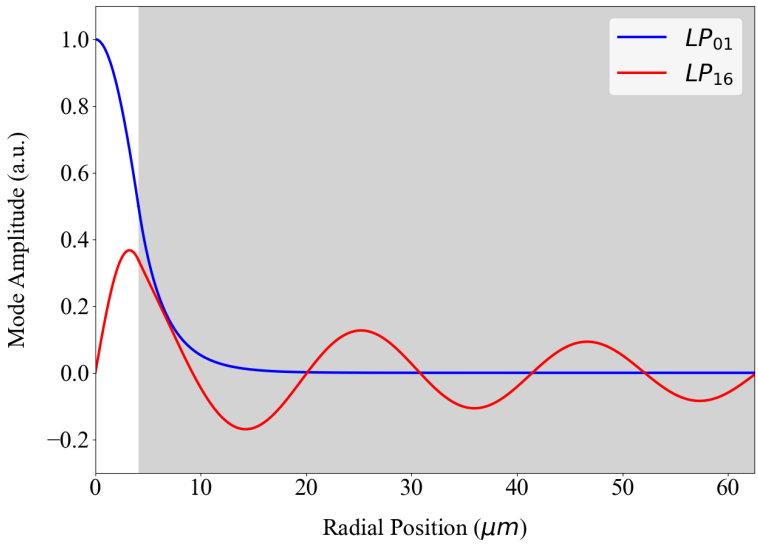

Figure 3.1: Radial functions of the LP_{01} and LP_{16} fiber modes (gray area corresponds to the fiber cladding).

3.1.2 Coupling Coefficients Formulation

Coupled-mode theory defines the interaction between optical modes as being proportional to their coupling coefficient K [12, 13]. For LP mode analysis only the longitudinal coefficient is relevant, and it is expressed in cylindrical coordinates as:

$$K_{\nu j,\mu k} = \frac{\omega}{4\mathcal{P}_0} \times \int_{\phi=0}^{2\pi} \int_{r=0}^{\infty} \Delta\epsilon(r,\phi,z)\Psi_{\nu j}(r,\phi)\Psi_{\mu k}(r,\phi) r dr d\phi \tag{3.10}$$

where $\Psi(r,\phi)$ is the transverse field of an LP mode, previously calculated through the TMM method, and $\Delta\epsilon(r,\phi,z)$ the permittivity variation. Since weak guidance between the core and cladding is assumed,

$$\Delta\epsilon(r,\phi,z) \approx 2\epsilon_0 n_0(r)\Delta n(r,\phi,z) \tag{3.11}$$

where ϵ_0 is the freespace permittivity, $n_0(r)$ is the unperturbed refractive index profile of the structure, and $\Delta n(r,\phi,z)$ is the variation of the refractive index.

The refractive index change in a grating can then be described as:

$$\Delta n(r,\phi,z) = \sigma(z)S(z)P(r,\phi) \tag{3.12}$$

with $\sigma(z)$ being the apodization factor, $P(r,\phi)$ the transverse refractive index perturbation, which has to be defined for every layer i that was perturbed, and $S(z)$ the longitudinal periodic function of period Λ, typically approximated by a Fourier series with two coefficients, $S(z) = s_0 + s_1 cos((2\pi/\Lambda)z)$. Since a sinusoidal modulation was used for this work, $s_0 = s_1 = 1$.

With this approximation, equation 3.10 can be rewritten,

$$\begin{aligned} K_{\nu j,\mu k} &= \sigma(z)\left[s_0 + s_1 cos\left(\left(\frac{2\pi}{\Lambda}\right)z\right)\right]\frac{\omega}{4\mathcal{P}_0} \\ &\times \int_{\phi=0}^{2\pi}\int_{r=0}^{\infty} n_0(r)P(r,\phi)\Psi_{\nu j}(r,\phi)\Psi_{\mu k}(r,\phi) r dr d\phi \quad (6) \\ &= \sigma(z)\left[s_0 + s_1 cos\left(\left(\frac{2\pi}{\Lambda}\right)z\right)\right]\zeta_{\nu j,\mu k} \end{aligned} \tag{3.13}$$

For the simulated structure, which has a sinusoidal RI variation in the core and cladding with the same amplitude p,

$$\zeta_{\nu j,\mu k}^{\{S\}\{S\}} = \frac{\omega\epsilon_0}{2\mathcal{P}_0} p \int_{\phi=\theta_1}^{\theta_2} \begin{Bmatrix} \cos(\nu\phi) \\ \sin(\nu\phi) \end{Bmatrix} \begin{Bmatrix} \cos(\mu\phi) \\ \sin(\mu\phi) \end{Bmatrix} d\phi \times \sum_{i=1}^{2} n_0(r_i) \int_{r=r_{i-1}}^{r_i} R_{\nu j}(r) R_{\mu k}(r) r dr \tag{3.14}$$

The {S} and {C} notation refers to the sine and cosine azimuthal dependence of the field, that as previously mentioned implies that an LP mode with $v > 0$ has to be treated as two independent modes.

3.1.3 Resonance Band Displacement

The modified first-order Brag condition can be used to accurately predict the band position without the computational effort required to simulate a transmission spectrum. It is a simple change of the traditional LPFG equation, that adds the self-coupling coefficients of the core and cladding mode to account for different fiber and RI modulations:

$$(\beta_{01}(\lambda) + s_0\zeta_{01,01}(\lambda)) - \left(\beta_{\nu j}(\lambda) + s_0\zeta_{\nu j,\nu j}^{\{S\}}(\lambda)\right) = \frac{2\pi}{\Lambda} \tag{3.15}$$

Using this relation, a phase-match condition graph, that presents the resonance wavelength of the modes for different gratings periods, can be obtained. For the simulated structure, that couples light to asymmetric first order cladding modes, this graph is presented in figure 3.2. Equation 3.15 can also be used to simulate the LPFG response to a variation of the external refractive index and the introduction of deposited overlays with different thicknesses, as presented in figure 3.3.

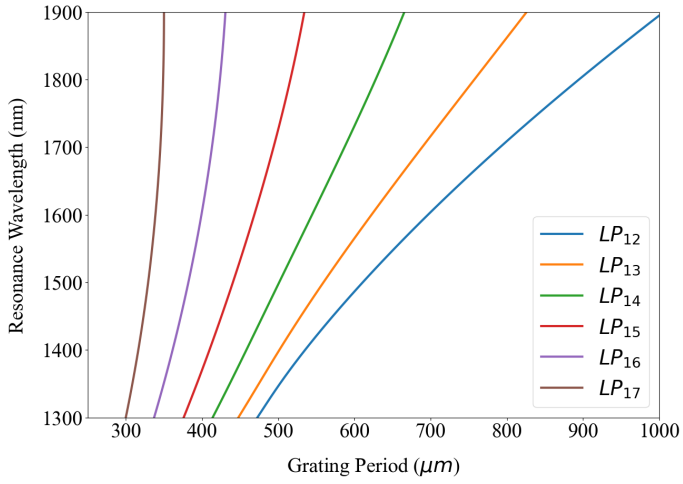

Figure 3.2: Simulated relationship between grating periodicity and wavelength where guided-to-cladding mode coupling takes place (phase-match condition graph).

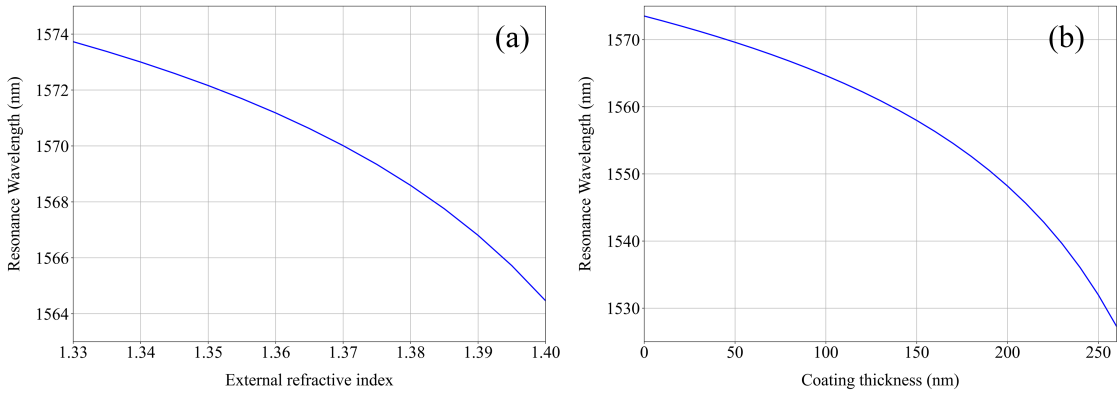

Figure 3.3: Simulated shift of the resonance wavelength of an LP_{16} LPFG mode with a variation of the (a) external refractive index and (b) thickness of a 1.543 RI coating with 1.333 external RI.

3.1.4 Coupled Mode Equations

The general coupled mode equation that describes the mode's evolution in an LPFG through their complex amplitude $\mathbf{A}(z)$ is:

$$\frac{d\mathbf{A}_{\mu k}(z)}{dz} = -j \sum_{\nu j=01}^{M} K_{\nu j,\mu k}\mathbf{A}_{\nu j}(z)\exp(-j(\beta_{\nu j} - \beta_{\mu k})z), \quad \mu k = 01, \dots M \tag{3.16}$$

which can be expressed in a matrix form:

$$\begin{pmatrix} \dot{A}_{01}(z) \\ \dot{A}_{02}(z) \\ \vdots \\ \dot{A}^C_{11}(z) \\ \dot{A}^S_{11}(z) \\ \dot{A}^C_{12}(z) \\ \vdots \end{pmatrix} = \begin{pmatrix} \mathbf{Q}_{01} & \mathbf{V}_{01,02} & \dots & \mathbf{V}^C_{01,11} & \mathbf{V}^S_{01,11} & \mathbf{V}^C_{01,12} & \dots \\ \mathbf{V}_{02,01} & \mathbf{Q}_{02} & \dots & \mathbf{V}^C_{02,11} & \mathbf{V}^S_{02,11} & \mathbf{V}^C_{02,12} & \dots \\ \vdots & \vdots & \vdots & \vdots & \vdots & \vdots & \vdots \\ \mathbf{V}^C_{11,01} & \mathbf{V}^C_{11,02} & \dots & \mathbf{Q}^C_{11} & \mathbf{P}^{CS}_{11} & \mathbf{V}^{CC}_{11,12} & \dots \\ \mathbf{V}^S_{11,01} & \mathbf{V}^S_{11,02} & \dots & \mathbf{P}^{SC}_{11} & \mathbf{Q}^S_{11} & \mathbf{V}^{SC}_{11,12} & \dots \\ \mathbf{V}^C_{12,01} & \mathbf{Q}^C_{12,02} & \dots & \mathbf{V}^{CC}_{12,11} & \mathbf{V}^{CS}_{12,11} & \mathbf{Q}^C_{12} & \dots \\ \vdots & \vdots & \vdots & \vdots & \vdots & \vdots & \vdots \end{pmatrix} \begin{pmatrix} A_{01}(z) \\ A_{02}(z) \\ \vdots \\ A^C_{11}(z) \\ A^S_{11}(z) \\ A^C_{12}(z) \\ \vdots \end{pmatrix} \tag{3.17}$$

where $\mathbf{Q}_{\nu j}$ terms correspond to self-coupling coefficients, $\mathbf{P}_{\nu j}$ to the cross-coupling coefficients between the cosine and sine forms of the same LP mode and $\mathbf{V}_{\nu j,\mu k}$ to the cross-coupling coefficients between different LP modes:

$$
\begin{aligned}
\mathbf{Q}_{\nu j}^{\{_S^C\}} &= -j\sigma(z)s_0\zeta_{\nu j,\nu j}^{\{_S^C\}}, \\
\mathbf{P}_{\nu j}^{\{_S^C\}\{_S^C\}} &= -j\sigma(z)s_0\zeta_{\nu j,\mu k}^{\{_S^C\}\{_S^C\}}, \quad \text{if } \beta_{\nu j} = \beta_{\mu k}, \\
\mathbf{V}_{\nu j,\mu k}^{\{_S^C\}\{_S^C\}} &= -j\sigma(z)\frac{s_1}{2}\zeta_{\nu j,\mu k}^{\{_S^C\}\{_S^C\}} \exp\left[-j\left(\beta_{\nu j} - \beta_{\mu k} \pm \frac{2\pi}{\Lambda}\right)z\right], \quad \text{if} \beta_{\nu j} \neq \beta_{\mu k}.
\end{aligned}
\tag{3.18}
$$

This system of differential equations can be solved numerically using the backward differentiation formula by assuming that only one mode is incident in the LPFG, $A_{01}(0) = 1$ and the remaining amplitudes are null. The transmission through an LPFG of length L is then obtained,

$$
Transmission = \frac{|A_{01}(L)|^2}{|A_{01}(0)|^2} \tag{3.19}
$$

The matrix formulation is complex, and its solution takes a long time to compute especially when using an interpreted language such as Python. The number of modes included in the simulation was then limited to the LP_{0j} LP_{1j} modes up to order 7, which was proven enough to simulate a grating response similar to the fabricated one, as seen by the results in figures 3.4 and 3.5. Interaction with higher order layers can be added, but since it wasn't possible to obtain the RI profile of the induced electric-arc LPFG, the interest of the results is always qualitative and there is no need to increase the computational effort only for a slightly more accurate simulated spectrum.

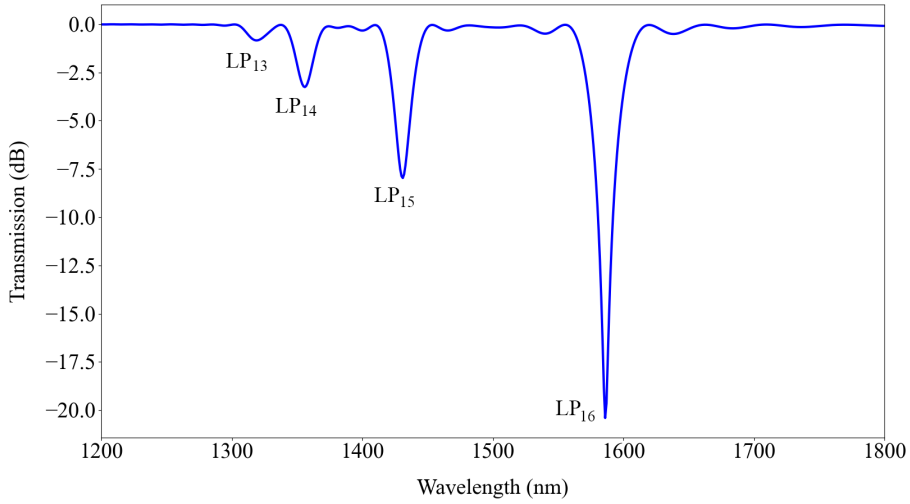

FIGURE 3.4: Simulated transmission spectrum of LPFG using TMM and CMT.

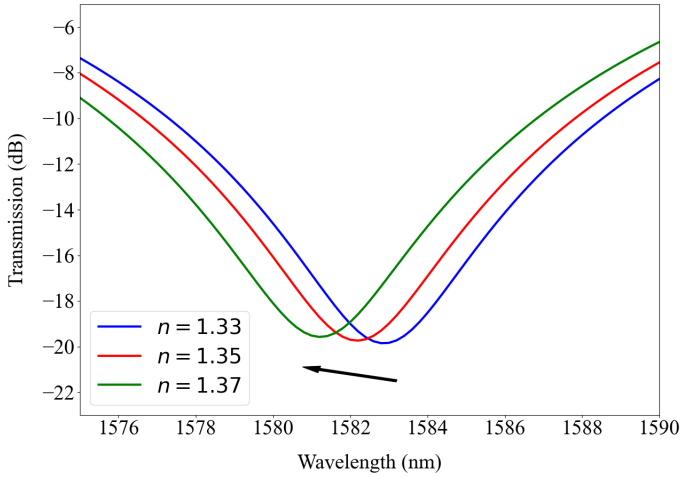

Figure 3.5: Spectral response of the simulated LPFG's LP_{16} mode to an external RI variation.

3.2 Stacks of Metals and Dielectrics

3.2.1 Transfer Matrix Formalism

The propagation of light in 1D layered media can be accurately described by using the Transfer Matrix Method, which takes advantage of the linearity of the fields between layers. This provides a simple matricial formalism that can be implemented numerically to obtain the response of a multilayer structure to an incident wave, which can include SPR and effects of other surface waves, when the conditions for their generation are met [103].

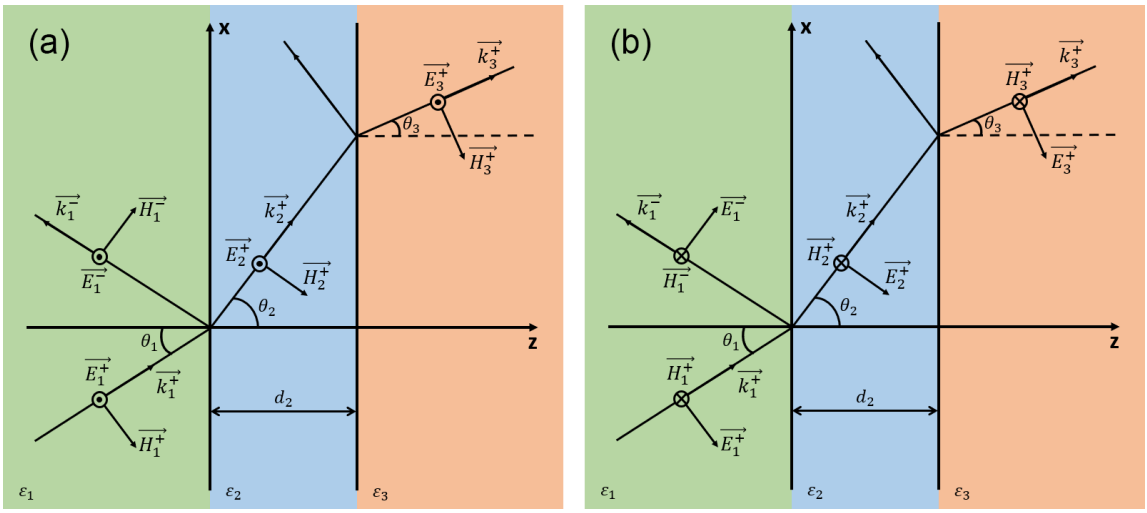

Figure 3.6: Reflection and transmission of electromagnetic waves at an interface between different materials. (a) S-polarized light; (b) p-polarized light;

If we consider the case of a p polarized wave on an interface between two materials of permittivity ε_1 and ε_2, represented in figure 3.6 where the vector's superscript $+$ and $-$ indicate whether the propagation is in the positive or negative z direction, respectively, and the subscript corresponds to the propagation medium, the electric and magnetic fields have the following components:

$$\begin{aligned} \vec{E} &= (E_x, 0, E_z) \\ \vec{H} &= (0, H_y, 0) \end{aligned} \tag{3.20}$$

The tangential components of the fields at the interface has to be continuous [104], therefore:

$$\begin{aligned} E^+_{x,1} + E^-_{x,1} &= E^+_{x,2} \\ H^+_{y,1} + H^-_{y,1} &= H^+_{y,2} \end{aligned} \tag{3.21}$$

For a plane wave, the fields have the following relation:

$$\vec{k} \times \vec{H} = \frac{-\varepsilon_1 \omega}{c} \vec{E} \tag{3.22}$$

so if the travelling wave has this property, from the field components of the polarized wave in equation 3.20 results:

$$\begin{aligned} \varepsilon \omega E^+_x &= k_z H^+_y \\ \varepsilon \omega E^-_x &= -k_z H^-_y \end{aligned} \tag{3.23}$$

and the continuity condition in 3.21 can be rewritten as:

$$\frac{\varepsilon_1 \omega}{k_{z,1}} E^+_{x,1} - \frac{\varepsilon_1 \omega}{k_{z,1}} E^-_{x,1} = \frac{\varepsilon_2 \omega}{k_{z,2}} E^+_{x,2} - \frac{\varepsilon_2 \omega}{k_{z,2}} E^-_{x,2} \tag{3.24}$$

Equation 3.24 can be manipulated to be presented in the matrix form, giving a relation between the tangential component of the magnetic field in the different materials [103]:

$$\begin{pmatrix} H^+_2 \\ H^-_2 \end{pmatrix} = M^p \begin{pmatrix} H^+_1 \\ H^-_1 \end{pmatrix}, \quad M^p = \frac{1}{2} \begin{pmatrix} 1 + \frac{\varepsilon_2 k_{z,1}}{\varepsilon_1 k_{z,2}} & 1 - \frac{\varepsilon_2 k_{z,1}}{\varepsilon_1 k_{z,2}} \\ 1 - \frac{\varepsilon_2 k_{z,1}}{\varepsilon_1 k_{z,2}} & 1 + \frac{\varepsilon_2 k_{z,1}}{\varepsilon_1 k_{z,2}} \end{pmatrix} \tag{3.25}$$

Analogously, the condition for the s polarization can be obtained through the same procedure:

$$\begin{pmatrix} E_2^+ \\ E_2^- \end{pmatrix} = M^s \begin{pmatrix} E_1^+ \\ E_1^- \end{pmatrix}, \quad M^s = \frac{1}{2} \begin{pmatrix} 1 + \frac{k_{z,1}}{k_{z,2}} & 1 - \frac{k_{z,1}}{k_{z,2}} \\ 1 - \frac{k_{z,1}}{k_{z,2}} & 1 + \frac{k_{z,1}}{k_{z,2}} \end{pmatrix} \tag{3.26}$$

Equations 3.25 and 3.26 can describe the refraction and reflection phenomena at an interface, and since the fields of consecutive media are related only through a matrix, it can easily be scaled to a multilayer structure. While only p polarized light generates SPPs, the simulated structures might only accept non-polarized light or the effect of both polarizations might be of interest, so in the following description Ψ will be used to generalize the TMM formulation, representing either the electric or magnetic field depending on the polarization.

The M matrix describes the changes in the fields at an interface, but the effects of the propagation inside a material cannot be neglected, as they add a phase to the wave, that not only results in attenuation but also highly influences the SPR. In the TMM formalism, it can be introduced through an additional matrix:

$$P_j = \frac{1}{2} \begin{pmatrix} exp(ik_{z,j}d) & 0 \\ 0 & exp(-ik_{z,j}d_j) \end{pmatrix} \tag{3.27}$$

where d_j is the thickness of the layer j and $k_{z,j}$ the normal component of the wavevector, $k_{z,j} = \sqrt{(\omega/c)^2\varepsilon_j - k_{x,j}^2}$.

The results in equations 3.25, 3.26 and 3.27 can be combined to obtain the transfer matrix of N layers 1D structure, which relates the incident and transmitted waves:

$$\begin{pmatrix} \Psi_N^+ \\ \Psi_N^- \end{pmatrix} = \prod_{i=1}^{N-1} M_{i,i+1} P_{i+1} \begin{pmatrix} \Psi_1^+ \\ \Psi_1^- \end{pmatrix} = M \begin{pmatrix} \Psi_1^+ \\ \Psi_1^- \end{pmatrix} \tag{3.28}$$

3.2.2 Spectra Simulation

The relation in equation 3.28, using the TMM formalism, allows for a simple computational calculation of the reflection, transmittance and absorbance of the multilayer structure, given the thickness and RI of each layer.

For a N layer structure, an incident wave of amplitude Ψ_1^+ is reflected, resulting in a backwards propagating wave of amplitude Ψ_1^-, and also transmitted, generating a forward propagating wave with amplitude Ψ_N^+. The reflection and transmission amplitudes can then be written as [103]:

$$\begin{aligned} r &= \frac{\Psi_1^-}{\Psi_1^+} \\ t &= \frac{\Psi_N^+}{\Psi_1^+} \end{aligned} \tag{3.29}$$

Since there is no backwards propagating wave in the layer N, their amplitudes have the following relation:

$$\begin{pmatrix} \Psi_N^+ \\ 0 \end{pmatrix} = M \begin{pmatrix} \Psi_1^+ \\ \Psi_1^- \end{pmatrix}, \quad M = \begin{pmatrix} M_{11} & M_{12} \\ M_{21} & M_{22} \end{pmatrix} \tag{3.30}$$

and the amplitudes of the reflected and transmitted waves can then be rewritten using the TMM formalism:

$$\begin{aligned} r &= -\frac{M_{21}}{M_{22}} \\ t &= \frac{M_{11}M_{22} - M_{12}M_{21}}{M_{22}} = \frac{\det M}{M_{22}} \end{aligned} \tag{3.31}$$

Since optical power is the parameter usually measured experimentally, we can define the reflectance and the transmittance as ratios of energy instead of the field's amplitude [103]. The waves are sinusoidal in time, so its power is given by the average time-averaged Poynting vector, $\vec{S} = \frac{c}{8\pi}\mathrm{Re}\{\vec{E} \times \vec{H}^*\}$, and using equation 3.22 the energy flow perpendicular to the plane can be written as:

$$S_{z,j}^+ = \frac{c}{8\pi}\mathrm{Re}\{\vec{E}_{x,j}^+ \times \vec{H}_{y,j}^{+*}\} = \frac{c^2}{8\pi}\frac{\mathrm{Re}\{\vec{k}_{z,j}\}}{\varepsilon_j \omega}|H_{y,j}^+|^2 \tag{3.32}$$

which can be used to define the reflectance:

$$R = \frac{S_1^-}{S_1^+} = \frac{|\Psi_{y,1}^-|^2}{|\Psi_{y,1}^+|^2} = |r|^2 = \left|\frac{M_{21}}{M_{22}}\right|^2 \tag{3.33}$$

While only one equation is needed to describe the reflection of both light polarizations, different expressions are needed for the transmittance:

$$T^p = \frac{S_N^+}{S_1^+} = \frac{\varepsilon_1}{\varepsilon_N}\frac{\mathrm{Re}\{k_{z,N}\}}{\mathrm{Re}\{k_{z,1}\}}|t|^2 = \frac{\varepsilon_1}{\varepsilon_N}\frac{\mathrm{Re}\{k_{z,N}\}}{\mathrm{Re}\{k_{z,1}\}}\left|\frac{\det M}{M_{22}}\right|^2 \tag{3.34}$$

$$T^s = \frac{S_N^+}{S_1^+} = \frac{\mathrm{Re}\{k_{z,N}\}}{\mathrm{Re}\{k_{z,1}\}}|t|^2 = \frac{\mathrm{Re}\{k_{z,N}\}}{\mathrm{Re}\{k_{z,1}\}}\left|\frac{\det M}{M_{22}}\right|^2 \tag{3.35}$$

Equations 3.33, 3.34 and 3.35 can be used to calculate the reflectance and transmission of a plane wave at a multilayer structure, which requires building its transfer matrix. This can simulate the effects of surface waves, including SPPs, and if done for different wavelengths, the reflection and transmission spectra can be obtained. It is also common to measure the absorbance of the structure, given by [105]:

$$A(\lambda) = 10 \log_{10} \frac{I_0}{I(\lambda)} \tag{3.36}$$

where for sensing in aqueous environments, the relation $I_0/I(\lambda)$ can be estimated by comparing the reflection in the air and water, $I_0/I(\lambda) = R_{air}/R_{water}$, similarly to what is done experimentally through a reference.

These spectra calculations assume light is incident at a specific angle, which is not the case in experimental setups, either due to imperfect sources or the structures used in the excitation, which results in wider SPR bands.

In the Kretschmann configuration, even if a collimator is used, there is a slight spatial broadening of the light which cannot be neglected when simulating the SPR. This effect can be compensated numerically by assuming a uniform power distribution throughout N light rays with incident angles in between θ_i and θ_f. Calculating the reflectance for each, their average results in a more realistic estimation of the optical response. This discretization process is given by the following equation [106]:

$$R_{\text{Kretschmann}} = \frac{\sum_{\theta_i}^{\theta_f} R(\theta)}{N} \tag{3.37}$$

When simulating fibers with a large diameter, we can assume light rays travelling from the critical angle, $\theta_c = \sin^{-1}(n_{cladding}/n_{core})$ to $90°$, which need to be considered. For $N(\theta) = L/(D \tan(\theta))$ light reflections at the metallic interface, the normalized transmittance can be expressed as [101]:

$$T_{fiber} = \frac{\int_{\theta_c}^{\pi/2} R^{N(\theta)}(\theta) P(\theta) d\theta}{\int_{\theta_c}^{\pi/2} P(\theta) d\theta} \tag{3.38}$$

where $P(\theta) = (n_{core}^2 \sin(\theta) \cos(\theta))/(1 - n_{core}^2 \cos^2(\theta))$ is the modal power for the angle of incidence θ. This expression can also be discretized for a numerical implementation.

For the simulation of light propagation in SMFs, the TMM is not adequate, since the geometrical optics theory is not valid for fibers with lower diameter than the light's wavelength. However, the phenomena behind SPP excitation in a side-polished fiber is similar

to that of a planar structure in the Kretschmann configuration, and therefore the same methodology can be used to obtain a decent approximation of the SPR band position and sensitivity, with an adjustment of the incident angles if needed. For more accurate results other simulation techniques are needed, such as the complex mode expansion and propagation method [107] or a more flexible numerical implementations like the finite-difference time-domain (FDTD) method.

A Graphical User Interface

A Python code was previously developed to simulate the optical response of 1D multilayer structure in the Kretschmann configuration, using the theory presented in subsections 3.2.1 and 3.2.2 [106]. It was slightly adjusted to create a graphical user interface (GUI) using Tkinter and CustomTkinter, allowing a fast and intuitive simulation of SPR bands. Its design can be seen in figure 3.7.

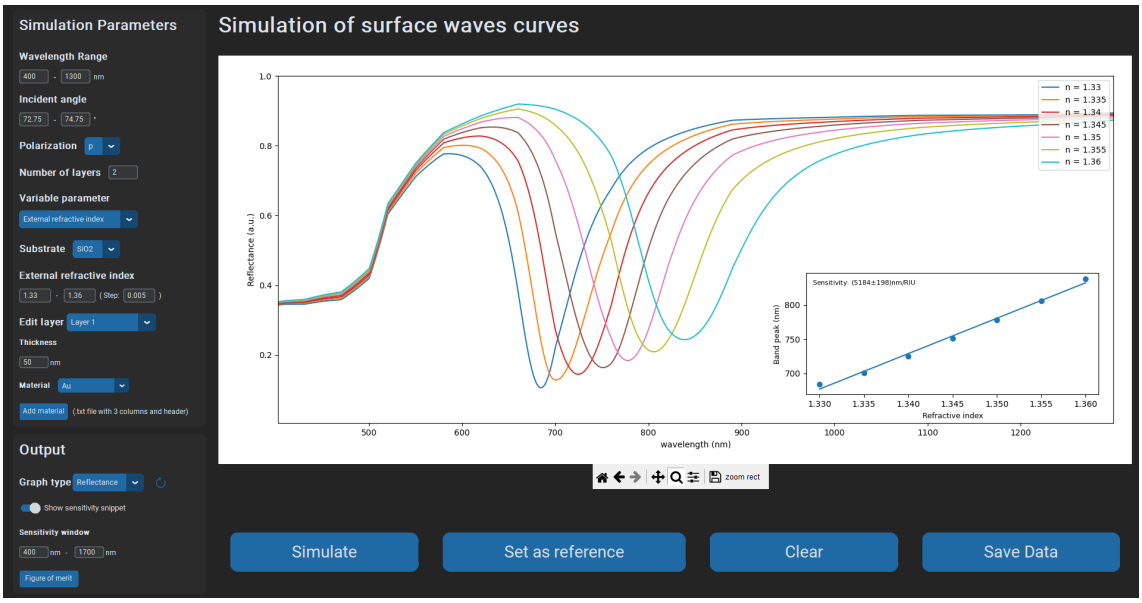

Figure 3.7: Graphical User Interface for the simulation of SPR bands on an arbitrary planar multilayer structure.

In the interface, the incident light wavelength range and polarization (p, s, and non-polarized) can be defined, as well as the incident angles boundaries, for broadening compensation. There is also an option to select the prism/substrate material, between silica and BK7 glass.

Each layer of the structure is customized individually by selecting its material, from a list of popular plasmonic metals and dielectrics or importing a new one from a text file, and

by defining the layer thickness. Since the most relevant use of the interface is to simulate the response of the structure to variations in the external refractive index, the basis of most plasmonic sensors, as well as optimize a sensing structure by finding the ideal thickness of its films, there is an option to choose a variable parameter (the thickness of one of the layers or the external refractive index) that when selected calculates the resonance bands over a defined range of that parameter.

The simulation results are presented in an interactive plot, which can show the reflectance, transmittance or absorbance of the optical structure and store previous results as a reference. Furthermore, if the external RI is selected as the variable parameter, the minima of the bands are located and used to calculate the sensitivity through a linear regression, and an approximation of the figure-of-merit is also calculated. The data can be saved on a text file if further manipulation is intended.

3.2.3 SPR sensing structure optimization

When designing a sensing structure based on SPR and using spectral interrogation, one of the most relevant features to consider is its sensitivity to the external medium refractive index, n_{ext}. Since the bands shift due to a change of the effective refractive index, n_{eff}, the sensitivity can be defined as:

$$S_n = \frac{\partial \lambda_r}{\partial n_{ext}} = \frac{\partial \lambda_r}{\partial n_{eff}} \frac{\partial n_{eff}}{\partial n_{ext}} \tag{3.39}$$

To denote the overall quality and resolution of the sensor, a universal parameter, applicable to all plasmonic sensing structures, is needed. For that, we can take into account the spectral width of the band through its full width at half maximum (FWHM), which can be used to define the Figure of Merit (FoM):

$$\text{FoM} = \frac{S_n}{\text{FWHM}} \tag{3.40}$$

A higher FoM is indicative of a better sensor, either due to a higher sensitivity or a lower FWHM. The latter represents a sharper band, resulting in lower uncertainty when acquiring the resonance wavelength.

Table 3.1: Simulated parameters of traditional SPR structures in the Kretschmann configuration

Sensing Structure	Resonance Wavelenght @ 1.333 RI (nm)	Simulated Sensitivity (nm/RIU)	Simulated FOM	
			n	FOM
50nm Ag	599	4500 ± 100	1.33	78
			1.34	70
			1.35	55
50nm Ag / 20nm SiO_2	680	5700 ± 200	1.33	91
			1.34	80
			1.35	56
40nm Ag / 40nm TiO_2	1257	10400 ± 200	1.33	82
			1.34	66
			1.35	56
50nm Au	694	4800 ± 100	1.33	72
			1.34	54
			1.35	47
40nm Au / 40nm TiO_2	1305	11100 ± 300	1.33	65
			1.34	55
			1.35	46
50nm Cu	686	4300 ± 200	1.33	71
			1.34	46
			1.35	36

A Plasmonic Materials

As previously mentioned, from equation 2.10 we can conclude that plasmons can only be generated in materials with a negative permittivity, which imposes a strict restriction in the plasmonic structures. This condition is typically met by materials with a high plasma frequency and electrical conductivity, properties of metals, making them the materials of choice for SPR generation.

Alkali metals have the lowest optical losses, so theoretically they produce the best SPR bands [108], but since they are highly reactive in water and air, no sensing applications using these materials have been found. Low losses noble metals (silver, gold and copper) then become the optimal materials for plasmonic sensors, and the metrics for some of the most popular structures can be found in table 3.1. Among them, while silver doesn't have the higher sensitivity, its narrow resonance band gives it a great FOM, making it the best

performing choice. The problem with silver is how fast it degrades, creating the need for a protection layer, usually made of silica or gold [109], capable of increasing the structure sensitivity while maintaining sharp peaks. Nevertheless, the chemical stability of gold in most environments and over a long period of time is an alluring characteristic that compensates the lower performance of the material. These two metals are still the most used in experimental work, since copper, while capable of decent results, also oxidizes easily providing no advantage over silver or gold, and platinum and palladium have high optical losses, only finding application when their chemical interactions are of interest [110]. Due to inter-band transitions, aluminum is only attractive in the UV region, where the permittivity of silver and gold is positive [111].

B Effect of metal thickness in the SPR band quality

Plasmonic metals have optical losses that cannot be neglected when designing a sensor. They affect the SPPs, so the thickness of the metallic layer will modify the wave attenuation, therefore changing the SPR response curve. This effect can be incorporated in the TMM simulations by including the complex component of the materials RI, resulting in the bands represented in figure 3.8.

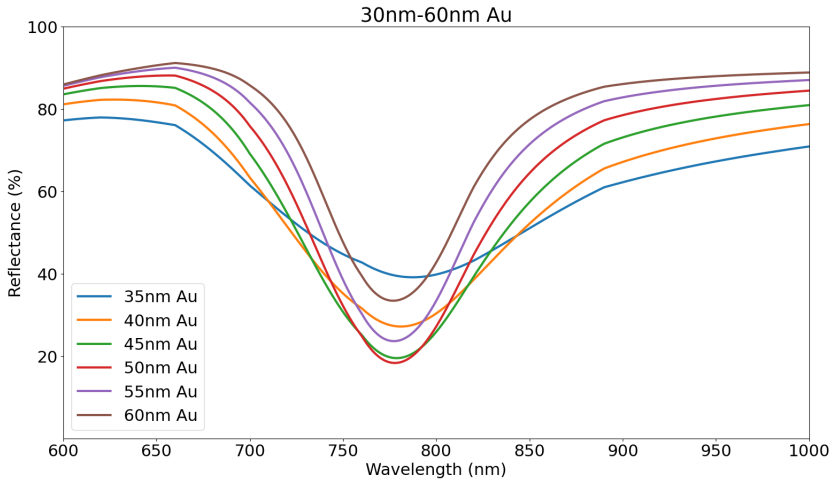

Figure 3.8: Simulated SPR bands for different gold film thicknesses (1.333 external RI).

For thicknesses higher than the optimal value, around 50nm, we can observe that an increase of the film thickness results in a lower reflectivity, which is the expected response since the optical losses due to the material also increase. At low metal thicknesses, this behavior does not occur. For these values, the losses due to electron-grain boundary scattering are much larger, and they increase for lower thicknesses. As they also dampen

the resonance bands, an optimal thickness for the sensor can then be found when the losses due to both phenomena is minimal [112, 113].

C Effect of conducting metal oxides overlays in the SPR band

The operating wavelengths of most SPR sensors are in the visible spectrum range, since they use silver, gold or a combination of both. To make use of different experimental setups or for multiplexing applications, there is often the need to shift the resonance bands to the near infrared (NIR) region. This can be done by adding layers of conducting metal oxides like TiO_2 [114], indium tin oxide (ITO) [115] and ZnO [116], since they have a lower carrier concentration (lower plasma frequency) than the plasmonic metals and a high RI. These properties result in a small increase of the spectral width, while simultaneously increasing the penetration depth of the surface plasmon wave and its sensitivity to the external RI. Titanium dioxide materials are the most widely adopted option, as they have high electrochemical stability and resistance to corrosion. The simulated shift of the resonance bands due to TiO_2 layers of different thicknesses is presented in figure 3.9.

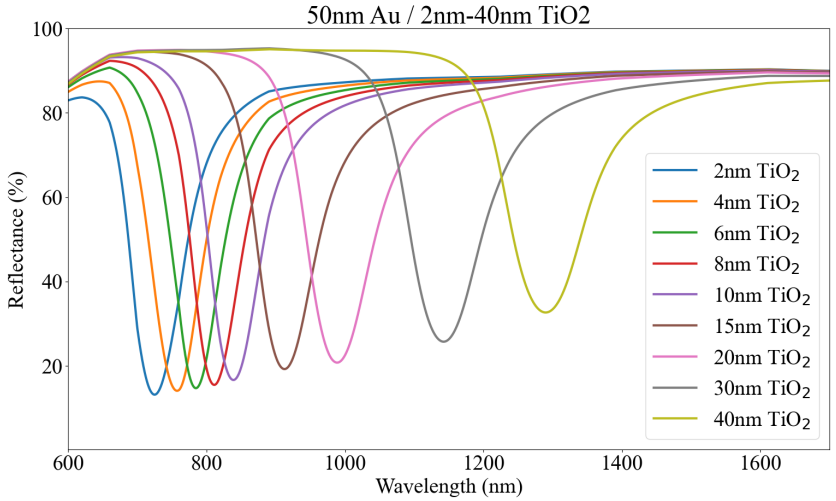

Figure 3.9: Simulated SPR bands of a 50nm gold film with a TiO_2 overlay with various thicknesses (1.333 external RI).

Chapter 4

Materials and Methods

Sections 4.1 and 4.2 describe the experimental setups used for the fabrication of the LPFGs and thin films on a planar substrate, respectively. The setup used for SPP excitation with the fabricated plasmonic structures on planar substrates is presented in section 4.3.

In section 4.4, the procedure done for the fabrication and characterization of an optical pH sensor is presented. The LbL technique was used to deposit a polyethylenimine (PEI) and polyacrylic acid (PAA) multilayer thin film. PAA is a pH sensitive polyanion and PEI a common polycation that, with a tuning of the deposition solutions pH, can be combined to achieve thick films, when compared to other LbL coatings [117, 118]. The effect of this coating on an LPFG was studied thoroughly. Additionally, the deposition was also made on an LPFG coated with titanium dioxide, that has an improved wavelength sensitivity over a bare LPFG due to a higher effective refractive index [23], and in a gold thin film in a planar substrate that supports SPR. Furthermore, the polymeric coating was characterized by comparing the experimental data from the LPFG to that of a Fabry-Perot (FP) cavity on a fiber tip [119], produced with a similar coating, and to simulation results.

Aptamers are short sequences of artificial DNA, RNA, XNA, or peptide that exhibit a strong specificity for a target molecule, by binding to its complementary chain. They can be immobilized onto a plasmonic metal so that when they bind with the target molecules, the SPP interaction can be used to detect their presence due to an increase of the effective refractive index. In section 4.5, the procedure for the fabrication and of an aptamer-based SPR sensor for the detection of glyphosate, using a thin gold film and the Kretschmann configuration, is presented.

4.1 LPFG Fabrication

Since the grating period of an LPFG is in the order of hundreds of micrometers, several techniques have been used to fabricate them. UV light exposure was the first method used to produce these structures [9], as its setup was similar to the ones already implemented for FBG production, and it remains as a popular option that has been improved to increase reproducibility [120]. Other techniques include using CO_2 laser radiation [121], femtosecond laser radiation [122], focused ion-beam irradiation [123], ion beam implantation [124], etching [125], mechanical pressure [126], and electric arc discharges [127].

Each fabrication method has its advantages and disadvantages, but an important distinction between is the RI profile they originate, since it can change which cladding modes are coupled to the core mode [128]. Photo-induced techniques usually make use of a beam focused on the fiber core, only modulating the RI in that area and therefore creating a symmetric LPFG whose RI profile along the fiber axis is described by:

$$n(z) = n_{co}(1 + \sigma(z)[1 + M\cos(2\pi z/\Lambda)]) \tag{4.1}$$

where $\sigma(z)$ is a slowly varying envelope, M is the amplitude of modulation of the induced RI in the grating or grating visibility, and Λ is the grating period.

Electric-arc and mechanically induced LPFGs are examples of asymmetric structures, which also have a perturbation of the cladding RI. This creates an angular dependency of the RI profile:

$$n(z) = n_{co}(1 + \sigma(z)M\sin(\varphi)\cos(2\pi z/\Lambda)) \tag{4.2}$$

4.1.1 Electric-arc Induced Fabrication

The electric-arc technique has multiple applications, from fiber fusion splicing to the production of fiber tapers, fiber couplers and microspheres [129]. The first demonstration of this method applied to LPFG fabrication was presented in 1994 by Poole et al. [35] in a two-step process which involved the ablation of the cladding of a two-mode fiber by CO_2 laser radiation followed by an annealing through arc discharges. In 1997 LPFG fabrication using only electric-arc discharges was presented by Dianov et al. [130].

Electric-arc induced LPFG fabrication consists in the application of electric-arc discharges on a fiber, aligned between two electrodes. It is a point-to-point process, where

after each discharge the fiber is displaced by a fixed distance, the grating period, usually through a translation stage. The number of points inscribed dictates the sensing region length. Since this method changes the RI of the fiber core and cladding, the structure is visible to the naked eye, as seen in figure 4.1.

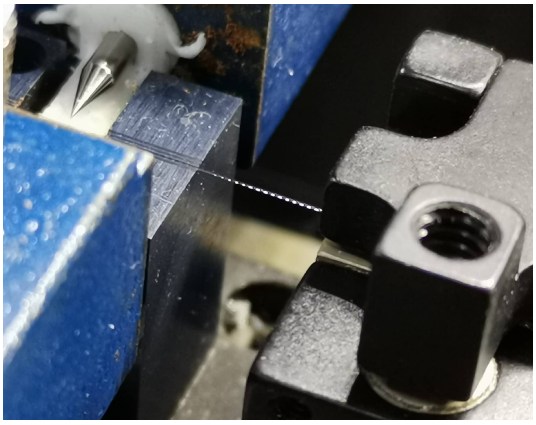

Figure 4.1: Photograph of an LPFG after fabrication using the electric-arc technique

Compared to other methods, this technique is simpler, making it low cost and flexible. It can induce gratings in any kind of fiber with high reproducibility without requirements such as a photosensitive fiber or the need for it to be hydrogen treated and thermal annealed, as is the case for the ones induced by UV-laser radiation [127]. Similar to photo-induced LPFGs, electric-arc induced LPFGs can also tolerate very high temperatures, an essential property for monitoring applications under extreme conditions [131].

4.1.2 Experimental Fabrication Setup

The LPFGs used in the work of this thesis were made through the electric-arc technique, as described by Rego et al [128]. The experimental setup is shown in figure 4.2. It consists of a linear translation stage connected to a microcontroller, with a precision of 0.1µm, where the fiber is secured with the help of a pulley, two clamps and a magnetic weight, to keep it under tension. The electrodes of a BICC AFS3100 fusion splicer machine were repurposed for this implementation, and the discharge parameters (current and discharge time) were previously optimized for LPFG fabrication. The electrodes were placed 1mm apart in a 2D translation stage with micrometer screws, so that with the help of a microscope placed above them the fiber position could be adjusted. Placing it in between the electrodes and at their height is essential to produce a good grating.

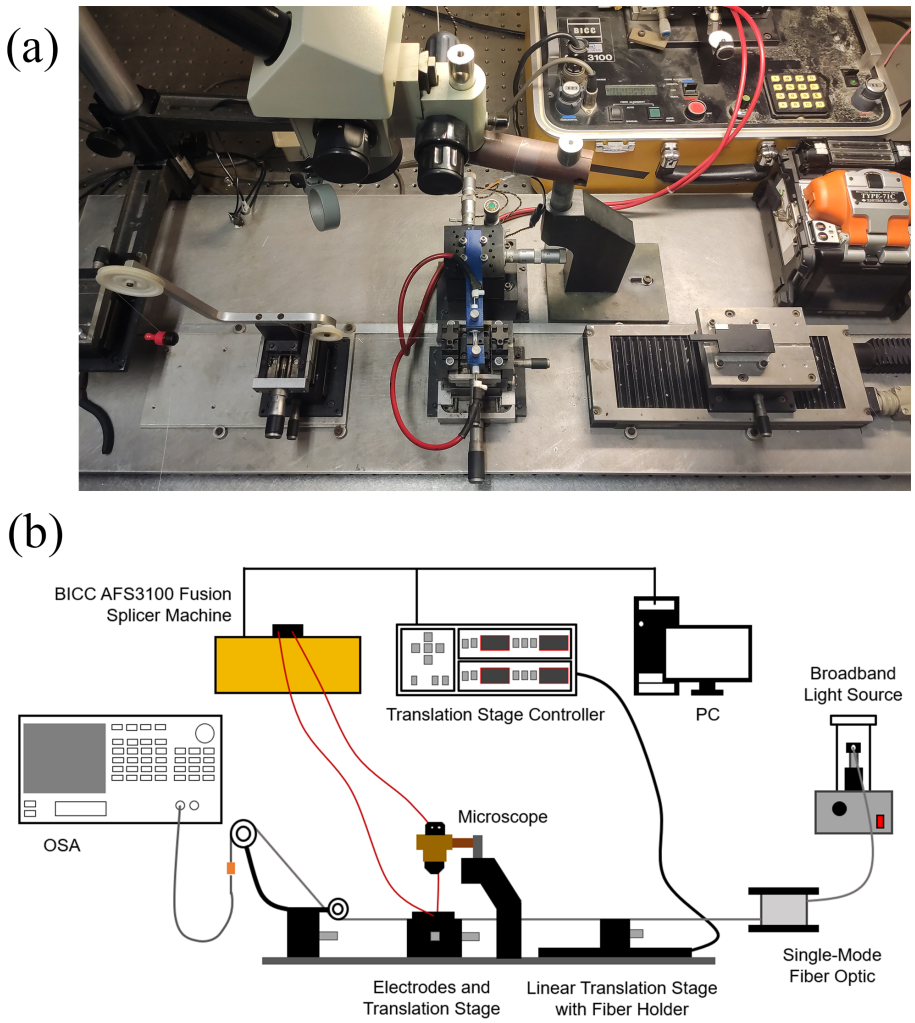

Figure 4.2: Experimental setup for LPFG fabrication using the electric-arc technique. (a) Setup photograph; (b) schematic diagram

The electrodes are made of tungsten doped with thorium, and need to be replaced after some uses due to exposure to silica particles and oxidation but can be reused after polishing. During fabrication the fiber is connected to a broadband light source and an Optical Spectrum Analyzer (OSA) to track the band evolution with each discharge.

The splicer machine and stage microcontroller are connected to a computer with a LabVIEW software that automates the fabrication process and allows the definition of the number of discharges and the grating period. The fabrication procedure consists in stripping the jacket of a standard SMF in the region where we want to imprint the grating, placing it between the electrodes while under tension and then connecting the fiber to the OSA. After that, we only need to use the software to carefully start the discharges until the desired attenuation peak is achieved (around -20dB for the LP_{16} mode).

4.2 Thin Film Deposition

To generate plasmons, metallic films with thicknesses in the order of tens of nanometers are required, which also means that deposition techniques with nanometer resolutions are needed. This requirement was one of the reasons that the increase of the interest in plasmonic technologies was only observed in the last decades, following the improvement of nanofabrication techniques.

Since a variety of techniques can be used to fabricate thin films using a large diversity of materials, structures can be produced with materials that are highly sensitive to a specific substance or chemical parameter. This makes thin film fabrication highly relevant for optical sensing, as the light interaction with the film can be taken advantage of for tracking the film properties and their variation [132].

The thin film deposition techniques can be categorized into two broad categories, depending on whether the process is mainly physical or chemical [133]. Physical deposition uses mechanical, electromechanical, or thermodynamic methods to remove material from a target, and examples of these techniques are thermal and electron beam evaporation, sputtering and molecular beam epitaxy. They are usually applied to materials with high energy bonds such as metals and dielectrics and can require high vacuum. In chemical methods, a fluid suffers a chemical change at a solid surface, which will originate the film. Compared to the physical methods, they are attractive due to their relative affordability, simplicity, and suitability for large-area depositions, although additional parameters such as the pH, temperature and fluid properties must be controlled. Spin coating, dip coating, chemical vapor deposition and atomic layer deposition are some of the most popular chemical methods.

The deposition of the metal and dielectric thin films used in this work was done through Radio Frequency (RF) Magnetron Sputtering, while the polymeric films were fabricated using the Layer-by-layer (LbL) electrostatic self-assembly (ESA) method, both of which do not require a cleanroom environment.

4.2.1 RF Magnetron Sputtering Deposition

The RF magnetron sputtering method involves the creation of a plasma by applying an RF voltage that is able to ionize Argon molecules within a chamber. As a result of a significant voltage gradient being applied, these ionized atoms will accelerate towards the cathode

where the target material is, colliding with it. Since the collision energy is much higher than the required for the material evaporation, it will vaporize and consequently slowly move towards the substrates, as they are located in the anode. The material will then be deposited at a variable rate in the order of a hundred picometers per second (approximately one atomic layer per second). Figure 4.3 shows the typical components found in an RF magnetron sputtering chamber.

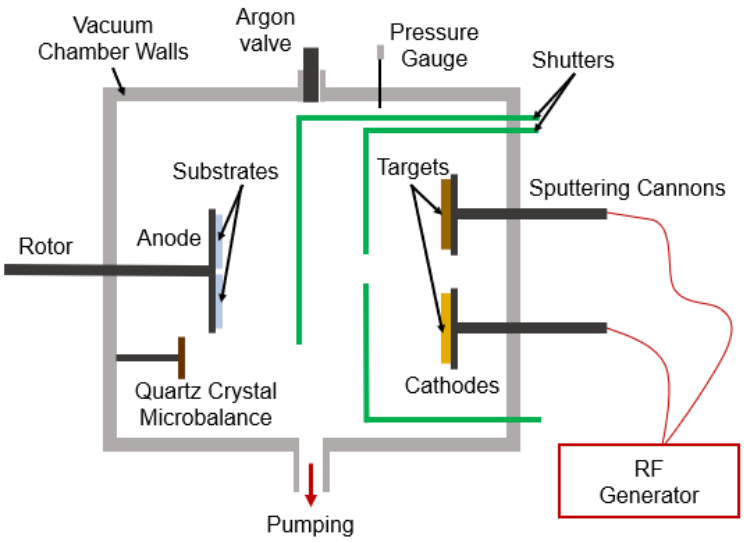

Figure 4.3: Schematic of the RF magnetron sputtering chamber.

The sputtering setup used and currently available at INESC-TEC facilities is shown in figure 4.4. The RF voltage is generated by an RF generator (CESAR RF Power Supply model 1312) connect to an impedance matching box. The impedance matching network is responsible for transmitting the majority of the generated energy to the target, minimizing wave reflection, as it can damage the RF generator. The need for this network comes from constant changes in variance due to variations of the pressure and temperature inside the chamber. By generating the RF voltage, a magnetron is achieved, which forces the electrons into helical paths, increasing the probability of collision and ionization of the Ar atoms, needed to create the plasma, and also redirecting the secondary electrons generated from the collisions of the ions with the targets to the ground shield, warding the substrates.

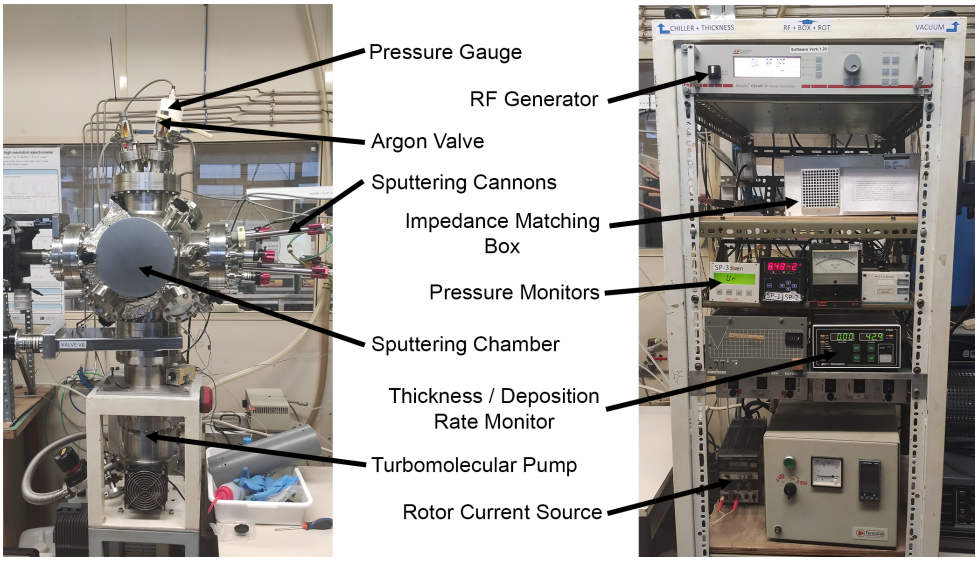

Figure 4.4: Picture of the RF magnetron sputtering system used for thin film deposition.

The vacuum inside the stainless-steel chamber is created by first using an attached primary pump (Edwards RV12), lowering the pressure to $\backsim 10^{-3}$mbar, and then a turbomolecular pump (Alcatel-Annecy 5400), supported by another primary pump, which allows pressures of $\backsim 10^{-6}$mbar. Two pressure gauges are used to monitor the vacuum so we can know when to open and close the valves, one inside the chamber and another between the turbomolecular pump and the supporting primary pump. The pressure gauge inside the chamber is a combo of a Pirani gauge (to measure pressures higher than $\backsim 10^{-2}$mbar) and a Penning gauge (for pressures lower than $\backsim 10^{-2}$mbar), that switches automatically between the two depending on the measured value. The pressure gauge between the turbomolecular and primary pump is a Pirani gauge. The flux of Argon gas is controlled manually by a precision valve connected to a gas cylinder, which allows pressure regulation. Given that in sputtering processes approximately 75% of the energy is dissipated as heat in the target, a water-cooling system with a chiller is used for refrigeration.

Two sputtering sources, cathodes (Meivac MAK 2”), are available to use in this system. They are connected with a switch to the impedance matching box, allowing an easy change of material to deposit. Both of them and the anode have an individual shutter in front of them, that can be easily opened and closed to prevent unwanted material removal and deposition, giving control of when the processes start.

The setup also allows the deposition of two substrates simultaneously, but since two cathodes are used, the distance of each substrate to the targets is different, which would cause the deposition of different layer thicknesses depending on where each structure

was positioned. To prevent this, the anode and substrate support is rotated at a constant rate by a motor connected to a current source.

To monitor the deposited thickness, a quartz crystal microbalance is used. Changes in the crystal resonator frequency can be translated in mass variation per unit area, that can then be converted to thickness when the acoustic properties of the deposited material are known. As the quartz crystal is not at the same position as the substrates, the measured and real deposition rates are not the same, so a calibration was made by producing a film with a fixed thickness measured by the monitor and doing a Scanning Electron Microscopy (SEM) analysis to obtain the real value.

The substrates used in the fabrication of structures in a planar geometry were cleaved microscope slides. Ideally, pure silica substrates should be used to minimize light refraction, since silica optical prisms were used experimentally. Nevertheless, great results were obtained without them.

To minimize the residue in the substrates, preventing possible adhesion problems, the following protocol was used to clean them: first 5 minutes ultrasonic bath in acetone was performed, then they were placed in isopropyl alcohol and in the ultrasonic bath for another 5 minutes, and finally 5 minutes ultrasonic bath in deionized (DI) water. After that, they were dried with nitrogen and carefully stored.

The optimal values for the sputtering system when depositing the materials used in this work were previously investigated. First a pressure of $\backsim 5 \times 10^{-5}$mbar was achieved using the turbomolecular pump, and then increased to $\backsim 8 \times 10^{-3}$mbar by injecting Argon to achieve the plasma. To deposit metals, a low power is enough (10W for gold deposition), but dielectrics require a much higher power (110W for TiO_2).

For certain materials such as gold, they have small adhesion to glass substrates, which causes the deposition of islands instead of a thin film. This problem can be solved by depositing an adhesion layer with great adhesion to both the substrate and material. Chromium and Titanium films of $\backsim$ 3nm were used for this purpose.

4.2.2 Layer-by-Layer Electrostatic Self-Assembly

The layer-by-layer (LbL) electrostatic self-assembly (ESA) is a cyclical process for deposition of thin films of polymers and colloids, biological or synthetic. It is a process where a charged material is adsorbed onto a substrate and, after washing, an oppositely charged

material is adsorbed on the previous layer, constituting a single bilayer [134]. Each bilayer has a thickness generally on the order of nanometers, but the deposition process can be repeated multiple times until a multilayer film with the desired thickness has been achieved, as schematize in figure 4.5. Electrostatic interactions between the materials are what enables this process, but other molecular interactions such as covalent bonds and hydrogen bonding in hydrophobic and hydrophilic molecules cannot be neglected, and in some cases can be exploited to fabricate the film [135].

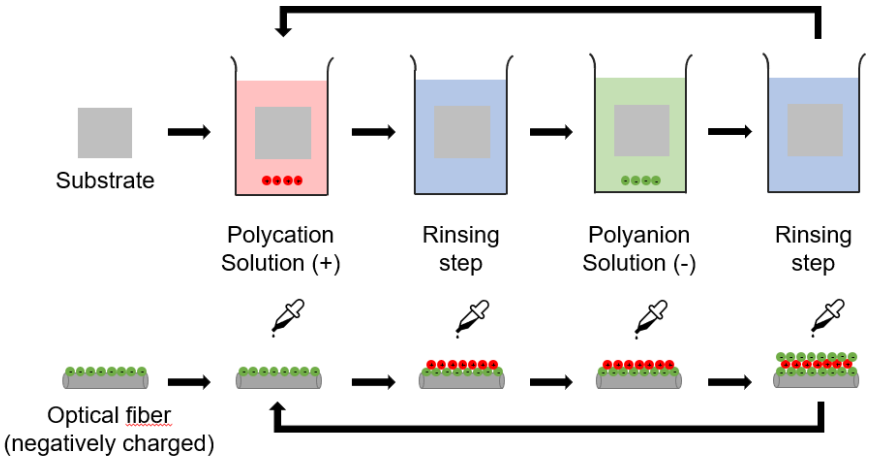

Figure 4.5: Schematic of the LbL self-assembly process.

The simplicity and versatility that the LbL technique provides is what makes it one of the most widely used technologies for thin film coating, but since it relies on molecular interactions, there are multiple parameters that can be used to manipulate the fabricated structure and must be controlled during the deposition to obtain reproducible results. These include the properties of the solutions used, their concentration, pH, salinity and temperature, as well as the time per layer, washing process, and the environmental conditions. To apply this method to different substrates using multiple materials, and to fabricate different structures with adjustable roughness, a large portfolio of techniques has been developed and automatized. Richardson et al. provide a good review of these methods [134].

In this work, the LbL technique was implemented by dipping the substrate in prepared solutions with the materials. For deposition in optical fibers, specifically in long-period fiber gratings, the sensing regions were placed on a Teflon groove where the solutions could be easily transferred into. It was fixed in a vertical lifting platform for an easy replacement of the solutions without the possibility of damaging the films. The setup can be seen in figure 4.6, where the fibers were also under tension and connectorized to a light source

and a spectral interrogator for real-time monitoring of the bands during the LbL deposition. The setup for fabrication in planar substrates was simpler, as it consisted in placing the structure in a beaker with a dipping solution and transferring it to new beakers with new solutions as needed. Since we only wanted the film on one side of the structure for it to be used in the Kretschmann configuration, Kapton tape was used to protect the other side, as shown in figure 4.6.

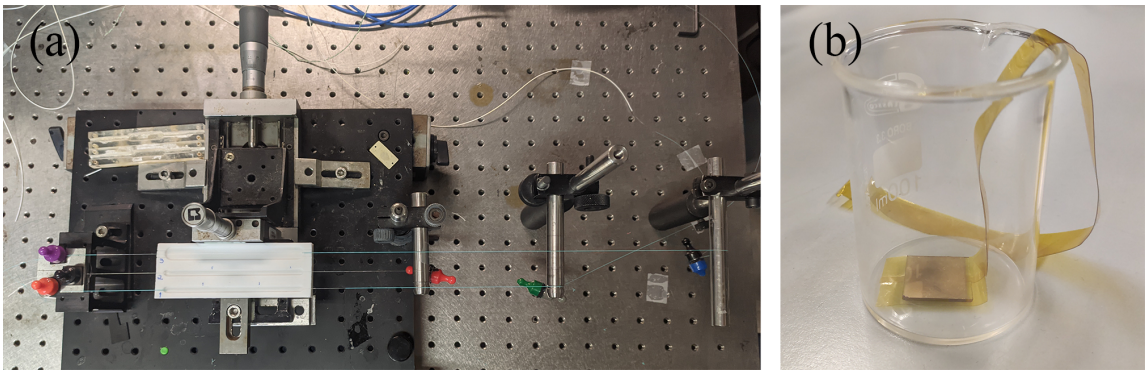

Figure 4.6: Picture of the experimental setups used for LbL deposition of thin films on (a) LPFGs (b) planar substrates

4.3 Experimental Setup for SPP Excitation

The setup represented in figure 4.7 was used to couple light to a thin film, exciting SPPs. Light is injected from a broadband Tungsten-Halogen light source (Sarspec LS-W) into a silica glass optical prism using a fiber optics patch cord, passing through a polarizer to achieve a p-polarized light. Both the prism and polarizer are placed on a 3D printed piece fabricated to hold them and to allow light incidence at an optimal angle of 74°. The sensing structure is placed on the prism, with a layer of index matching to eliminate the reflection losses in the air interfaces. The light is then reflected at the interface between the substrate and the external dielectric, and collected into an optical fiber connected to a spectrometer (Avantes AvaSpec-ULS2048CL-EVO) for detection in the visible spectral range.

For an easy exchange of the solutions on top of the sensing structure, a Teflon microfluidic chamber, seen in figure 4.8, was used. It presses against the substrate with an O-ring, to ensure no solution escapes the interaction area which would modify the measured band. The solution can be injected into the chamber using the tubes and syringes, and to ensure good washing steps, the setup is fixed vertically.

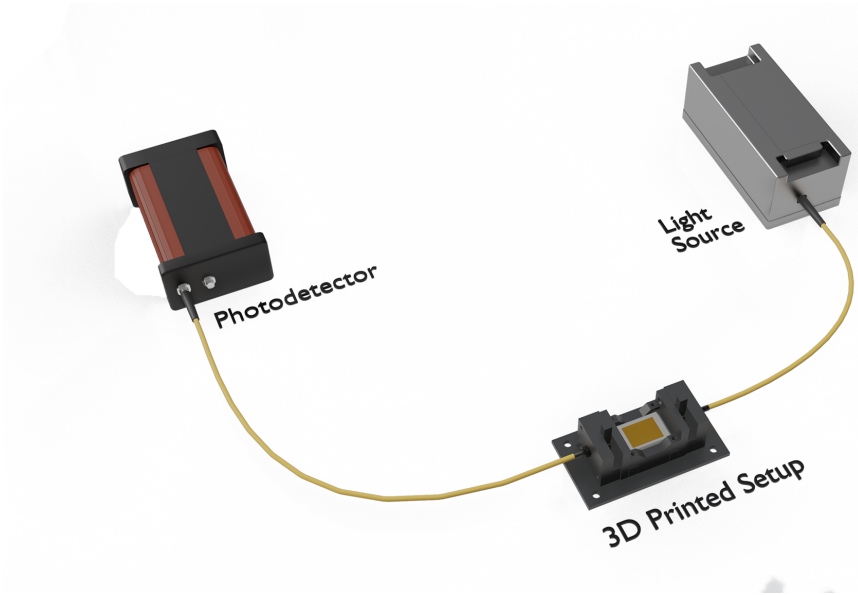

Figure 4.7: Schematic of the experimental setup for SPP excitation in a planar substrate (Kretschamnn configuration).

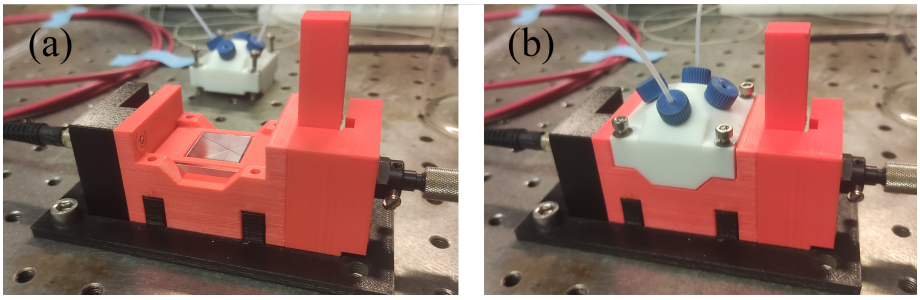

Figure 4.8: 3D printed piece for SPP excitation in planar substrates. (a) Without the microfluidic chamber on top of the prism; (b) with the microfluidic chamber

4.4 Fabrication and Characterization of an Optical pH Sensor Based on a Polymeric Nanocoating

4.4.1 Chemical Reagents

Polyethylenimine aqueous solution (PEI; 50% (w/v)), polyacrylic acid (PAA; Mv = 3000000), and sodium chloride (NaCl) were purchased from Sigma-Aldrich and were used for the polymeric coatings.

Hydrochloric acid, sodium hydroxide, sodium acetate, glacial acetic acid, sodium phosphate dibasic dihydrate, sodium phosphate monobasic monohydrate, Trizma® base ($\geq$ 99.9%), sodium bicarbonate and sodium carbonate were also purchased from Sigma-Aldrich and used to prepare the pH buffers.

4.4.2 Layer-by-Layer Electrostatic Self-Assembly of the Sensing Coating

The LbL fabrication technique was used to fabricate a coating of PEI and PAA on the following structures: an LPFG with attenuation around 20dB and peak in the 1500 to 1600nm wavelength range, a similar LPFG but with a 40nm TiO_2 coating, and planar substrate with a 3nm Cr / 50nm Au thin film.

Since PAA is a weak polyelectrolyte, the properties of the produced film, which include its thickness, depend greatly on the dipping solution pH [136], as this parameter modifies the polymer charge, which consequently affects the adhesion process. When the pH of the PAA dipping solution is low and the pH of the PEI solution is high, the ionization degree of both polymers is low, increasing their diffusion ability and resulting in a higher growth rate of the film. For this reason, to achieve a higher thickness coating with a low number of bilayers, the immersion solution of PAA was kept at an acidic level during the deposition on the LPFGs and was slightly increased for the fabrication on the planar substrate.

The experimental setup in figure 4.9 was used to deposit the pH sensitive polymeric coating in the LPFGs. The sensing region was kept under tension to assure a constant strain on the LPFG, and the fibers with the sensors were connected to a BraggMETER (FS22SI from HBK FiberSensing, Portugal, with 1pm of spectral resolution) using a fiber optic circulator to obtain transmission spectra using a reflection mode interrogator. This unit was connected to a personal computer with a developed software that enabled real-time monitoring of the measured spectra and peak tracking and analysis, with a timeline construction. The deposition in the planar substrates was done using beakers, as mentioned in section 4.2.2, which unlike the setup for the LPFGs does not enable band monitoring during the deposition.

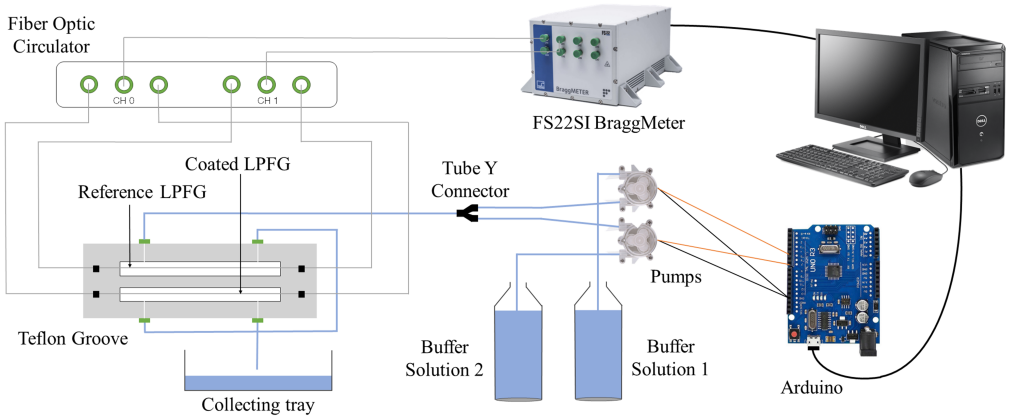

Figure 4.9: Schematic of the setup for real-time band monitoring during coating fabrication and to obtain the sensor spectral response to pH.

NaCl was dissolved in deionized (DI) water to obtain a 0.5M solution in which the PEI was diluted to a concentration of 0.1% and pH 10.1. For the coatings on LPFGs, a 0.6% PAA solution in sodium acetate buffer (pH 5.6) was used, resulting in a final solution with 4.9 pH. For the fabrication process on planar substrates, a 0.2% PAA solution was used instead, with the polymer being dissolved in a 6.2 pH phosphate buffer to obtain a dipping solution with 6.05 pH. Before use, the PEI solutions were stirred at room temperature for 2h and the PAA for 8h.

To produce the coating in the LPFG, the sensing fiber was first cleaned with acetone, while no pretreatment was done to gold surface. Since the silica fiber surface is negatively charged and PEI is a strong polycation whose adhesion to gold was verified experimentally through a SPR band shift, the same LbL fabrication procedure was implemented for all sensing structures. They were immersed in the PEI and PAA solutions alternately for 10 minutes, except for the first PEI monolayer where the immersion lasted 1h to ensure a homogeneous charge dispersion along the surface. After each monolayer was assembled, the sensing region was immersed for 1 min in specific cleaning solutions for PEI and PAA, DI water and a buffer solution, respectively. The washing process was repeated five times to ensure the removal of the excess of each polyelectrolyte between layers. After 2 bilayers, the structures were let to dry overnight at room temperature. A schematic of the structure fabricated on a LPFG can be found in figure 4.10, and scanning electron microscope (SEM) images of the LPFG before and after this deposition process are shown in figure 4.11, confirming the deposition of the polymers.

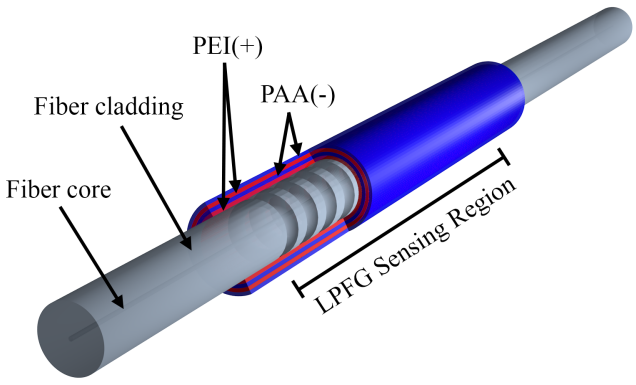

Figure 4.10: Schematic of the LPFG with the sensing coating.

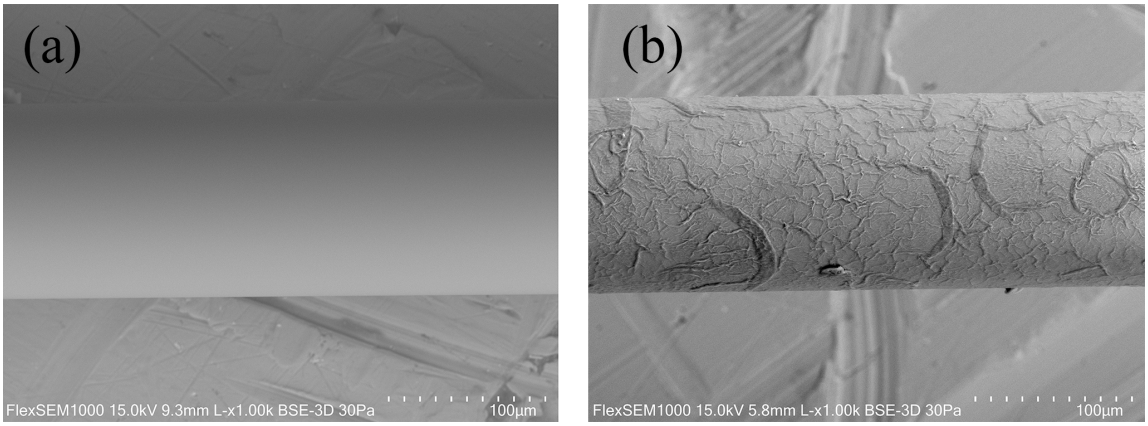

Figure 4.11: SEM images of (a) a bare LPFG (b) an LPFG coated with 2 PEI/PAA bilayers.

4.4.3 Sensor Spectral Response to pH

To obtain the response curve of the sensor to pH variations, different pH buffers in the 5.00-10 pH range were prepared to ensure the solutions stability [137], and their pH was measured with the commercial sensor HACH HQ40D.

The response curves for the LPFGs were obtained using the setup in figure 4.9 by sweeping from high pH values to low and the reverse. The response of the gold film SPR was done using the SPP excitation setup explained in section 4.3.

The coated LPFGs were also exposed to multiple successive cycles between 2 different pH buffers, performed using an automatic system, also presented in figure 4.9. It consists of a microfluidic chamber where the LPFGs were placed, connected to two small pumps for the injection of the solutions. The pumps were controlled by an Arduino and an interface on the same software that allowed real-time spectra measurements.

For the LPFGs measurements, another LPFG without the fabricated coating was simultaneously immersed in the same buffer solutions as the pH sensitive structure. Since the resonance wavelength of an LPFG also depends on the solution RI and temperature, a bare LPFG was needed as a reference during the measurements, to ensure that wavelength shifts observed for the sensor when changing the pH are only due to a variation of this parameter. The uncoated structure can then be used for temperature and RI compensation if relevant variations of its resonance wavelength are verified.

4.4.4 Optical Fiber Interferometer for the Measurement of the Polymeric Coating Refractive Index and Thickness

The experimental procedure to fabricate a PEI/PAA bilayer in the LPFG was used to deposit a 21 bilayers structure on a single-mode fiber tip with the setup represented in figure 4.12. The resulting thickness was enough to produce a low-finesse FP interferometer, whose reflection intensity I_R is given by the following equation:

$$I_R(\lambda) = R_1 + (1-\alpha)^2(1-R_1)^2R_2 - 2\sqrt{R_1R_2}(1-\alpha)(1-R_1)\cos(\omega) \tag{4.3}$$

where the Fresnel coefficients are $R_1 = (n_{core} - n_{pol})^2/(n_{core} + n_{pol})^2$ and $R_2 = (n_{core} - n_{ext})^2/(n_{core} + n_ext)^2$, α is the insertion loss factor and $\omega = (4\pi n_{pol}L)/\lambda$, L being the cavity length or the polymeric coating thickness [119].

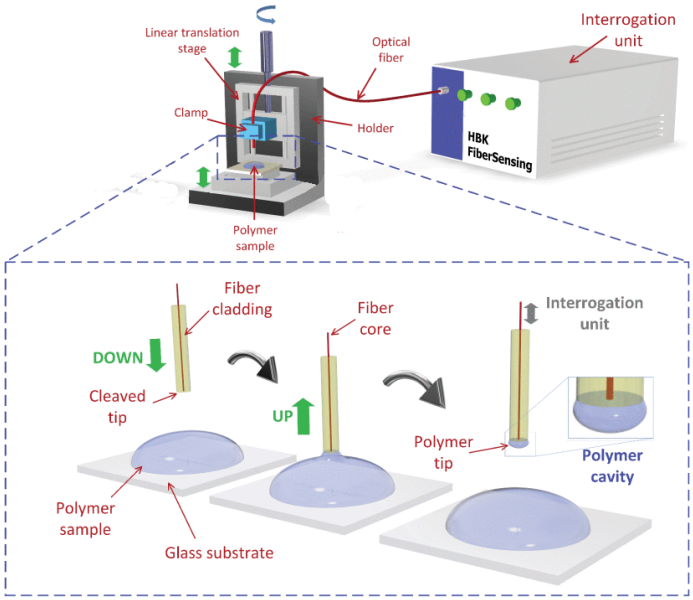

FIGURE 4.12: Experimental setup for the fabrication of the FP tips (edited from [119]).

Since the light source has a spectrally dependent intensity $I_{src}(\lambda)$, a correction of the measured spectra is needed to compensate this effect. If $I_{FP}(\lambda)$ is the measured spectra and $I_{core}(\lambda)$ the spectrum of the cleaved fiber in the air, obtained before deposition, $I_R(\lambda)$ can be obtained without knowing $I_{src}(\lambda)$ using:

$$\frac{I_{FP}(\lambda)}{I_{core}(\lambda)} = \frac{I_{src}(\lambda)I_R(\lambda)}{I_{src}(\lambda)R_{core}(\lambda)} \tag{4.4}$$

The average value of the signal and its amplitude can then be introduced in equation 4.3 to solve it for n_{pol}, resulting in 4 possible values for the RI and in the coating thickness [119].

Since a high number of bilayers was deposited and for the early layers deposition there is an exponential growth of the overlay [117, 118], this technique cannot be used to obtain the thickness of the coating with only two bilayers but can provide relevant information about the expansion/compression behavior of the polymer with the pH.

4.5 Fabrication and Characterization of an Aptamer-Based SPR Sensor for the Detection of Glyphosate

4.5.1 Chemical Reagents and Solutions

The following reagents and solutions were used for the assembly of the sensing probe: 0.1% (w/v) poly-L-lysine (PLL) solution in H_2O was purchased from Sigma-Aldrich; and amine-modified glyphosate binding aptamers (GBA) with a sequence (NH2 - 5'-GGA CAG CTG GCC GCG TAG CGA GAC ACG TAC AAG GTA CTA TAC GGC TGG CAT ATG TAT CTG-3'; Mw 18.7 kDa) were purchased from Eurogentec S.A. and were prepared in a 10x SSPE buffer solution to a final concentration of 0.57 µM. Glyphosate (PESTANAL®, analytical standard) was purchased from Sigma-Aldrich and was prepared in DI water to a final concentration of 500mg/L, being stored as a stock solution for further dilutions in smaller concentrations.

4.5.2 Sensing Probe Assembly and Glyphosate Detection

The glyphosate sensing probe was assembled on a planar substrate with a 50nm gold film and a 3nm chromium adhesion layer. Both the assembly and the glyphosate detection were performed on the excitation setup with the microfluidic chamber described in section 4.3, so the SPR bands could be constantly tracked during this process.

To assemble the sensing probe, the sensing surface was first rinsed with DI water and then functionalized with PLL for 30 minutes, at room temperature. Since PLL is a strong polycation, an electrostatic attraction to gold is possible. The prepared GBA solution was then incubated for 60 minutes at room temperature, to enable covalent attachment to the

PLL. This structure, presented in figure 4.13, can be then used to detect glyphosate, by monitoring the GBA/Glyphosate complex formation.

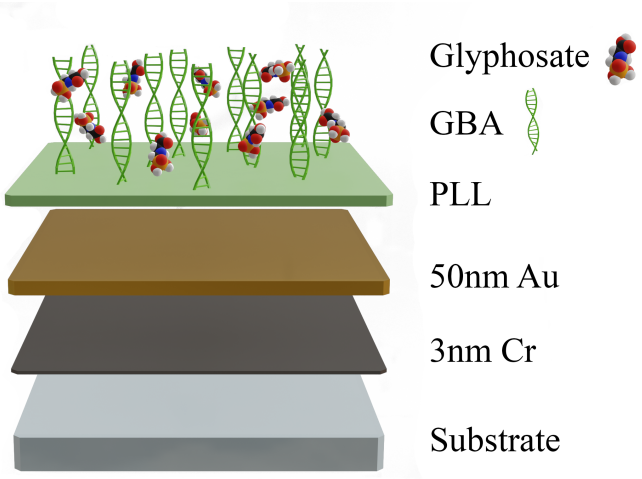

Figure 4.13: Schematic of the fabricated aptamer-based SPR sensor for the detection of glyphosate.

To measure the response of the sensing structure to glyphosate, it was incubated with several concentrations of glyphosate ranging from 10^{-3} to 10^{5}µg/L, for 30 minutes. Between all concentrations steps, the device was washed with DI water. The positions of the bands in water after the rinsing process are the only ones relevant for studying the sensor, as they indicate whether the GBA and glyphosate are bound.

Chapter 5

Experimental Results and Discussion

In this chapter, the experimental results obtained for the fabricated optical pH sensors and Aptamer-Based SPR Sensor for the Detection of Glyphosate are presented. In section 5.1 the pH sensitive polymeric coating structural response and stability was also discussed, and in section 5.2 the limit of detection of the glyphosate sensor was obtained and compared to the regulated values.

5.1 Optical pH Sensor based on a Polymeric Nanocoating

5.1.1 FP cavity on a Fiber Tip

The spectra obtained for the PEI/PAA coating on a fiber tip, at different pH values, is represented in figure 4. It was only possible to observe a FP cavity response when the structure was either dry or at high and low pH values, likely because it was in a saturated state, where changes in volume with time were negligible.

Using only the results from equation 4.3 it was not possible to obtain a value for the RI of the polymeric coating, but the difference in the spectra period is large enough to conclude about the volume changes with pH. When it is dry, the polymers are in their collapsed state of minimum thickness, and while immersed in a solution, a decrease of the pH results in a compression of the coating, increasing its RI. This is an essential result to understand the polymeric coating response.

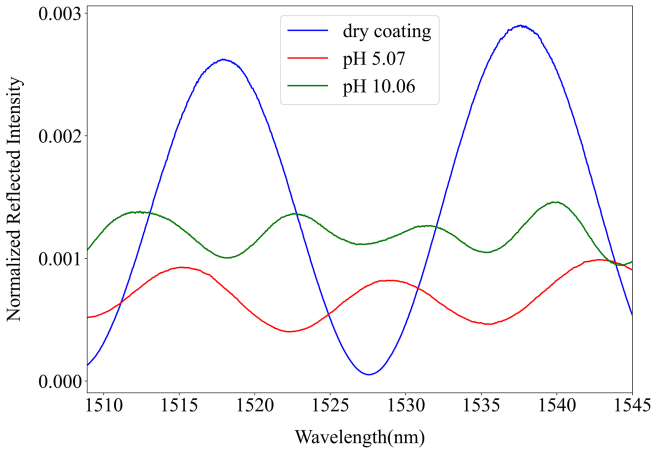

Figure 5.1: Normalized reflected intensity of a FP cavity in a fiber tip coated with 21 PEI/PAA bilayers.

5.1.2 Bare LPFG

The resonance band was monitored during the LbL deposition process on a bare LPFG. Figure 5.2 shows the spectra corresponding to each bilayer, when the LPFG was immersed in the sodium acetate rinsing solution. It is evident from the spectra that with each bilayer the bands widen and undergo a blue shift. This corresponds to an increase in the effective RI of the cladding, which is aligned with our expectations, since the deposited polymers possess a higher RI than the buffer. The band translation can then be used to confirm the deposition of the overlay.

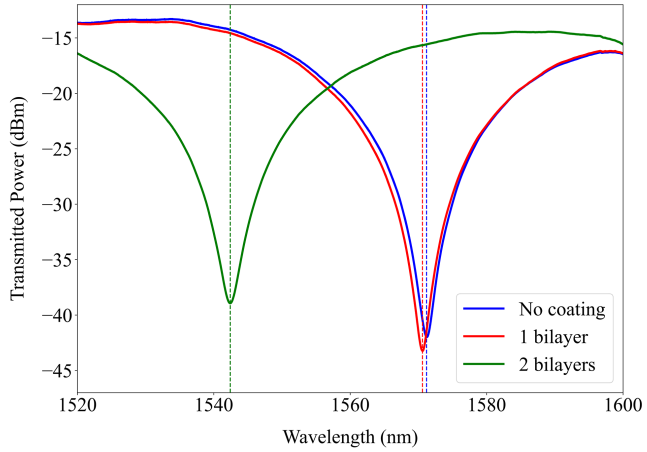

Figure 5.2: Long-period fiber grating resonance band shift with PEI/PAA bilayers deposition.

The coated LPFG spectral response to an increase of the immersion solution pH is presented in figure 5.3, where a redshift of the band is observed, verifying the pH sensitivity of the fabricated structure. With an increase of the external RI or with higher coating thicknesses, a typical LPFG band intensity tends to attenuate, a monotone behavior that was not observed in the fabricated sensor response to pH. In this case, two regions can be observed, one where the resonance band power peak decreases with the pH and another where it increases. From this result, we can assume that both the variation of the coating thickness and its RI, properties that depend on each other, influence the sensor response, and neither of those changes can be ignored in the analysis. Since a blueshift with an increase of the pH was recorded, we conclude that the shift due to the coating RI decrease dominates over the higher thickness.

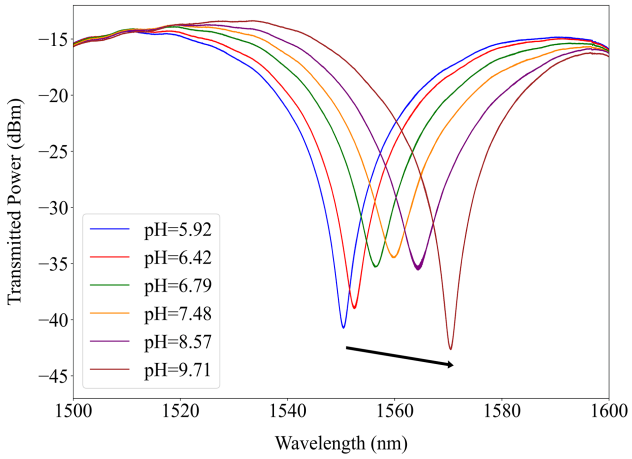

Figure 5.3: Coated Long-period fiber grating resonance band shift with a pH increase along the arrow.

The dynamic response of the sensor in the 5.00-10.18 pH range was obtained simultaneously to the response curve, and is presented in figure 5.4, where the time response to successive pH variations can be observed. A significant sensitivity to pH was attained in the region from pH 5.92 to 9.23. Outside this range, the sensor exhibited minor wavelength shifts, leading to an absence of any discernible pH response. This means that the polymeric structure is saturated, either in its most compressed or expanded stated.

Figure 5.4 also highlights the sensor behavior when a pH variation is introduced. The resonance peak position takes around 8 minutes to stabilize, which is a sensor parameter that must be improved to obtain a practical, high-resolution device. It can be improved by increasing the surface roughness, therefore foregoing a high sensitivity, so a compromise

has to be found between the response time and the sensitivity. An easy change to the fabrication method that affects the surface roughness is the variation of the dipping solution's pH or the addition of a dye to the solution [30].

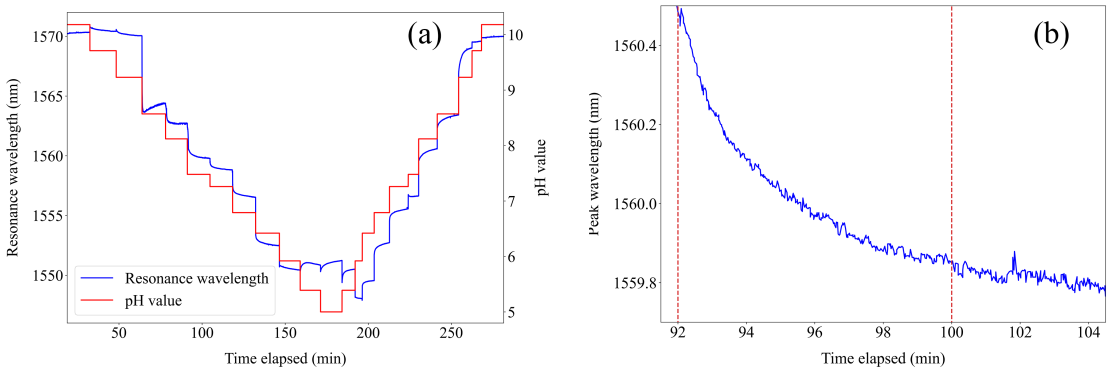

Figure 5.4: (a) Measured dynamic response of the sensor and (b) zoomed in section to highlight the response time.

The calibration curve of the sensor in the 5.92-9.23 pH range is shown in figure 5.5, where the sensitivity to this parameter is also registered. When the pH is outside this region, while certain external factors might cause a slight band shift, it is negligible. As such, we assume the coating remains in the same state as in the limit of the defined region. The fabricated sensor achieved a substantial wavelength shift of 19.6 nm due to a pH variation of 3.3, while the reference LPFG shifts were negligible. This was obtained in a structure with only two bilayers, whose fabrication was simple and fast, despite the critical step of altering the pH of the PAA dipping solution. The low number of bilayers can also be a disadvantage to the reproducibility of this structure, as environmental factors can affect the solutions pH and the LbL deposition process, therefore having great influence on the overlay thickness and its response curve. The control over the coating thickness is lower when only a few thicker layers are deposited.

The reversibility of the sensor is also demonstrated, with a 20% hysteresis that cannot be ignored. This behavior is a typical occurrence in pH sensitive polymers due to differences in the deswelling and swelling phenomena that create non-linear effects. Not only the shrunk and swollen states of the structure have different energy barrier heights depending on the transition direction, but the diffusion process of protons when the coating is placed in a new environment also varies with the polymer expansion state, resulting in the observed hysteresis and in a difference in the response curves when increasing and decreasing the pH [138].

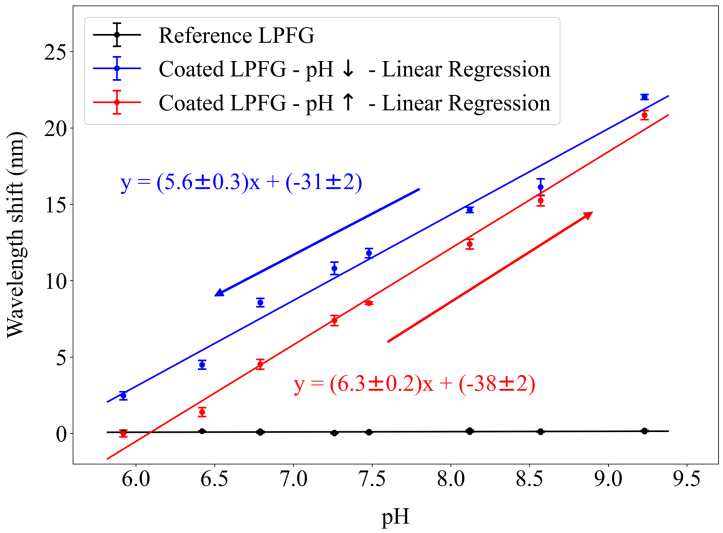

Figure 5.5: Coated long-period fiber grating response curve to an increase and to a decrease of pH values.

A linear response of the sensor was observed, so a linear fit of experimental data can be done. A sensitivity of (5.6±0.3)nm/pH when decreasing the pH and (6.3±0.2)nm/pH when increasing it was achieved. Higher pH sensitivities could still be obtained by adding additional layers, with the consequence of a wider band.

For an optical sensor to be practical, reusability and repeatability are essential features. Figure 5.6 shows the response of the sensor to multiple cycles between buffers of pH 5.59 and 7.36. While a slight degradation of the response was observed, it was negligible considering the overall shift, which is a great result for a possible implementation in long-term measurements.

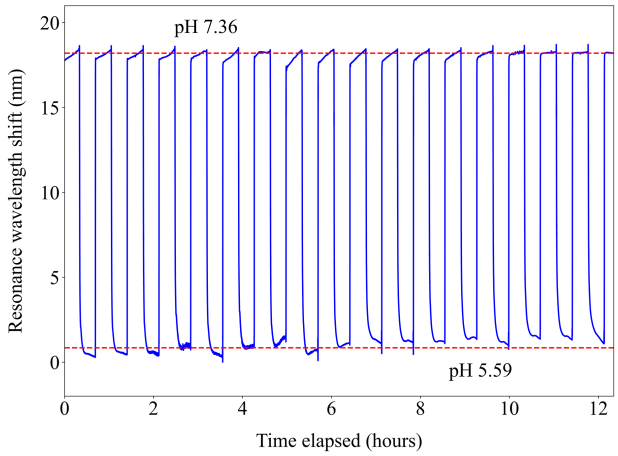

Figure 5.6: Stability test of the sensor to multiple cycles between pH 5.59 and 7.36.

The slight variation might be due to the large change of pH in the cycles, that can change the number of ionizable groups in the polymers, therefore shifting the response, or due to the formation of salts, altering the ionic strength [138]. A stability test of another LPFG with a similar coating was done for a longer period, and the obtained timeline is represented in figure 5.7. In this case, the change of ionizable groups becomes evident as a drift of the response is observed, completely altering the response and sensitivity of the structure. This phenomenon cannot be prevented, so the best application of pH sensitive polymeric coatings is then the real-time monitoring in scenarios where only gradual changes of this parameter are expected.

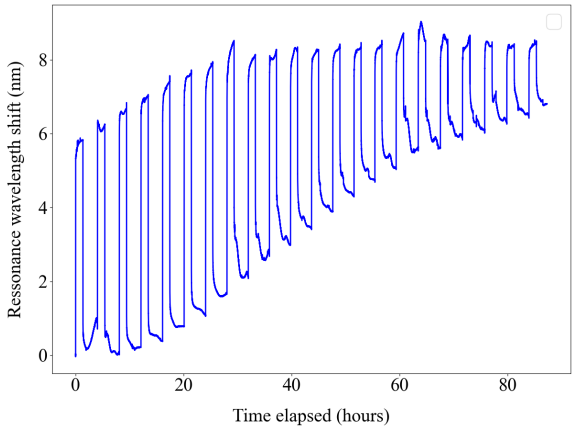

Figure 5.7: Stability test of the sensor to multiple cycles between pH 6.06 and 7.34, where a drift of the response was observed.

When the pH value of a multilayer coating changes, there is a competition between multiple factors, such as the electrostatic interaction of a polymer chains with themselves or the other polymer chains, and the molecule's water affinity, resulting in multiple response phases [139]. Since the PEI/PAA coating reduces its thickness with a pH decrease, one can assume that PAA responsible for most of the structural changes with this parameter, since at low pH its acidic groups are protonated and unionized, the hydrophobic interactions dominate resulting in a lower thickness, and at a higher pH the opposite occurs, it has a high charge density which increases the electrostatic repulsion between the polymer chains, that will then associate with water to cause swelling [140].

Crossing the results from the LPFG sensor and the FP cavity on the fiber tip, a wavelength shift of around 20nm when the coating thickness expands about 155% is expected. Knowing this information and having the possible RI solutions from the FP interferometer, simulations of the response were performed using the numerical implementation described in section 3.1, and a trend similar to the observed experimentally was achieved when the

coating expanded from 200nm and 1.530 RI, at a low pH, to 310nm with a 1.353 RI. The simulated curve is represented in Figure 10.

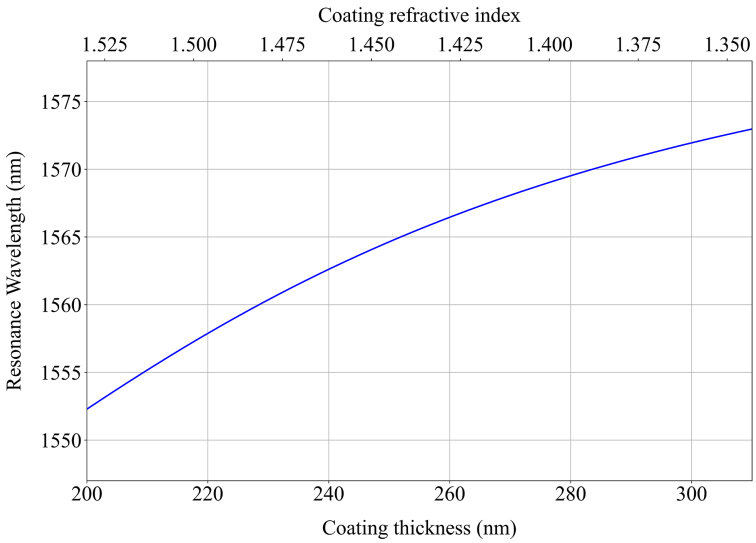

Figure 5.8: Simulated response of the LP_{16} mode of an LPFG with a variation of its coating thickness and RI (1.333 external RI).

From the FP fiber tip data, we then obtain that at a pH of 5.07 (the coating is saturated and compressed) the overlay has a RI of 1.53±0.01, which expands by (56.6±0.6)% at a pH of 10.06, when its RI is 1.35±0.01.

5.1.3 TiO_2 coated LPFG

As an attempt to obtain a more sensitive pH sensor using LPFGs, the same polymeric structure was deposited on an LPFG previously coated with 40nm of TiO_2. The high RI of the metal oxide increases the effective RI of the cladding to values where the phase-matching curve slope is higher, making the structure more sensitive in the 1.30 to 1.40 external RI range [23].

The resonance bands obtained when this structure was immersed in solution with different pH are represented in figure 5.9. Unlike a bare LPFG, the band's width increases significantly with the pH decrease. For pH values below 7.48 the deformation is already pronounced, and for a 6.22 pH the band has collapsed. This behavior is due to the higher effective refractive index obtained when combining the dielectric and the polymeric coating in acidic solutions, that as previously predicted achieved a 1.530 RI for low pH values.

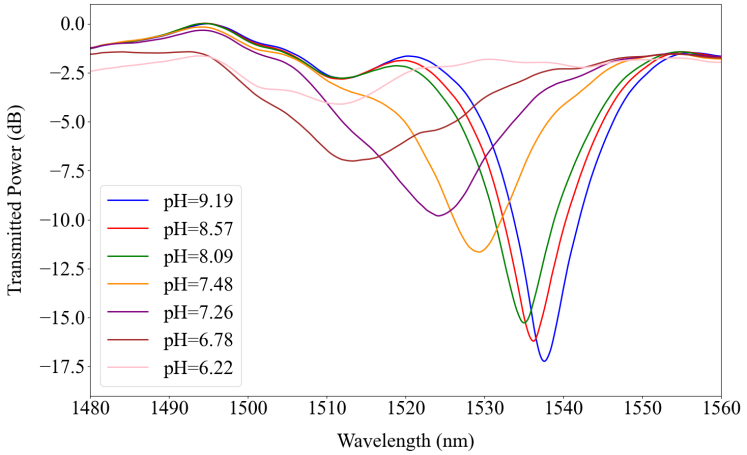

Figure 5.9: Polymer and TiO_2 coated LPFG resonance band shift with pH variations.

Despite the large band width and consequently low resolution, it was still possible to obtain the resonance peaks for pH values above 6.78, by applying a low-pass filter. In the 6.78-8.09 pH range, a linear response was observed, with a sensitivity of (16±2)nm/pH when decreasing the pH and (16±1)nm/pH when increasing it. This sensitivity is almost three times higher than the obtained using a bare LPFG, but the low resolution and small detection range of this structure set aside the interest in this sensor. Nevertheless, it might find applications for sensing of alkaline solutions.

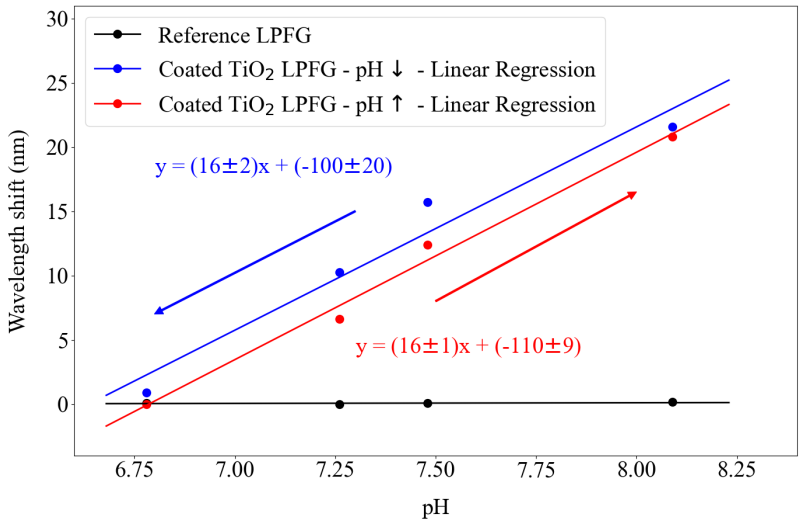

Figure 5.10: Response curve of a Polymer and TiO_2 coated LPFG to an increase and to a decrease of pH values.

5.1.4 SPR in a Planar Substrate

SPR sensing structures have completely different properties than LPFGs. Using spectral interrogation, the SPR bands are significantly larger, but the higher sensitivity of SPPs to

the external RI enables higher resolution measurements when using plasmonic sensors. As such, the implementation of the PEI/PAA coating in a SPR pH structure in a planar substrate was attempted.

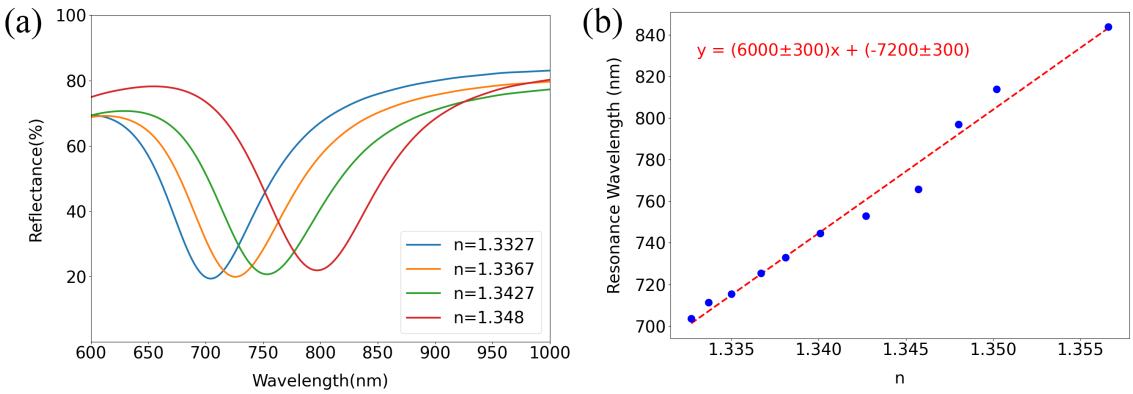

Figure 5.11: (a) Experimental SPR bands of a 50nm Au film at different RIs and (b) its sensitivity curve.

The plasmonic structure chosen was a 50nm gold film, with a 3nm chromium adhesion layer, as long-time exposure to solutions is almost a requirement for current pH sensors and gold has great chemical stability. It had a sensitivity of (6000±300)nm/RIU, as presented in figure 5.11, where the resonance wavelengths were measured using solutions with different RI. They were fabricated by dissolving sucrose in DI water in different ratios, and their RI was measured using an Abbe refractometer (Atago DR-A1).

In an initial approach, the dipping solutions used for the coating fabrication had the same pH and concentration as the ones used in the LPFGs, but the thickness of the obtained coating was too high, considering the high sensitivity and low field penetration of the SPP, and consequently the SPR band disappeared after the LbL deposition. Since the number of fabricated layers was already low, the pH of the PAA was increase and the concentration of the solution decreased as an attempt to find values that would result in a film with an adequate thickness for SPR sensing.

An interesting structure was found when using a 0.2% PAA solution with pH 6.2 and a 0.1% PEI solution with 10.5 pH, which caused a band shift of 87nm, as seen in figure 5.12.

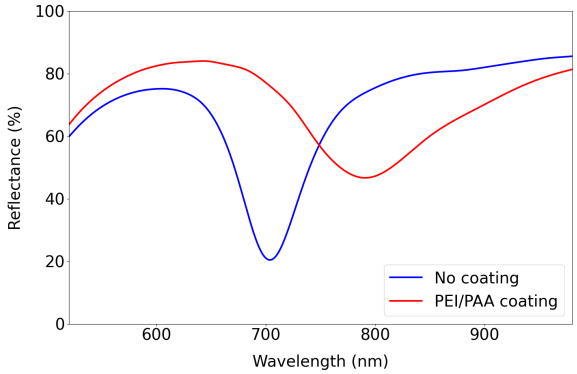

Figure 5.12: Shift of the SPR band after deposition of the polymeric coating.

The response of the sensing structure SPR bands to pH variations is shown in figure 5.13. Unlike what was observed in the LPFG, due to the reduced thickness of the coating and possible differences in the adhesion of PAA onto gold instead of silica, neither the wavelength shifts due to the thickness changes or the shift caused by RI variation of the coating when altering the pH dominated over the other. Instead, what was observed were random shifts of the bands and a decrease in the reflected power for higher pH solution, mainly caused by higher optical losses of the compressed polymeric coating.

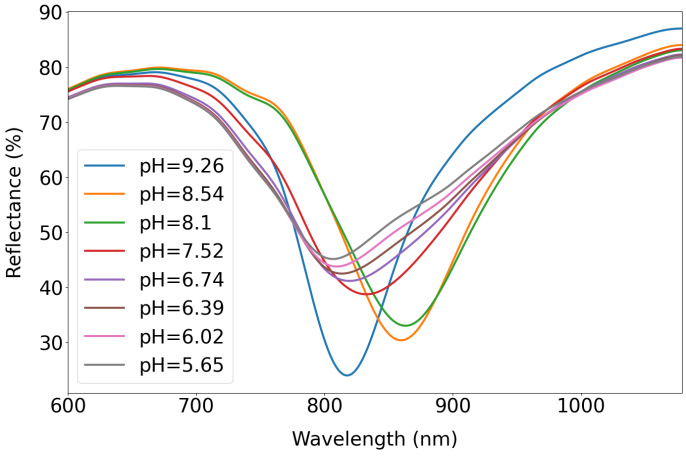

Figure 5.13: SPR bands of the PEI/PAA coated Au film for different pH values.

Integrating the bands, we can obtain a value proportional to the reflected power. In the 5.65-7.52 pH range, a linear relation between the reflected power and the pH was obtained, with a sensitivity of (18$\pm$1)/pH when decreasing the pH and (16.9$\pm$0.5)/pH when increasing it, as seen in figure 5.14. While the high sensitivity desired by using the SPR and spectral interrogation was not achieved, the power results enable an interesting approach using intensity interrogation, as well as a simpler and cheaper setup by swapping the spectrometer for a photodetector.

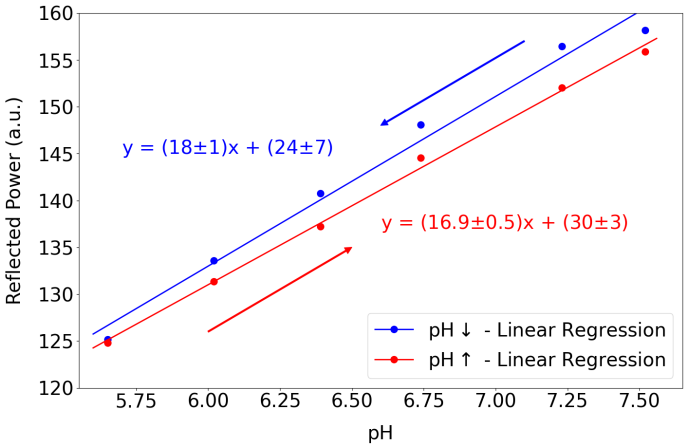

Figure 5.14: Reflected power of the SPR band as a function of the solution pH.

5.2 Aptamer-Based SPR Sensor for the Detection of Glyphosate

Before the assembly of the sensing probe, the sensitivity of the plasmonic structure was obtained, using solutions of different RI prepared by mixing DI water and ethanol, to not leave any residue on the gold surface. A sensitivity of (4800±200)nm/RIU was measured, as seen in figure 5.15.

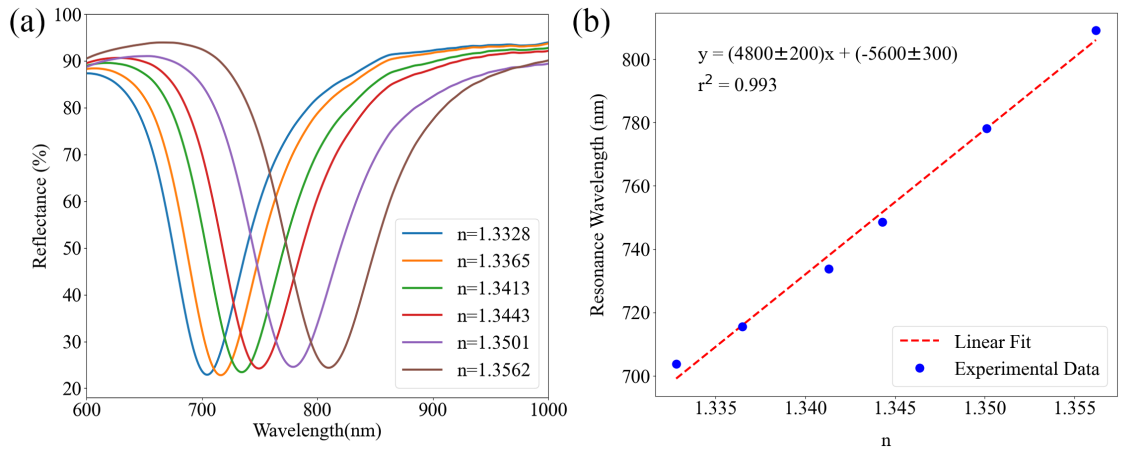

Figure 5.15: (a) Experimental SPR bands of the planar sensing structure of 50nm Au at different RIs and (b) its sensitivity curve.

Figure 5.16 shows the shift of the SPR band when the PLL and GBA were deposited on the sensing structure. A significant shift was observed after each deposition step, for a total wavelength shift of 7.1nm, which confirms the deposition of the structures and therefore sensing probe fabrication.

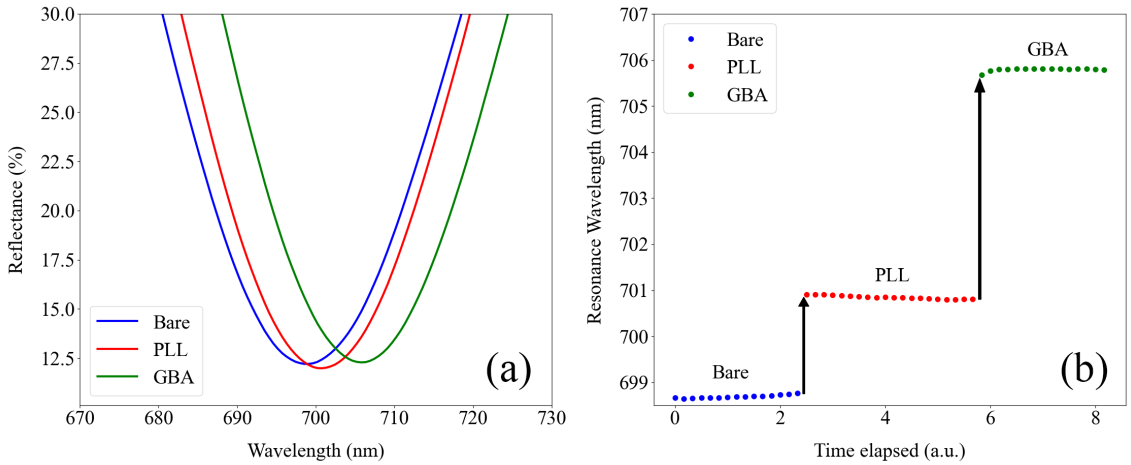

Figure 5.16: (a) SPR bands after each procedure of the the sensing probe deposition and (b) wavelength shift of the structure.

For each glyphosate concentration, wavelength shifts in the order of hundreds of picometers were observed, whose detection with high precision was only possible due to the narrow SPR bands obtained when using a planar configuration. The results can be observed in figure 5.17, confirming the detection of this contaminant.

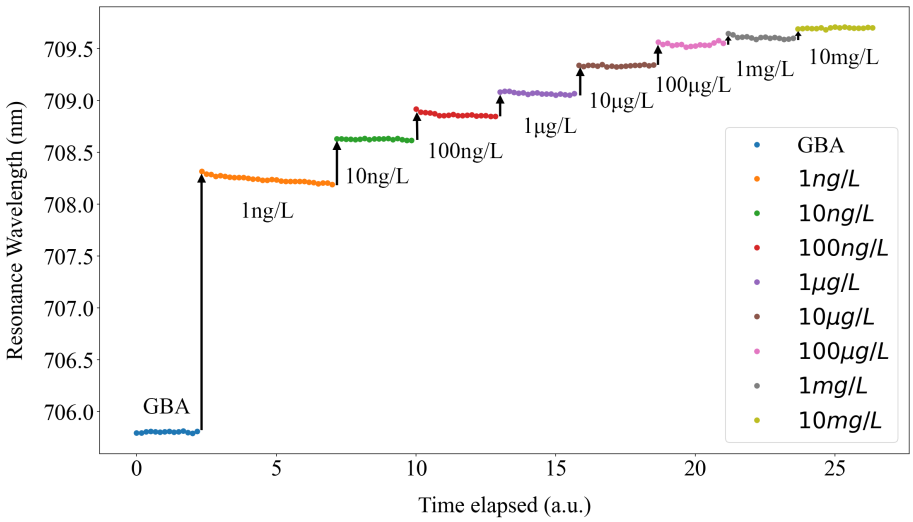

Figure 5.17: Resonance wavelength of the sensor in water, after each incubation in different concentrations of glyphosate

The resonance wavelength can be plotted as a function of the glyphosate concentration to obtain the response curve of the sensor to this molecule. In order to calculate the limit of detection (LOD) of the sensor, that data was fitted to the Hill-Langmuir equation [141], traditionally used to characterize molecule binding processes:

$$y = \lambda_{min} + (\lambda_{max} - \lambda_{min}) \frac{x^{nH}}{k^{nH} + x^{nH}} \tag{5.1}$$

x is stimuli dose, in this case the glyphosate concentration, y the sensor response and λ_{max} and λ_{min} the maximum and minimum wavelengths achievable, respectively. k is the effective ligand concentration producing half occupation of the binding sites and nH is the Hill coefficient, that quantifies the degree of interaction between ligand binding sites and compensates this effect in the calculations.

Fixing λ_{min} as the resonance wavelength measured before glyphosate incubation, 705.80nm, the fitted equation, represented in figure 5.18, has and r^2 of 0.9993 and the following fitting parameters: λ_{max} = (709.98nm ± 0.09), k = (9 ± 2) × 10^{-5}µg/L and nH = (0.15 ± 0.01).

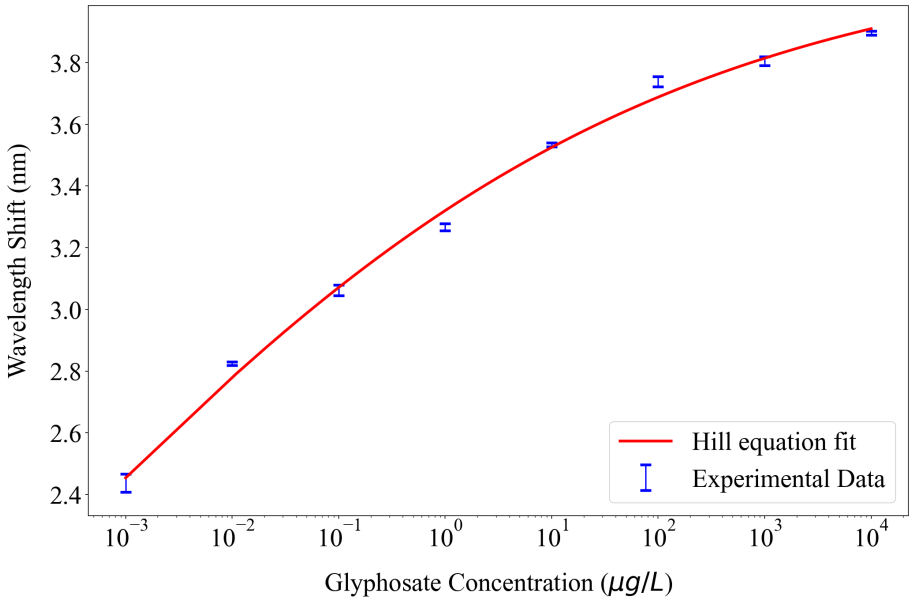

Figure 5.18: SPR wavelength as a function of the concentration of glyphosate

If the sensitivity of the structure is defined as the quotient between the total wavelength shift and the half-maximum effective concentration:

$$S = \frac{\lambda_{max} - \lambda_{min}}{k^{nH}} \tag{5.2}$$

, the sensitivity of the fabricated sensor is (16.7 ± 0.5)nm/(µg/L). This value can then be used to calculate the limit of detection of the sensor:

$$\text{LOD} = \frac{3\sigma}{S} \tag{5.3}$$

Defining σ as the standard deviation of the measurements in water before the sensing probe assembly, 6pm for the used setup, the LOD of the sensor is $(1.13 \pm 0.03) \times 10^{-3}$µg/L. This value is 2 orders of magnitude lower than the defined safety limit of 0.1µg/L, making this sensor viable for glyphosate detection, and confirming aptamer-based SPR sensors as a promising approach for the detection of this contaminant.

Chapter 6

Final Remarks and Future Work

The theoretical study of the physical principles behind LPFGs was proven essential for the development of a pH sensor using these gratings as sensing platforms. Moreover, the simulation software developed using a numerical implementation of the TMM formalism and the coupling coefficients formulation was used to corroborate experimental results and to understand the behavior of a pH sensitive coating to variations of this parameter. The Python code implementation allows the simulation of an LPFG with an arbitrary structure, including deposited overlays. As such, the development of a graphical user interface to facilitate the use of this software will surely be useful, but the code still needs to be optimized or written in a faster language before creating the interface.

In this work, only a small fraction of the plasmonic topics were studied and implemented experimentally. It is an emerging field, still being developed, and whose complexity is rapidly increasing. Nevertheless, the foundations established through the simulation of SPR, fabrication of thin film and experimental excitation of SPPs will allow future research in this area.

A highly sensitive optical pH sensor based on a PEI/PAA polymeric coating deposited onto an LPFG was achieved and thoroughly studied. However, since the overlay fabrication was done using the LbL technique, a chemical process, it can still be further optimized by tweaking various parameters, from the dipping solutions pH and concentration to the immersion times and external conditions, a trial-and-error process that ideally would result in a lower hysteresis and higher pH sensing range. Using the same polymers and deposition technique, a SPR pH sensor was also attained, but contrary to the typical spectral interrogation approach, only the reflected power had a significant linear shift with the pH. Additional testing of this structure could provide interesting results.

The applicability of SPR structures in a planar substrate for the detection of glyphosate was attested by achieving a lower LOD than the safety limit defined by most environmental control agencies. However, it was not tested in the presence of interferents, which must be done before any implementation in a real scenario. Future work would be the introduction of the sensing probe on SPR structures in fiber optics, that might be able to achieve better results due to a bigger sensing region. The measurement of this contaminant using optical fibers would also allow for multiplexing applications, for example with the developed pH sensor, that are a high priority to accommodate the current needs in water quality monitoring.

Bibliography

[1] E. Swyngedouw, “Un water report 2012: Depoliticizing water,” *Development and Change*, vol. 44, no. 3, pp. 823–835, 2013. [Online]. Available: https://onlinelibrary.wiley.com/doi/abs/10.1111/dech.12033

[2] X. Su, L. Sutarlie, and X. J. Loh, “Sensors, biosensors, and analytical technologies for aquaculture water quality,” *Research*, vol. 2020, 2020. [Online]. Available: https://spj.science.org/doi/abs/10.34133/2020/8272705

[3] S. N. Zulkifli, H. A. Rahim, and W.-J. Lau, “Detection of contaminants in water supply: A review on state-of-the-art monitoring technologies and their applications,” *Sensors and Actuators B: Chemical*, vol. 255, pp. 2657–2689, 2018. [Online]. Available: https://www.sciencedirect.com/science/article/pii/S0925400517317446

[4] S. Yin, P. Ruffin, and F. Yu, *Fiber Optic Sensors*, ser. Optical Science and Engineering. CRC Press, 2017. [Online]. Available: https://books.google.pt/books?id=5KdCOguH9CsC

[5] A. Kersey, M. Davis, H. Patrick, M. LeBlanc, K. Koo, C. Askins, M. Putnam, and E. Friebele, “Fiber grating sensors,” *Journal of Lightwave Technology*, vol. 15, no. 8, pp. 1442–1463, 1997.

[6] S. W. James and R. P. Tatam, “Optical fibre long-period grating sensors: characteristics and application,” *Measurement Science and Technology*, vol. 14, no. 5, p. R49, mar 2003. [Online]. Available: https://dx.doi.org/10.1088/0957-0233/14/5/201

[7] K. O. Hill, Y. Fujii, D. C. Johnson, and B. S. Kawasaki, “Photosensitivity in optical fiber waveguides: Application to reflection filter fabrication,” *Applied Physics Letters*, vol. 32, no. 10, pp. 647–649, 08 2008. [Online]. Available: https://doi.org/10.1063/1.89881

[8] F. Chiavaioli, F. Baldini, S. Tombelli, C. Trono, and A. Giannetti, "Biosensing with optical fiber gratings," *Nanophotonics*, vol. 6, no. 4, pp. 663–679, 2017. [Online]. Available: https://doi.org/10.1515/nanoph-2016-0178

[9] A. Vengsarkar, P. Lemaire, J. Judkins, V. Bhatia, T. Erdogan, and J. Sipe, "Long-period fiber gratings as band-rejection filters," *Journal of Lightwave Technology*, vol. 14, no. 1, pp. 58–65, 1996.

[10] V. Bhatia and A. M. Vengsarkar, "Optical fiber long-period grating sensors," *Opt. Lett.*, vol. 21, no. 9, pp. 692–694, May 1996. [Online]. Available: https://opg.optica.org/ol/abstract.cfm?URI=ol-21-9-692

[11] V. Bhatia, T. D'Alberto, K. A. Murphy, R. O. Claus, and C. P. Nemarich, "Comparison of optical fiber long-period and Bragg grating sensors," in *Smart Structures and Materials 1996: Smart Sensing, Processing, and Instrumentation*, K. A. Murphy and D. R. Huston, Eds., vol. 2718, International Society for Optics and Photonics. SPIE, 1996, pp. 110 – 121. [Online]. Available: https://doi.org/10.1117/12.240853

[12] T. Erdogan, "Cladding-mode resonances in short- and long-period fiber grating filters," *J. Opt. Soc. Am. A*, vol. 14, no. 8, pp. 1760–1773, Aug 1997. [Online]. Available: https://opg.optica.org/josaa/abstract.cfm?URI=josaa-14-8-1760

[13] E. Anemogiannis, E. Glytsis, and T. Gaylord, "Transmission characteristics of long-period fiber gratings having arbitrary azimuthal/radial refractive index variations," *Journal of Lightwave Technology*, vol. 21, no. 1, pp. 218–227, 2003.

[14] I. D. Villar, I. R. Matías, F. J. Arregui, and P. Lalanne, "Optimization of sensitivity in long period fiber gratings with overlay deposition," *Opt. Express*, vol. 13, no. 1, pp. 56–69, Jan 2005. [Online]. Available: https://opg.optica.org/oe/abstract.cfm?URI=oe-13-1-56

[15] O. Deparis, R. Kiyan, O. Pottiez, M. Blondel, I. G. Korolev, S. A. Vasiliev, and E. M. Dianov, "Bandpass filters based on π-shifted long-period fiber gratings for actively mode-locked erbium fiber lasers," *Opt. Lett.*, vol. 26, no. 16, pp. 1239–1241, Aug 2001. [Online]. Available: https://opg.optica.org/ol/abstract.cfm?URI=ol-26-16-1239

[16] M. Harumoto, M. Shigehara, and H. Suganuma, “Gain-flattening filter using long-periodfiber gratings,” *J. Lightwave Technol.*, vol. 20, no. 6, p. 1027, Jun 2002. [Online]. Available: https://opg.optica.org/jlt/abstract.cfm?URI=jlt-20-6-1027

[17] V. Grubsky, D. S. Starodubov, and J. Feinberg, “Wavelength-selective coupler and add-drop multiplexer using long-period fiber gratings,” in *Optical Fiber Communication Conference*. Optica Publishing Group, 2000, p. FB5. [Online]. Available: https://opg.optica.org/abstract.cfm?URI=OFC-2000-FB5

[18] V. Bhatia, D. Campbell, R. O. Claus, and A. M. Vengsarkar, “Simultaneous strain and temperature measurement with long-period gratings,” *Opt. Lett.*, vol. 22, no. 9, pp. 648–650, May 1997. [Online]. Available: https://opg.optica.org/ol/abstract.cfm?URI=ol-22-9-648

[19] J. Qu, H. Zhang, X. Shi, C. Li, D. Jia, T. Liu, and R. Su, “High sensitivity temperature sensing of long-period fiber grating for the ocean,” *Sensors*, vol. 23, no. 10, 2023. [Online]. Available: https://www.mdpi.com/1424-8220/23/10/4768

[20] Y.-P. Wang, D. N. Wang, and W. Jin, “Co2 laser-grooved long period fiber grating temperature sensor system based on intensity modulation,” *Appl. Opt.*, vol. 45, no. 31, pp. 7966–7970, Nov 2006. [Online]. Available: https://opg.optica.org/ao/abstract.cfm?URI=ao-45-31-7966

[21] H. Patrick, C. Chang, and S. Vohra, “Long period fibre gratings for structural bend sensing,” *Electronics Letters*, vol. 34, pp. 1773–1775(2), September 1998. [Online]. Available: https://digital-library.theiet.org/content/journals/10.1049/el_19981237

[22] G. M. Rego, J. L. Santos, and H. M. Salgado, “Refractive index measurement with long-period gratings arc-induced in pure-silica-core fibres,” *Optics Communications*, vol. 259, no. 2, pp. 598–602, 2006. [Online]. Available: https://www.sciencedirect.com/science/article/pii/S0030401805009703

[23] L. Coelho, D. Viegas, J. Santos, and J. Almeida, “Enhanced refractive index sensing characteristics of optical fibre long period grating coated with titanium dioxide thin films,” *Sensors and Actuators B: Chemical*, vol. 202, pp. 929–934, 2014. [Online]. Available: https://www.sciencedirect.com/science/article/pii/S0925400514007242

[24] Q. Ling, Z. Gu, and K. Gao, "Smart design of a long-period fiber grating refractive index sensor based on dual-peak resonance near the phase-matching turning point," *Appl. Opt.*, vol. 57, no. 10, pp. 2693–2697, Apr 2018. [Online]. Available: https://opg.optica.org/ao/abstract.cfm?URI=ao-57-10-2693

[25] F. Chiavaioli, P. Biswas, C. Trono, S. Jana, S. Bandyopadhyay, N. Basumallick, A. Giannetti, S. Tombelli, S. Bera, A. Mallick, and F. Baldini, "Sol–gel-based titania–silica thin film overlay for long period fiber grating-based biosensors," *Analytical Chemistry*, vol. 87, no. 24, pp. 12 024–12 031, 2015, pMID: 26548589. [Online]. Available: https://doi.org/10.1021/acs.analchem.5b01841

[26] A. A. Badmos, Q. Sun, Z. Sun, J. Zhang, Z. Yan, P. Lutsyk, A. Rozhin, and L. Zhang, "Enzyme-functionalized thin-cladding long-period fiber grating in transition mode at dispersion turning point for sugar-level and glucose detection," *Journal of Biomedical Optics*, vol. 22, no. 2, p. 027003, 2017. [Online]. Available: https://doi.org/10.1117/1.JBO.22.2.027003

[27] A. Baliyan, S. Sital, U. Tiwari, R. Gupta, and E. K. Sharma, "Long period fiber grating based sensor for the detection of triacylglycerides," *Biosensors and Bioelectronics*, vol. 79, pp. 693–700, 2016. [Online]. Available: https://www.sciencedirect.com/science/article/pii/S0956566315307417

[28] K. Dandapat, S. M. Tripathi, Y. Chinifooroshan, W. J. Bock, and P. Mikulic, "Compact and cost-effective temperature-insensitive bio-sensor based on long-period fiber gratings for accurate detection of e. coli bacteria in water," *Opt. Lett.*, vol. 41, no. 18, pp. 4198–4201, Sep 2016. [Online]. Available: https://opg.optica.org/ol/abstract.cfm?URI=ol-41-18-4198

[29] M. Janczuk-Richter, M. Dominik, E. Roźniecka, M. Koba, P. Mikulic, W. J. Bock, M. Łoś, M. Śmietana, and J. Niedziółka□Jönsson, "Long-period fiber grating sensor for detection of viruses," *Sensors and Actuators B: Chemical*, vol. 250, pp. 32–38, 2017. [Online]. Available: https://www.sciencedirect.com/science/article/pii/S092540051730758X

[30] J. M. Corres, I. R. Matias, I. del Villar, and F. J. Arregui, "Design of ph sensors in long-period fiber gratings using polymeric nanocoatings," *IEEE Sensors Journal*, vol. 7, no. 3, pp. 455–463, 2007.

[31] Y. Chen, F. Tang, Y. Tang, M. J. O'Keefe, and G. Chen, "Mechanism and sensitivity of fe-c coated long period fiber grating sensors for steel corrosion monitoring of rc structures," *Corrosion Science*, vol. 127, pp. 70–81, 2017. [Online]. Available: https://www.sciencedirect.com/science/article/pii/S0010938X17306935

[32] T. Wang, S. Korposh, S. James, R. Tatam, and S.-W. Lee, "Optical fiber long period grating sensor with a polyelectrolyte alternate thin film for gas sensing of amine odors," *Sensors and Actuators B: Chemical*, vol. 185, pp. 117–124, 2013. [Online]. Available: https://www.sciencedirect.com/science/article/pii/S0925400513004668

[33] M. Partridge, S. W. James, and R. P. Tatam, "Dissolved oxygen sensing using an optical fiber long period grating coated with hemoglobin," *Journal of Lightwave Technology*, vol. 34, no. 19, pp. 4506–4510, 2016.

[34] J. Hromadka, S. Korposh, M. C. Partridge, S. W. James, F. Davis, D. Crump, and R. P. Tatam, "Multi-parameter measurements using optical fibre long period gratings for indoor air quality monitoring," *Sensors and Actuators B: Chemical*, vol. 244, pp. 217–225, 2017. [Online]. Available: https://www.sciencedirect.com/science/article/pii/S0925400516320123

[35] C. Poole, H. Presby, and J. Meester, "Two-mode fibre spatial-mode converter using periodic core deformation," *Electronics Letters*, vol. 30, pp. 1437–1438(1), August 1994. [Online]. Available: https://digital-library.theiet.org/content/journals/10.1049/el_19940948

[36] S. Thomas Lee, R. Dinesh Kumar, P. Suresh Kumar, P. Radhakrishnan, C. Vallabhan, and V. Nampoori, "Long period gratings in multimode optical fibers: application in chemical sensing," *Optics Communications*, vol. 224, no. 4, pp. 237–241, 2003. [Online]. Available: https://www.sciencedirect.com/science/article/pii/S0030401803015979

[37] G. Humbert, A. Malki, S. Février, P. Roy, J.-L. Auguste, and J.-M. Blondy, "Long period grating filters fabricated with electric arc in dual concentric core fibers," *Optics Communications*, vol. 225, no. 1, pp. 47–53, 2003. [Online]. Available: https://www.sciencedirect.com/science/article/pii/S0030401803017863

[38] T. Allsop, D. Webb, and I. Bennion, “Investigations of the spectral sensitivity of long period gratings fabricated in three-layered optical fiber,” *Journal of Lightwave Technology*, vol. 21, no. 1, pp. 264–268, 2003.

[39] K. J. Han, Y. W. Lee, J. Kwon, S. Roh, J. Jung, and B. Lee, “Simultaneous measurement of strain and temperature incorporating a long-period fiber grating inscribed on a polarization-maintaining fiber,” *IEEE Photonics Technology Letters*, vol. 16, no. 9, pp. 2114–2116, 2004.

[40] T. J. Eom, S.-J. Kim, T.-Y. Kim, C.-S. Park, and B. H. Lee, “Optical pulse multiplication and temporal coding using true time delay achieved by long-period fiber gratings in dispersion compensating fiber,” *Opt. Express*, vol. 12, no. 26, pp. 6410–6420, Dec 2004. [Online]. Available: https://opg.optica.org/oe/abstract.cfm?URI=oe-12-26-6410

[41] L. Dong, L. Reekie, and J. L. Cruz, “Long period gratings formed in depressed cladding fibres,” in *Bragg Gratings, Photosensitivity, and Poling in Glass Fibers and Waveguides: Applications and Fundamentals*. Optica Publishing Group, 1997, p. BMG.17. [Online]. Available: https://opg.optica.org/abstract.cfm?URI=BGPPF-1997-BMG.17

[42] L. Rindorf, J. B. Jensen, M. Dufva, L. H. Pedersen, P. E. Høiby, and O. Bang, “Photonic crystal fiber long-period gratings for biochemical sensing,” *Opt. Express*, vol. 14, no. 18, pp. 8224–8231, Sep 2006. [Online]. Available: https://opg.optica.org/oe/abstract.cfm?URI=oe-14-18-8224

[43] P. Xue, F. Yu, Y. Cao, and J. Zheng, “Refractive index sensing based on a long period grating imprinted on a multimode plastic optical fiber,” *IEEE Sensors Journal*, vol. 19, no. 17, pp. 7434–7439, 2019.

[44] Y. Xu, P. Lu, L. Chen, and X. Bao, “Recent developments in microstructured fiber optic sensors,” *Fibers*, vol. 5, no. 1, 2017. [Online]. Available: https://www.mdpi.com/2079-6439/5/1/3

[45] Y. Tan, W. Ji, V. Mamidala, K. Chow, and S. Tjin, “Carbon-nanotube-deposited long period fiber grating for continuous refractive index sensor applications,” *Sensors and Actuators B: Chemical*, vol. 196, pp. 260–264, 2014. [Online]. Available: https://www.sciencedirect.com/science/article/pii/S092540051400080X

[46] B. R. Heidemann, I. Chiamenti, M. M. Oliveira, M. Muller, and J. L. Fabris, "Plasmonic optical fiber sensors: enhanced sensitivity in water-based environments," *Appl. Opt.*, vol. 54, no. 27, pp. 8192–8197, Sep 2015. [Online]. Available: https://opg.optica.org/ao/abstract.cfm?URI=ao-54-27-8192

[47] Z. Li, T. Chen, Z. Zhang, Y. Zhou, D. Li, and Z. Xie, "Highly sensitive surface plasmon resonance sensor utilizing a long period grating with photosensitive cladding," *Appl. Opt.*, vol. 55, no. 6, pp. 1470–1480, Feb 2016. [Online]. Available: https://opg.optica.org/ao/abstract.cfm?URI=ao-55-6-1470

[48] S. A. Maier, *Surface Plasmon Polaritons at Metal / Insulator Interfaces*. New York, NY: Springer US, 2007, pp. 21–37. [Online]. Available: https://doi.org/10.1007/0-387-37825-1_2

[49] R. W. Wood, "On a remarkable case of uneven distribution of light in a diffraction grating spectrum," *Proceedings of the Physical Society of London*, vol. 18, no. 1, p. 269, jun 1902. [Online]. Available: https://dx.doi.org/10.1088/1478-7814/18/1/325

[50] L. R. O. P.R.S., "Iii. note on the remarkable case of diffraction spectra described by prof. wood," *The London, Edinburgh, and Dublin Philosophical Magazine and Journal of Science*, vol. 14, no. 79, pp. 60–65, 1907. [Online]. Available: https://doi.org/10.1080/14786440709463661

[51] A. Hessel and A. A. Oliner, "A new theory of wood's anomalies on optical gratings," *Appl. Opt.*, vol. 4, no. 10, pp. 1275–1297, Oct 1965. [Online]. Available: https://opg.optica.org/ao/abstract.cfm?URI=ao-4-10-1275

[52] R. W. Wood, "Anomalous diffraction gratings," *Phys. Rev.*, vol. 48, pp. 928–936, Dec 1935. [Online]. Available: https://link.aps.org/doi/10.1103/PhysRev.48.928

[53] D. Pines and D. Bohm, "A collective description of electron interactions: Ii. collective vs individual particle aspects of the interactions," *Phys. Rev.*, vol. 85, pp. 338–353, Jan 1952. [Online]. Available: https://link.aps.org/doi/10.1103/PhysRev.85.338

[54] R. H. Ritchie, "Plasma losses by fast electrons in thin films," *Phys. Rev.*, vol. 106, pp. 874–881, Jun 1957. [Online]. Available: https://link.aps.org/doi/10.1103/PhysRev.106.874

[55] C. J. Powell and J. B. Swan, “Origin of the characteristic electron energy losses in magnesium,” *Phys. Rev.*, vol. 116, pp. 81–83, Oct 1959. [Online]. Available: https://link.aps.org/doi/10.1103/PhysRev.116.81

[56] E. Kretschmann and H. Raether, “Notizen: Radiative decay of non radiative surface plasmons excited by light,” *Zeitschrift für Naturforschung A*, vol. 23, no. 12, pp. 2135–2136, 1968. [Online]. Available: https://doi.org/10.1515/zna-1968-1247

[57] A. Otto, “Excitation of nonradiative surface plasma waves in silver by method of frustrated total reflection,” *European Physical Journal A*, vol. 216, pp. 398–410, 08 1968.

[58] C. Nylander, B. Liedberg, and T. Lind, “Gas detection by means of surface plasmon resonance,” *Sensors and Actuators*, vol. 3, pp. 79–88, 1982. [Online]. Available: https://www.sciencedirect.com/science/article/pii/0250687482800085

[59] H. H. Nguyen, J. Park, S. Kang, and M. Kim, “Surface plasmon resonance: A versatile technique for biosensor applications,” *Sensors*, vol. 15, no. 5, pp. 10 481–10 510, 2015. [Online]. Available: https://www.mdpi.com/1424-8220/15/5/10481

[60] A. Paliwal, A. Sharma, M. Tomar, and V. Gupta, “Carbon monoxide (co) optical gas sensor based on zno thin films,” *Sensors and Actuators B: Chemical*, vol. 250, pp. 679–685, 2017. [Online]. Available: https://www.sciencedirect.com/science/article/pii/S0925400517308857

[61] S. K. Mishra, S. N. Tripathi, V. Choudhary, and B. D. Gupta, “Spr based fibre optic ammonia gas sensor utilizing nanocomposite film of pmma/reduced graphene oxide prepared by in situ polymerization,” *Sensors and Actuators B: Chemical*, vol. 199, pp. 190–200, 2014. [Online]. Available: https://www.sciencedirect.com/science/article/pii/S0925400514003852

[62] P. Tobiška, O. Hugon, A. Trouillet, and H. Gagnaire, “An integrated optic hydrogen sensor based on spr on palladium,” *Sensors and Actuators B: Chemical*, vol. 74, no. 1, pp. 168–172, 2001, proceedings of the 5th European Conference on Optical Chemical Sensors and Biosensors. [Online]. Available: https://www.sciencedirect.com/science/article/pii/S0925400500007280

[63] Y. Saylan, S. Akgönüllü, D. Çimen, A. Derazshamshir, N. Bereli, F. Yılmaz, and A. Denizli, "Development of surface plasmon resonance sensors based on molecularly imprinted nanofilms for sensitive and selective detection of pesticides," *Sensors and Actuators B: Chemical*, vol. 241, pp. 446–454, 2017. [Online]. Available: https://www.sciencedirect.com/science/article/pii/S0925400516316434

[64] C. Boulart, R. Prien, V. Chavagnac, and J.-P. Dutasta, "Sensing dissolved methane in aquatic environments: An experiment in the central baltic sea using surface plasmon resonance," *Environmental Science & Technology*, vol. 47, no. 15, pp. 8582–8590, 2013, pMID: 23815404. [Online]. Available: https://doi.org/10.1021/es4011916

[65] S. B. Borah, T. Bora, S. Baruah, and J. Dutta, "Heavy metal ion sensing in water using surface plasmon resonance of metallic nanostructures," *Groundwater for Sustainable Development*, vol. 1, no. 1, pp. 1–11, 2015. [Online]. Available: https://www.sciencedirect.com/science/article/pii/S2352801X15300072

[66] T. M. Chinowsky, S. D. Soelberg, P. Baker, N. R. Swanson, P. Kauffman, A. Mactutis, M. S. Grow, R. Atmar, S. S. Yee, and C. E. Furlong, "Portable 24-analyte surface plasmon resonance instruments for rapid, versatile biodetection," *Biosensors and Bioelectronics*, vol. 22, no. 9, pp. 2268–2275, 2007, selected Papers from the Ninth World Congress On Biosensors. Toronto, Canada 10 - 12 May 2006. [Online]. Available: https://www.sciencedirect.com/science/article/pii/S0956566306005562

[67] B. Wang, P. Yu, W. Wang, X. Zhang, H.-C. Kuo, H. Xu, and Z. M. Wang, "High-q plasmonic resonances: Fundamentals and applications," *Advanced Optical Materials*, vol. 9, no. 7, p. 2001520, 2021. [Online]. Available: https://onlinelibrary.wiley.com/doi/abs/10.1002/adom.202001520

[68] M. G. Blaber, M. D. Arnold, and M. J. Ford, "A review of the optical properties of alloys and intermetallics for plasmonics," *Journal of Physics: Condensed Matter*, vol. 22, no. 14, p. 143201, mar 2010. [Online]. Available: https://dx.doi.org/10.1088/0953-8984/22/14/143201

[69] C. Rhodes, S. Franzen, J. Maria, M. Losego, D. Leonard, B. Laughlin, G. Duscher, and S. Weibel, "Surface plasmon resonance in conducting metal oxides," *Journal of Applied Physics*, vol. 100, no. 5, 2006.

[70] W. Yang, J. Gao, Z. Li, C. Li, Y. Cheng, Y. Huo, S. Jiang, and M. Jiang, "High performance d-type plastic fiber spr sensor based on a hyperbolic metamaterial composed of ag/mgf2," *J. Mater. Chem. C*, vol. 9, pp. 13 647–13 658, 2021. [Online]. Available: http://dx.doi.org/10.1039/D1TC02217B

[71] M. S. Hamed, M. A. Adedeji, and G. T. Mola, "Rare-earth metal-induced plasmon resonances for enhanced photons harvesting in inverted thin film organic solar cell," *Energy & Fuels*, vol. 35, no. 18, pp. 15 010–15 017, 2021. [Online]. Available: https://doi.org/10.1021/acs.energyfuels.1c01907

[72] E. Petryayeva and U. J. Krull, "Localized surface plasmon resonance: Nanostructures, bioassays and biosensing—a review," *Analytica Chimica Acta*, vol. 706, no. 1, pp. 8–24, 2011. [Online]. Available: https://www.sciencedirect.com/science/article/pii/S0003267011011196

[73] D. T. Nurrohman and N.-F. Chiu, "A review of graphene-based surface plasmon resonance and surface-enhanced raman scattering biosensors: Current status and future prospects," *Nanomaterials*, vol. 11, no. 1, 2021. [Online]. Available: https://www.mdpi.com/2079-4991/11/1/216

[74] G.-S. Liu, X. Xiong, S. Hu, W. Shi, Y. Chen, W. Zhu, H. Zheng, J. Yu, N. H. Azeman, Y. Luo, and Z. Chen, "Photonic cavity enhanced high-performance surface plasmon resonance biosensor," *Photon. Res.*, vol. 8, no. 4, pp. 448–456, Apr 2020. [Online]. Available: https://opg.optica.org/prj/abstract.cfm?URI=prj-8-4-448

[75] A. Steinegger, O. S. Wolfbeis, and S. M. Borisov, "Optical sensing and imaging of ph values: Spectroscopies, materials, and applications," *Chemical Reviews*, vol. 120, no. 22, pp. 12 357–12 489, 2020, pMID: 33147405. [Online]. Available: https://doi.org/10.1021/acs.chemrev.0c00451

[76] D. Wencel, T. Abel, and C. McDonagh, "Optical chemical ph sensors," *Analytical Chemistry*, vol. 86, no. 1, pp. 15–29, 2014, pMID: 24180284. [Online]. Available: https://doi.org/10.1021/ac4035168

[77] J. I. Peterson, S. R. Goldstein, R. V. Fitzgerald, and D. K. Buckhold, "Fiber optic ph probe for physiological use," *Analytical Chemistry*, vol. 52, no. 6, pp. 864–869, 1980, pMID: 7396208. [Online]. Available: https://doi.org/10.1021/ac50056a022

[78] Y. Zhao, M. Lei, S.-X. Liu, and Q. Zhao, “Smart hydrogel-based optical fiber spr sensor for ph measurements,” *Sensors and Actuators B: Chemical*, vol. 261, pp. 226–232, 2018. [Online]. Available: https://www.sciencedirect.com/science/article/pii/S0925400518301266

[79] J. M. Corres, I. del Villar, I. R. Matias, and F. J. Arregui, “Fiber-optic ph-sensors in long-period fiber gratings using electrostatic self-assembly,” *Opt. Lett.*, vol. 32, no. 1, pp. 29–31, Jan 2007. [Online]. Available: https://opg.optica.org/ol/abstract.cfm?URI=ol-32-1-29

[80] V. N. K. Pabbisetti and S. S. Madhuvarasu, “Hydrogel-coated fiber Bragg grating sensor for pH monitoring,” *Optical Engineering*, vol. 55, no. 6, p. 066112, 2016. [Online]. Available: https://doi.org/10.1117/1.OE.55.6.066112

[81] B. Gu, M. Yin, A. P. Zhang, J. Qian, and S. He, “Biocompatible fiber-optic ph sensor based on optical fiber modal interferometer self-assembled with sodium alginate/polyethylenimine coating,” *IEEE Sensors Journal*, vol. 12, no. 5, pp. 1477–1482, 2012.

[82] A. Lopez Aldaba, □. González-Vila, M. Debliquy, M. Lopez-Amo, C. Caucheteur, and D. Lahem, “Polyaniline-coated tilted fiber bragg gratings for ph sensing,” *Sensors and Actuators B: Chemical*, vol. 254, pp. 1087–1093, 2018. [Online]. Available: https://www.sciencedirect.com/science/article/pii/S0925400517313813

[83] V. Kozlovskaya, E. Kharlampieva, B. P. Khanal, P. Manna, E. R. Zubarev, and V. V. Tsukruk, “Ultrathin layer-by-layer hydrogels with incorporated gold nanorods as ph-sensitive optical materials,” *Chemistry of Materials*, vol. 20, no. 24, pp. 7474–7485, 2008. [Online]. Available: https://doi.org/10.1021/cm8023633

[84] M. Tsui and L. Chu, “Environmental fate and non-target impact of glyphosate-based herbicide (roundup®) in a subtropical wetland,” *Chemosphere*, vol. 71, no. 3, pp. 439–446, 2008. [Online]. Available: https://www.sciencedirect.com/science/article/pii/S0045653507013616

[85] A. Valle, F. Mello, R. Balvedi, L. Rodrigues, and L. Goulart, “Glyphosate detection: methods, needs and challenges,” *Environmental Chemistry Letters*, vol. 17, 09 2018.

[86] N. Khansili, G. Rattu, and P. M. Krishna, “Label-free optical biosensors for food and biological sensor applications,” *Sensors and Actuators B: Chemical*, vol. 265, pp. 35–49, 2018. [Online]. Available: https://www.sciencedirect.com/science/article/pii/S0925400518304829

[87] X. Ding and K.-L. Yang, “Development of an oligopeptide functionalized surface plasmon resonance biosensor for online detection of glyphosate,” *Analytical Chemistry*, vol. 85, no. 12, pp. 5727–5733, 2013, pMID: 23675691. [Online]. Available: https://doi.org/10.1021/ac400273g

[88] M. Vráblová, K. Smutná, I. Koutník, T. Prostějovský, and R. Žebrák, “Surface plasmon resonance imaging sensor for detection of photolytically and photocatalytically degraded glyphosate,” *Sensors*, vol. 22, no. 23, 2022. [Online]. Available: https://www.mdpi.com/1424-8220/22/23/9217

[89] A. Valle, K. Ferreira, L. Goulart, C. Freire, E. Medeiros, C. Filho, R. Cruz, L. Rodrigues, and C. Moreira, “Smartphone-based surface plasmon resonance sensor for glyphosate detection: Different ph and concentrations,” *Plasmonics*, vol. 18, pp. 1–10, 03 2023.

[90] T. Erdogan, “Fiber grating spectra,” *Journal of Lightwave Technology*, vol. 15, no. 8, pp. 1277–1294, 1997.

[91] Z. Jacob and V. M. Shalaev, “Plasmonics goes quantum,” *Science*, vol. 334, no. 6055, pp. 463–464, 2011. [Online]. Available: https://www.science.org/doi/abs/10.1126/science.1211736

[92] J. Homola, *Electromagnetic Theory of Surface Plasmons*, 07 2006, vol. 4, pp. 3–44.

[93] A. Movsesyan, “Plasmonic Properties of Metallic Nanoparticles : Beyond the Dipolar Resonance,” Theses, Université de Technologie de Troyes, Dec. 2018. [Online]. Available: https://theses.hal.science/tel-03610410

[94] M. Bertolotti, C. Sibilia, and □. Guzmán, *Evanescent Waves in Optics: An Introduction to Plasmonics*, 01 2017.

[95] W. Lukosz, “Principles and sensitivities of integrated optical and surface plasmon sensors for direct affinity sensing and immunosensing,” *Biosensors*

and Bioelectronics, vol. 6, no. 3, pp. 215–225, 1991. [Online]. Available: https://www.sciencedirect.com/science/article/pii/095656639180006J

[96] A. V. Zayats, I. I. Smolyaninov, and A. A. Maradudin, "Nano-optics of surface plasmon polaritons," *Physics Reports*, vol. 408, no. 3, pp. 131–314, 2005. [Online]. Available: https://www.sciencedirect.com/science/article/pii/S0370157304004600

[97] H. Raether, *Surface plasmons on gratings*. Berlin, Heidelberg: Springer Berlin Heidelberg, 1988, pp. 91–116. [Online]. Available: https://doi.org/10.1007/BFb0048323

[98] R. Jorgenson and S. Yee, "A fiber-optic chemical sensor based on surface plasmon resonance," *Sensors and Actuators B: Chemical*, vol. 12, no. 3, pp. 213–220, 1993. [Online]. Available: https://www.sciencedirect.com/science/article/pii/0925400593800213

[99] R. Ulrich and R. Torge, "Measurement of thin film parameters with a prism coupler," *Appl. Opt.*, vol. 12, no. 12, pp. 2901–2908, Dec 1973. [Online]. Available: https://opg.optica.org/ao/abstract.cfm?URI=ao-12-12-2901

[100] J. Fahrenfort, "Attenuated total reflection: A new principle for the production of useful infra-red reflection spectra of organic compounds," *Spectrochimica Acta*, vol. 17, no. 7, pp. 698–709, 1961. [Online]. Available: https://www.sciencedirect.com/science/article/pii/0371195161801367

[101] C. Teng, S. Ying, R. Min, S. Deng, H. Deng, M. Chen, X. Chu, L. Yuan, Y. Cheng, and M. Xue, "Side-polish plastic optical fiber based spr sensor for refractive index and liquid-level sensing," *Sensors*, vol. 22, no. 16, 2022. [Online]. Available: https://www.mdpi.com/1424-8220/22/16/6241

[102] D. Gloge, "Weakly guiding fibers," *Appl. Opt.*, vol. 10, no. 10, pp. 2252–2258, Oct 1971. [Online]. Available: https://opg.optica.org/ao/abstract.cfm?URI=ao-10-10-2252

[103] P. Markos and C. M. Soukoulis, *Wave Propagation: From Electrons to Photonic Crystals and Left-Handed Materials*, 2008.

[104] D. Griffiths, *Introduction to Electrodynamics*. Pearson Education, 2014. [Online]. Available: https://books.google.pt/books?id=J9ygBwAAQBAJ

[105] E. Cohen, R. S. of Chemistry (Great Britain), I. U. of Pure, A. C. Physical, and B. C. Division, *Quantities, Units and Symbols in Physical Chemistry*. Royal Society of Chemistry, 2007. [Online]. Available: https://books.google.pt/books?id=TEImhULQoeIC

[106] B. Dias, "Electromagnetic surface waves in one dimensional structures: Application to optical sensors," Master's thesis, FCUP, 2022. [Online]. Available: https://hdl.handle.net/10216/147296

[107] J. Ctyroky, J. Homola, and M. Skalsky, "Modelling of surface plasmon resonance waveguide sensor by complex mode expansion and propagation method," *Optical and Quantum Electronics*, vol. 29, pp. 301–311, 1997. [Online]. Available: https://api.semanticscholar.org/CorpusID:117078964

[108] M. Blaber, M. Arnold, N. Harris, M. Ford, and M. Cortie, "Plasmon absorption in nanospheres: A comparison of sodium, potassium, aluminium, silver and gold," *Physica B: Condensed Matter*, vol. 394, no. 2, pp. 184–187, 2007. [Online]. Available: https://www.sciencedirect.com/science/article/pii/S0921452606018977

[109] Z. Wang, Z. Cheng, V. Singh, Z. Zheng, Y. Wang, S. Li, L. Song, and J. Zhu, "Stable and sensitive silver surface plasmon resonance imaging sensor using trilayered metallic structures," *Analytical Chemistry*, vol. 86, no. 3, pp. 1430–1436, 2014, pMID: 24372308. [Online]. Available: https://doi.org/10.1021/ac402126k

[110] J. Andersson, J. Svirelis, G. Ferrand-Drake del Castillo, T. Sannomiya, and A. Dahlin, "Surface plasmon resonance sensing with thin films of palladium and platinum – quantitative and real-time analysis," *Phys. Chem. Chem. Phys.*, vol. 24, pp. 4588–4594, 2022. [Online]. Available: http://dx.doi.org/10.1039/D1CP05381G

[111] J. C. Quail, J. G. Rako, and H. J. Simon, "Long-range surface-plasmon modes in silver and aluminum films," *Opt. Lett.*, vol. 8, no. 7, pp. 377–379, Jul 1983. [Online]. Available: https://opg.optica.org/ol/abstract.cfm?URI=ol-8-7-377

[112] R. Todorov, V. Lozanova, P. Knotek, E. Černošková, and M. Vlček, "Microstructure and ellipsometric modelling of the optical properties of very thin silver films for application in plasmonics," *Thin Solid Films*, vol. 628, pp. 22–30, 2017. [Online]. Available: https://www.sciencedirect.com/science/article/pii/S0040609017301840

[113] D. I. Yakubovsky, A. V. Arsenin, Y. V. Stebunov, D. Y. Fedyanin, and V. S. Volkov, "Optical constants and structural properties of thin gold films," *Opt. Express*, vol. 25, no. 21, pp. 25 574–25 587, Oct 2017. [Online]. Available: https://opg.optica.org/oe/abstract.cfm?URI=oe-25-21-25574

[114] Y. Singh and S. K. Raghuwanshi, "Titanium dioxide (tio2) coated optical fiber-based spr sensor in near-infrared region with bimetallic structure for enhanced sensitivity," *Optik*, vol. 226, p. 165842, 2021. [Online]. Available: https://www.sciencedirect.com/science/article/pii/S0030402620316624

[115] R. K. Verma and B. D. Gupta, "Surface plasmon resonance based fiber optic sensor for the ir region using a conducting metal oxide film," *J. Opt. Soc. Am. A*, vol. 27, no. 4, pp. 846–851, Apr 2010. [Online]. Available: https://opg.optica.org/josaa/abstract.cfm?URI=josaa-27-4-846

[116] R. Tabassum and B. D. Gupta, "Performance analysis of bimetallic layer with zinc oxide for spr-based fiber optic sensor," *J. Lightwave Technol.*, vol. 33, no. 22, pp. 4565–4571, Nov 2015. [Online]. Available: https://opg.optica.org/jlt/abstract.cfm?URI=jlt-33-22-4565

[117] W. Yuan, Z. Lu, and C. M. Li, "Charged drug delivery by ultrafast exponentially grown weak polyelectrolyte multilayers: amphoteric properties, ultrahigh loading capacity and ph-responsiveness," *J. Mater. Chem.*, vol. 22, pp. 9351–9357, 2012. [Online]. Available: http://dx.doi.org/10.1039/C2JM30834G

[118] Y.-H. Yang, M. Haile, Y. T. Park, F. A. Malek, and J. C. Grunlan, "Super gas barrier of all-polymer multilayer thin films," *Macromolecules*, vol. 44, no. 6, pp. 1450–1459, 2011. [Online]. Available: https://doi.org/10.1021/ma1026127

[119] B. Dias, J. P. S. Mendes, J. M. Marques Martins de Almeida, and L. C. C. Coelho, "Simple optical fiber interferometer for dynamic measurement of refractive index and thickness of polymer films," *IEEE Sensors Journal*, vol. 22, no. 12, pp. 11 732–11 739, 2022.

[120] R. Y. N. Wong, E. Chehura, S. E. Staines, S. W. James, and R. P. Tatam, "Fabrication of fiber optic long period gratings operating at the phase matching turning point using an ultraviolet laser," *Appl. Opt.*, vol. 53, no. 21, pp. 4669–4674, Jul 2014. [Online]. Available: https://opg.optica.org/ao/abstract.cfm?URI=ao-53-21-4669

[121] D. Davis, T. Gaylord, E. Glytsis, S. Kosinski, S. Mettler, and A. Vengsarkar, "Long-period fibre grating fabrication with focused co2 laser pulses," *Electronics Letters*, vol. 34, pp. 302–303(1), February 1998. [Online]. Available: https://digital-library.theiet.org/content/journals/10.1049/el_19980239

[122] F. Ahmed, H.-E. Joe, B.-K. Min, and M. B. Jun, "Characterization of refractive index change and fabrication of long period gratings in pure silica fiber by femtosecond laser radiation," *Optics & Laser Technology*, vol. 74, pp. 119–124, 2015. [Online]. Available: https://www.sciencedirect.com/science/article/pii/S0030399215001486

[123] M. L. von Bibra, A. Roberts, and J. Canning, "Fabrication of long-period fiber gratings by use of focused ion-beam irradiation," *Opt. Lett.*, vol. 26, no. 11, pp. 765–767, Jun 2001. [Online]. Available: https://opg.optica.org/ol/abstract.cfm?URI=ol-26-11-765

[124] M. Fujimaki, Y. Ohki, J. L. Brebner, and S. Roorda, "Fabrication of long-period optical fiber gratings by use of ion implantation," *Opt. Lett.*, vol. 25, no. 2, pp. 88–89, Jan 2000. [Online]. Available: https://opg.optica.org/ol/abstract.cfm?URI=ol-25-2-88

[125] S. R. H. Largani, H.-Y. Wen, J.-L. Chen, and C.-C. Chiang, "Photoresist-free, laser-assisted chemical etching process for long-period fiber grating," *Opt. Express*, vol. 27, no. 20, pp. 28 606–28 617, Sep 2019. [Online]. Available: https://opg.optica.org/oe/abstract.cfm?URI=oe-27-20-28606

[126] S. Savin, M. J. F. Digonnet, G. S. Kino, and H. J. Shaw, "Tunable mechanically induced long-period fiber gratings," *Opt. Lett.*, vol. 25, no. 10, pp. 710–712, May 2000. [Online]. Available: https://opg.optica.org/ol/abstract.cfm?URI=ol-25-10-710

[127] S.-Y. Tan, Y.-T. Yong, S.-C. Lee, and F. A. Rahman, "Review on an arc-induced long-period fiber grating and its sensor applications," *Journal of Electromagnetic Waves and Applications*, vol. 29, no. 6, pp. 703–726, 2015. [Online]. Available: https://doi.org/10.1080/09205071.2015.1021019

[128] G. Rego, P. Caldas, and O. V. Ivanov, "Arc-induced long-period fiber gratings at inesc tec. part i: Fabrication, characterization and mechanisms of formation," *Sensors*, vol. 21, no. 14, 2021. [Online]. Available: https://www.mdpi.com/1424-8220/21/14/4914

[129] G. Rego, "Fibre optic devices produced by arc discharges," *Journal of Optics*, vol. 12, no. 11, p. 113002, nov 2010. [Online]. Available: https://dx.doi.org/10.1088/2040-8978/12/11/113002

[130] E. Dianov, V. Karpov, M. Grekov, K. Golant, S. Vasiliev, O. Medvedkov, and R. Khrapko, "Thermo-induced long-period fibre gratings," in *Integrated Optics and Optical Fibre Communications, 11th International Conference on, and 23rd European Conference on Optical Communications (Conf. Publ. No.: 448)*, vol. 2, 1997, pp. 53–56 vol.2.

[131] G. REGO, P. V. S. MARQUES, J. L. SANTOS, and H. M. SALGADO, "Arc-induced long-period gratings," *Fiber and Integrated Optics*, vol. 24, no. 3-4, pp. 245–259, 2005. [Online]. Available: https://doi.org/10.1080/01468030590922975

[132] V. Kumar, S. K. Raghuwanshi, and S. Kumar, "Advances in nanocomposite thin-film-based optical fiber sensors for environmental health monitoring—a review," *IEEE Sensors Journal*, vol. 22, no. 15, pp. 14 696–14 707, 2022.

[133] D. Smith, *Thin-Film Deposition: Principles and Practice*. McGraw-Hill Education, 1995. [Online]. Available: https://books.google.pt/books?id=kTVkwRWwxfYC

[134] J. J. Richardson, M. Björnmalm, and F. Caruso, "Technology-driven layer-by-layer assembly of nanofilms," *Science*, vol. 348, no. 6233, p. aaa2491, 2015. [Online]. Available: https://www.science.org/doi/abs/10.1126/science.aaa2491

[135] X. Zhang, H. Chen, and H. Zhang, "Layer-by-layer assembly: from conventional to unconventional methods," *Chem. Commun.*, pp. 1395–1405, 2007. [Online]. Available: http://dx.doi.org/10.1039/B615590A

[136] S. S. Shiratori and M. F. Rubner, "ph-dependent thickness behavior of sequentially adsorbed layers of weak polyelectrolytes," *Macromolecules*, vol. 33, no. 11, pp. 4213–4219, 2000. [Online]. Available: https://doi.org/10.1021/ma991645q

[137] D. D. Perrin and B. Dempsey, *The Theory of Buffer Action*. Dordrecht: Springer Netherlands, 1974, pp. 4–23. [Online]. Available: https://doi.org/10.1007/978-94-009-5874-6_2

[138] M. Guenther, G. Gerlach, and T. Wallmersperger, "Non-linear effects in hydrogel-based chemical sensors: Experiment and modeling," *Journal of Intelligent Material*

Systems and Structures, vol. 20, no. 8, pp. 949–961, 2009. [Online]. Available: https://doi.org/10.1177/1045389X08101562

[139] M. Annaka and T. Tanaka, "Multiple phases of polymer gels," *Nature*, vol. 355, pp. 430–432, 01 1992.

[140] F. Reyes-Ortega, "3 - ph-responsive polymers: properties, synthesis and applications," in *Smart Polymers and their Applications*, M. R. Aguilar and J. San Román, Eds. Woodhead Publishing, 2014, pp. 45–92. [Online]. Available: https://www.sciencedirect.com/science/article/pii/B9780857096951500030

[141] B. D. Ventura, M. Cennamo, A. Minopoli, R. Campanile, S. B. Censi, D. Terracciano, G. Portella, and R. Velotta, "Colorimetric test for fast detection of sars-cov-2 in nasal and throat swabs," *ACS Sensors*, vol. 5, no. 10, pp. 3043–3048, 2020, pMID: 32989986. [Online]. Available: https://doi.org/10.1021/acssensors.0c01742